THE $D(d,n)^3He$ REACTION AND N-P SCATTERING

Allan Bruce Jones

A thesis submitted as a requirement

for the degree of

Master of Science

at the

Australian National University

December 1980

PREFACE

The work described in this thesis was carried out on the cyclotron injector and the EN tandem accelerator system in the Department of Nuclear Physics at the Australian National University.

The thesis is divided into two distinct parts. Part I considers the $D(d,n)^3He$ reaction which includes measurements of the differential cross sections and the use of this reaction as a neutron source. Part II examines the measurement of n-p differential cross sections. This includes the development and use of Monte Carlo techniques for data analysis. Each part has its own introduction.

The project was suggested by Dr. C.M. Bartle, who at the time was my supervisor, but on leaving after 12 months for an overseas posting, Dr. T.R. Ophel became my official supervisor. In the early stages of the experimental work the round-the-clock running of experiments was shared by Dr. C.M. Bartle, Dr. D.W. Gebbie and myself. I am grateful to both for their assistance in those early days.

The experimental equipment used was to a large degree already in existence, the $D(d,n)^3He$ associated particle scattering chamber and ^3He detection system having been constructed by Dr. C.M. Bartle. The design of the additional equipment and some modifications to the existing equipment were undertaken by myself.

For the data collection and basic sorting existing computer programs were used. All other data analysis programs were written by myself. Dr. H.J. Hay was of much

assistance in keeping the IBM 1800 computer operating in times of need.

The Monte Carlo program was mostly written by myself. I am indebted to Mr. E. Clayton for initial discussions about the program and for supplying the microscopic total cross section data complete with a subroutine for the calculation of the absorption coefficients for NE102.

Much of the work in Chapter 2 of this thesis has appeared in the following publication:

"D(d,n)^{3}He Differential Cross Sections from 18 to 26 MeV", A.B. Jones, Aust. J. Phys., 33 (1980) 203.

I extend my thanks also to the following:

Dr. C.S. Newton, Dr. S.H. Sie and Dr. P.B. Treacy for their willingness to assist;

Professor J.O. Newton, for giving me the opportunity to use the facilities of this laboratory;

Mr. G.P. Clarkson, for the careful photographic reproduction of a large number of the diagrams;

Dr. T.R. Ophel for reading the drafts of this thesis and the afore mentioned publication.

I especially thank my wife for her support while this work was brought to completion.

The work reported in this thesis is my own, except where it has been otherwise acknowledged. No part of this work has been submitted for another degree.

B. Jones

ABSTRACT

Angular distributions of the $D(d,n)^3He$ reaction have been measured for incident deuteron energies of 18, 20, 22, 24 and 26 MeV. The data provided no evidence for the proposed broad level in ^4He at approximately 30 MeV.

The $D(d,n)^3He$ reaction was used as a neutron source by means of the associated particle technique. This neutron source was the basis of a study of the measurement of n-p differential cross sections using plastic scintillators os the proton targets. The study included two distinct approaches, discrete measurements and unfolding from continuous spectra, both of which required the application of Monte Carlo techniques in the analysis and error correction calculations. Despite the lack of success in obtaining good differential cross section data, the work has demonstrated the usefullness of applying Monte Carlo techniques in the analysis of experimental data.

Table of contents

PART I

PART II

Table of contents

Table of contents

1. INTRODUCTION

1.1. Neutron Sources

Since the discovery of the neutron by J. Chadwick (Ch32) researchers have relied on nuclear reactions as their source of neutrons. Some reactions which have been extensively used for this purpose are: $^{9}Be(\alpha,n)\ ^{12}C$ (Q=5.708 MeV); $^{7}Li(p,n)^{7}Be$ (Q=-1.646 MeV); $^{9}Be(d,n)^{10}B$ (Q=4.35 MeV); $^{3}H(p,n)^{3}He$ (Q=-0.7); and $^{3}H(d,n)^{4}He$ (Q=17.6MeV). The $^{9}Be(\alpha,n)^{12}C$ reaction can be used with a natural alpha emitter, for example, radium, to provide portable neutron sources. It was, in fact, this reaction which Chadwick used in his early work with neutrons. Be can also be used with a gamma emitter with energies greater than the binding energy of the last neutron, 1.67 MeV, to provide a source of neutron.

For a more intense neutron source, fission reactors are used. The beam from these reactors can be chopped using the neutron's time of flight to select neutrons of the required energy. A third method uses charged particle accelerators to induce an appropriate reaction to produce neutrons. This approach readily enables the use of the associated particle technique in which detection of the associated recoil ion at a particular angle kinematically determines the energy and the direction of the emitted neutron. Thus by determining the number of recoil ions, the associated particle technique is capable of producing an essentially monoenergetic neutron

beam of known flux. The measurement of the neutron flux is absolute and free from any previously determined standards.

In the past, the preferred reaction for use with the associated particle technique for the production of neutrons above 14 MeV was the $^{3}H(d,^{4}He)n$ reaction which has a Q value of 17.59 MeV. The high Q value means that only relatively low energy deuterons are required. This reaction has the disadvantage of a somewhat hazardous and difficult target technology which involves the handling of gaseous tritium or tritiated foils. In contrast, the $D(d,n)^{3}He$ reaction has a Q value of only 3.27MeV, which means that much higher deuteron energies are required. However, to offset this the target technology is simpler as deuterated polyethylene foils can be used. These foils are stable, non-hazardous and can readily be made into foils of a chosen thickness (Ba77). The $D(d,n)^{3}He$ reaction is also a desirable reaction because the recoil ion only has one bound state, the ground state, meaning that the ratio of neutrons produced (at the required energy) to recoil ions detected, is a maximum, thus giving a faster count rate.

1.2. Using the $D(d,n)^{3}He$ Reaction

Early attempts to use the $D(d,n)^{3}He$ reaction as an associated particle neutron source suffered from the difficulty of unambiguously resolving the associated ^{3}He events from the background of products produced by other reactions such as deuteron elastic scattering, $^{12}C(d,\alpha)^{10}B$ and $^{2}H(d,p)^{3}H$. The problem is clearly shown in Figure (1.1)

which is a typical energy spectrum obtained using a silicon surface barrier detector. The ^{3}He peak clearly contains significant background contributions making it difficult to isolate the ^{3}He events.

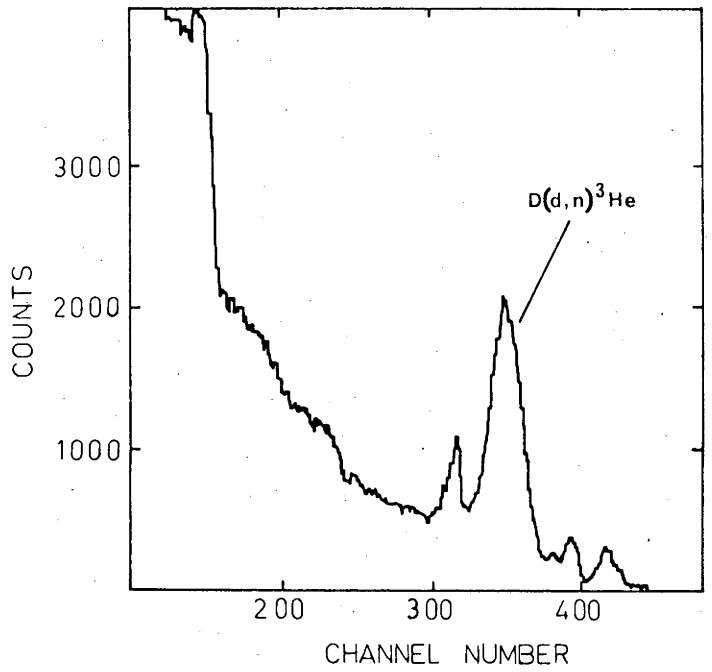

Figure (1.1)
The energy spectrum from a 1ØØ um silicon surface barrier detector at 34° (Lab.) with 22 MeV deuterons. The peak which needs to be unambiguously resolved, the ^{3}He peak, is situated in a region of high background.

Bartle and Quin (Ba74) went some way toward solving the identification problem of identifiying the ^{3}He events by incorporating a "veto" detector behind the main silicon surface barrier detector. By choosing a front detector just thick enough to stop ^{3}He ions of the required energy, the veto detector eliminated penetrating events in the front detector corresponding to the unwanted protons and

deuterons.

Later Bartle,Gebbie and Hollas (Ba77a) successfully adopted a particle identification technique using a silicon surface barrier detector telescope consisting of a "ΔE_1 ", "ΔE_2" and "veto" detectors. The particle identification unit used was designed by England (En73). This unit determines the function $MZ^2 = \Delta E_1 (ko + \Delta E_1 + \Delta E_2)$ where M and Z are the mass and charge of the detected particle respectively. This function is based on the variations used by Stokes, Northrop and Buyer (St58) of the first order solution to the standard Bethe energy loss equation

$$dE/dx = (C_1 MZ^2)[\log (C_2 E_T)/(MZ^2)] / E_T \qquad (1.2)$$

Ignoring the logarithmic term the solution of this equation yields $\Delta E_1 (\Delta E_1 + \Delta E_2) =$ constant x MZ^2 . The constant, ko, which is added in equation (1.1) enables the particle identification unit to be used over a large dynamic range with less restriction on the thickness of the transmission (ΔE_1) detector.

The successful application of this particle identification technique meant that the high degree of ^{3}He energy resolution previously required was no longer necessary. Consequently thicker targets could be used. Prior to this achievement targets had been limited to approximately 100 ug/cm^2 in order to provide good ^{3}He energy resolution. This not only meant that there was a small amount of target material, but also that the incident beam current had to be limited to approximately 300nA due to the fragile nature of the target. With the ^{3}He particle

identification technique described, the target thickness can successfully be increased to 5 mg/cm^2. The beam current was still limited to 300nA due to the increased heating of the foil, however, it was estimated that if the speed of the rotating target mechanism described by Bartle et al (Ba77) was increased from 60 revs/min to 240 revs/min then the beam current could be increased to 2 uA thus significantly improving the neutron yield.

[The rotating foil mechanism uses a foil 30mm in diameter, rotating such that the 2mm diameter deuteron beam traces out a circle on the foil thus distributing the heat over an area of more than 100mm^2.]

Despite this significant improvement, the neutron yield is still limited to about 5 x 10^2 neutrons/sec. Thus if the associated particle technique is to be used effectively it is important to choose the kinematic condition (the incident deuteron energy and the scattering angle) to optimize the neutron yield. In order to choose the optimum scheme, it is necessary to consider the ratio of the neutron cone angle to the ^{3}He cone angle and the D(d,n)^{3}He differential cross sections. The neutron cone angle is important only when the target to be irradiated is not large. The cone angle ratio varies by a factor of 2 over the acceptable kinematic schemes as is illustrated by Figure (1.2). In contrast to this the differential cross sections vary by more than an order of magnitude (see Figure (2.7)) and will have a significant effect on the neutron yield. Thus an accurate knowledge of the D(d,n)^{3}He differential cross sections is essential. Cross sections are required over the deuteron

energy range 18 to 26 MeV thus extending the cross section data to the upper limit of the A.N.U. Cyclotron-Tandem accelerator system. A single measurement made by Van Oers and Brockman (Va63) at 25.3 MeV provides the only data above 18 MeV. The present work sought to establish the differential cross sections for the energy range 18 to 26 MeV.

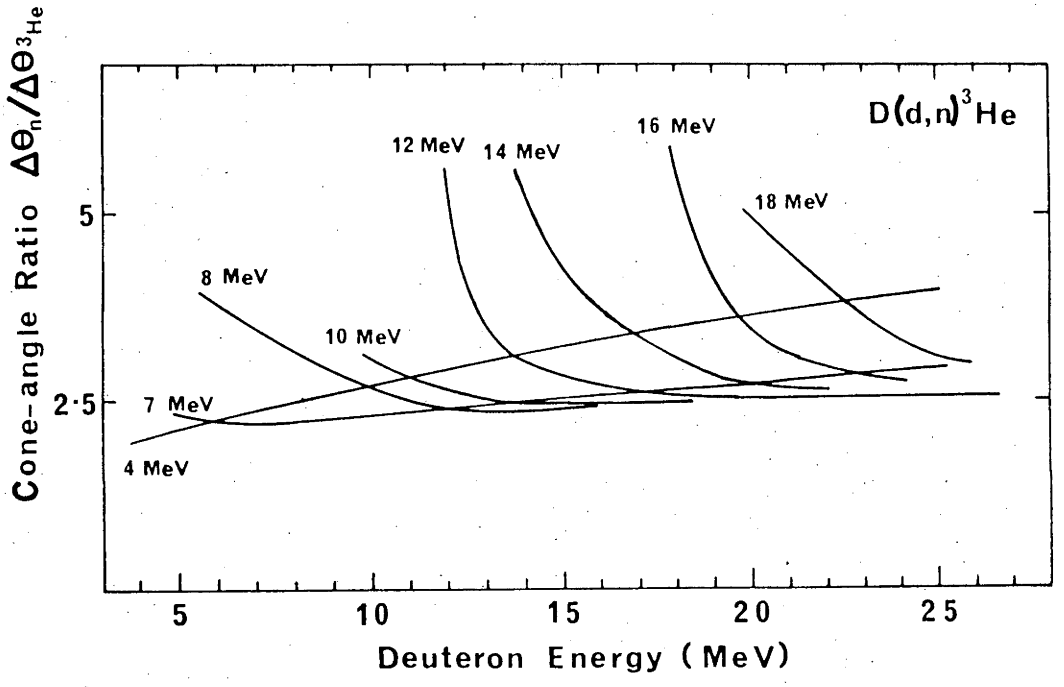

Figure (1.2)
The ratio of the neutron cone angle to the ^{3}He cone angle for the D(d,n)^{3}He reaction is plotted versus deuteron energy. Plots are shown for selected neutron energies. The narrowest neutron beams are obtained when the ratio is small.

1.3. Excited States in ^{4}He

From analysis of the summed energy spectra for the two

ejected protons from the $^{6}Li(\pi^{+},2p)^{4}He$ reaction, Tang (Ta66) suggested the existence of a 2^{+} state in ^{4}He at 30 MeV due to an S-wave d+d resonance of the type $^{5}S_{2}$. Later Werntz and Meyerhof (We68) refuted the S nature of the 2^{+} state and proposed instead a $^{1}D_{2}$ state on the basis of an R-matrix analysis of differential cross sections and neutron polarization in the $^{3}H(p,n)^{3}He$ reaction. Their analysis used the positions of other well established levels as given by Tombrello (To65) and Barrett, Meyerhof and Walecka (Ba66). They initially, freely varied the mixing parameter α, the energy of the assumed 2^{+} state, and the reduced deuteron width amplitude γ_{d} to obtain the best fit to the Legendre polynomial coefficients representing the differential cross section and polarization data. In the final fit the energies of all the levels were varied slightly.

A further attempt to verify the existence of the 2^{+} level in ^{4}He was carried out by Meyerhof, Feldman, Gilbert and O'Connell (Me69) with a study of the $^{2}H(d,\gamma)^{4}He$ reaction. The cross section was found to peak near 31 MeV; however it was concluded that the shape of the cross section was not consistent with a simple 2^{+} resonance in ^{4}He; rather it indicated a predominantly direct reaction mechanism.

In a study of d+d and $d^{*}+d^{*}$ systems using the method of resonating group structure with a one channel approximation, Thompson (Th70) obtained a resonance energy for the D state of about 32.3 MeV excitation in ^{4}He and a reduced width of 2.1 MeV. It was not clear whether this resonance corresponded to the 2^{+} state near 30 MeV predicted by Werntz

and Meyerhof, but the work did confirm that there is an l=2 anomaly in ^{4}He in this energy region. More recently, Erdas, Mosconi, Pompie and Quarati (Er70) predicted from cross section calculations for the ^{4}He(γ,d)d reaction, using the dispersive approach of Bosco (Bo61) with corrections for the interaction between the outgoing deuterons, that a 2^+ level should be located at 30 MeV, later [Erdas et al (Er71)] the estimate of the excitation energy was revised to 33 MeV with a reduced width γ^2 of 5 MeV, which would correspond to an observed width of 25 MeV for the present system.

As with Werntz and Meyerhof, all researchers have obtained the energy and the width of the level by assuming the 2^+ level does exist, and then varying its energy and width until a particular model provided the best representation of the experimental data. The subtle nature of the evidence to date makes further evidence highly desirable. Given that deuteron energies in the range 18 to 26 MeV incident on deuterium, correspond to excitation in ^{4}He between 32.85 and 36.85 MeV, it was hoped that measurements of the D(d,n)^{3}He differential cross section between 18 and 26 MeV might provide additional information about the proposed level in ^{4}He.

The measurement of the D(d,n)^{3}He differential cross sections is described in Chapter 2. A more detailed description of the ^{3}He detection system to be used in later experiments is included in Chapter 3 which discusses the neutron beam profile, how it was measured and how it can be represented. Part II discusses the application of the

associated particle neutron source to the problem of measuring n-p differential cross sections. Chapters 4 and 5 give an introduction to n-p scattering and some reasons why it is important. A Monte Carlo program which was used to assist in the analysis of the n-p scattering data is described in Chapter 6. The related detector response functions are dealt with in Chapter 7. Chapters 8 and 9 describe the n-p scattering experiments and how the Monte Carlo code was used in the analysis. Conclusions are drawn in Chapter 10.

2. $D(d,n)^3He$ DIFFERENTIAL CROSS SECTIONS

It is possible to observe either the emitted neutrons or the recoil ^3He particles in order to measure the differential cross sections of the $D(d,n)^3He$ reaction. The latter method was adopted in the present work despite the disadvantage of the primary deuteron beam limiting small angle measurements to 7° Lab. (approximately 17° c.m.). This limitation is of particular importance when fitting the data because of the strong peaking of the differential cross section in the forward direction. This limitation is, however, outweighed by the advantage of detecting ^3He ions over the detection of neutrons.

2.1. Experimental Procedure

A 3 mg/cm^2 self-supporting, deuterated-polyethylene target (Ba77) was bombarded with a deuteron beam from the ANU cyclotron injector† and the EN tandem accelerator system*. Beam currents ranging from 10 to 30 nA were used, the current being varied in order to maintain an essentially constant ^3He count rate of approximately 150 counts per second as the detector angle was varied. The beam diameter at the target was 2 mm. The target was mounted on a rotating target holder designed by Bartle (Ba77a) and was

† Model CNI-30 Cyclotron, The Cyclotron Corporation, 950 Gilman St., Berkeley, California, USA.
* EN Electrostatic Accelerator, High Voltage Engineering Corporation, Burlington, Massachusetts, USA.

rotated at 60 revs/min. The axis of rotation was parallel to, but not coincident with the deuteron beam.

The ^{3}He recoils were measured with a silicon surface barrier detector telescope as used by Bartle et al (Ba77a). The telescope consisted of a "E_1 - E_2 - veto" configuration using detectors of thickness 30, 490 and 100 microns respectively. The detector telescope was mounted on a rotating platform. The transmitted beam was measured in a Faraday cup mounted 339 cm from the target, and a 2000 micron silicon surface barrier detector fixed at approximately 35° to the transmitted beam direction monitored the target yield. The experimental arrangement is shown schematically in Figure (2.1). The detector telescope was mounted behind a collimator housing which contained three rectangular collimators and electron suppression magnets. The full angle subtended by the slit system was 0.44° on the horizontal plane (the plane of the experiment) and 1.76° in the vertical plane, corresponding to a solid angle of 0.24 msr. The collimator block for the monitor detector subtended 0.44° in the horizontal plane and 2.26° in the vertical plane, corresponding to a solid angle of 0.31 msr.

At each of the incident deuteron energies of 18, 20, 22, 24 and 26 MeV the ^{3}He yield was measured from 7° to 35° in the laboratory system in 15 steps, corresponding to a range of approximately 17.5° to 95° in the centre of mass system. The measurements were made at 1.0° (Lab.) intervals for the smaller angles and at 2.5° (Lab.) at the larger angles. The closer spacing of measurements at the smaller

angles were necessary to ensure a good fit of the strong forward peak.

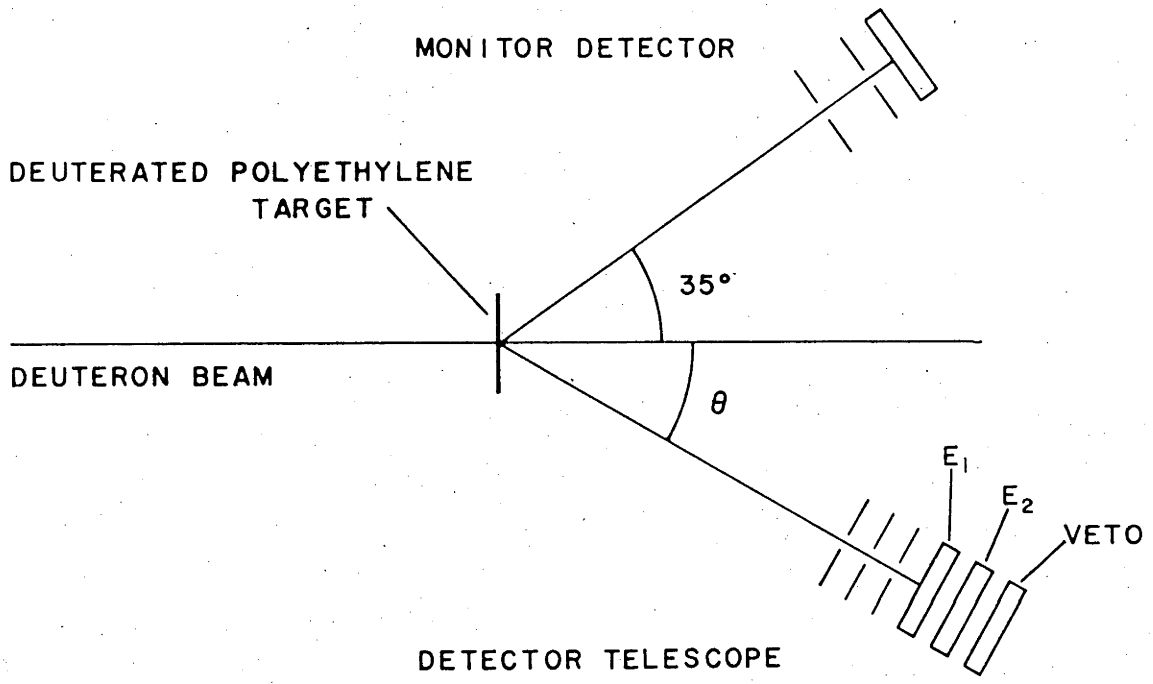

Figure (2.1)
A rotating self-supporting deuterated polyethylene target was bombarded with a deuteron beam. The recoil ^{3}He ions were detected using a silicon surface barrier detector telescope. A monitor detector was used in conjunction with a Faraday cup collecting the transmitted beam to monitor the target yield and to provide normalization of angular distributions at consecutive energies.

The detector signals were analyzed using a particle identification unit (En73) incorporated into the circuit shown in Figure (2.2). The spectrum proportional to "MZ^2" and the total energy spectrum are shown in Figures (2.3) and (2.4) respectively.

The "MZ^2" spectrum shows the ^{3}He and the ^{4}He groups distinctly separated. The two spectra were recorded in event mode enabling projections to be made of either spectrum with a window on the other, and thus allowing accurate determination of the ^{3}He yield.

There was some contamination of the ^{3}He spectrum due to the $^{12}C(d,^3He)^{11}B$ reaction. It can be seen from the kinematics shown in Figure (2.5) that the ^{3}He energy from the $D(d,n)^3He$ reaction is larger than that from the $^{12}C(d,^3He)^{11}B$ reaction for all but the largest angles measured. Thus at these angles the peak of interest will be superimposed on ^{3}He peaks from the $^{12}C(d,^3He)^{11}B$ reaction. The magnitude of the contamination was accurately estimated by means of measurements with a carbon target.

It should be noted for all deuteron energies above 3.29 MeV, at any particular angle, that the $D(d,n)^3He$ reaction produces two different ^{3}He energies (see Figure (2.5)). Only the higher energy group was detected as ^{3}He ions with energies less than 5.4 MeV were stopped in the E_1 detector.

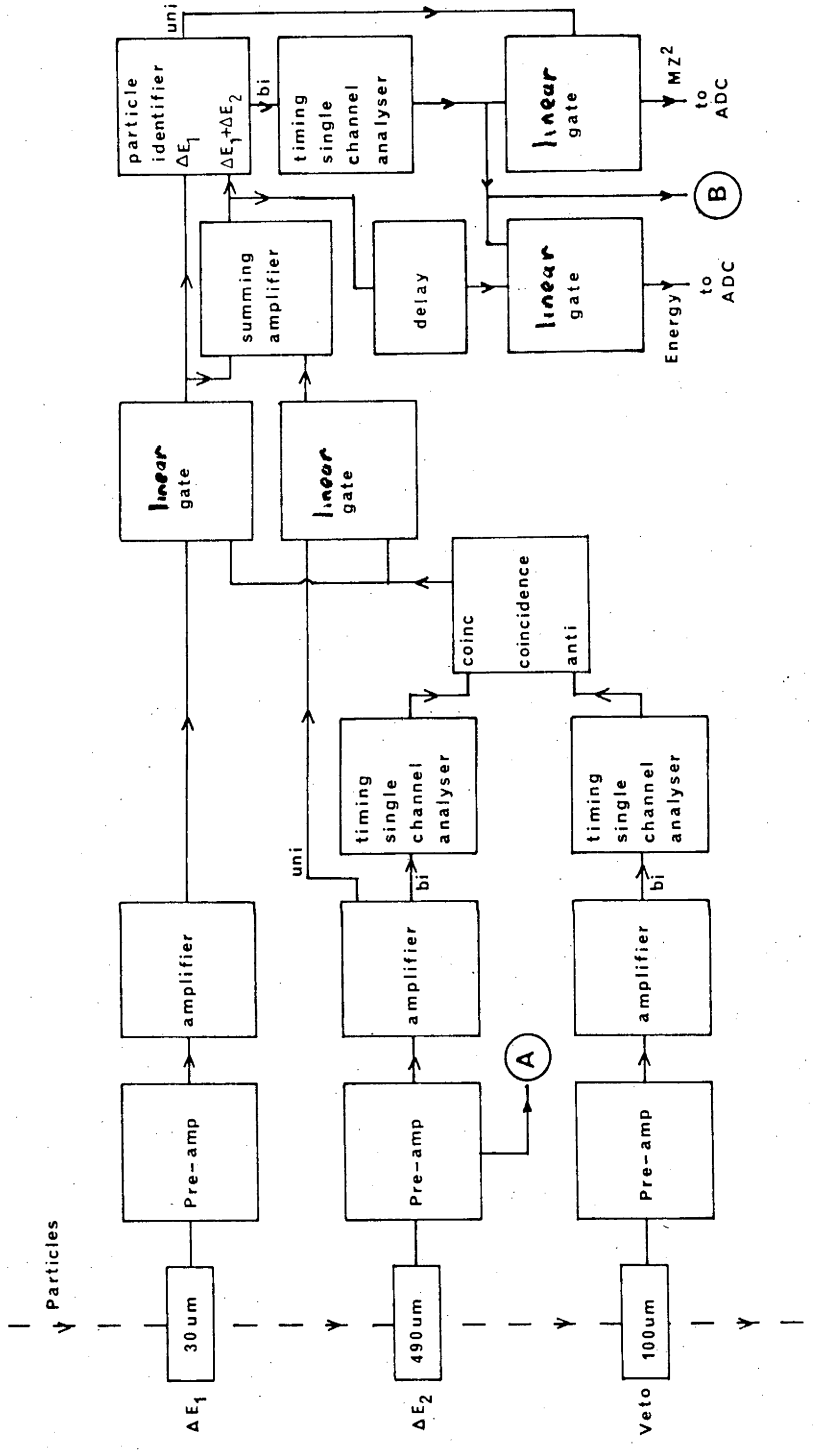

Figure (2.2)
Circuit diagram of the ^{3}He identification system.

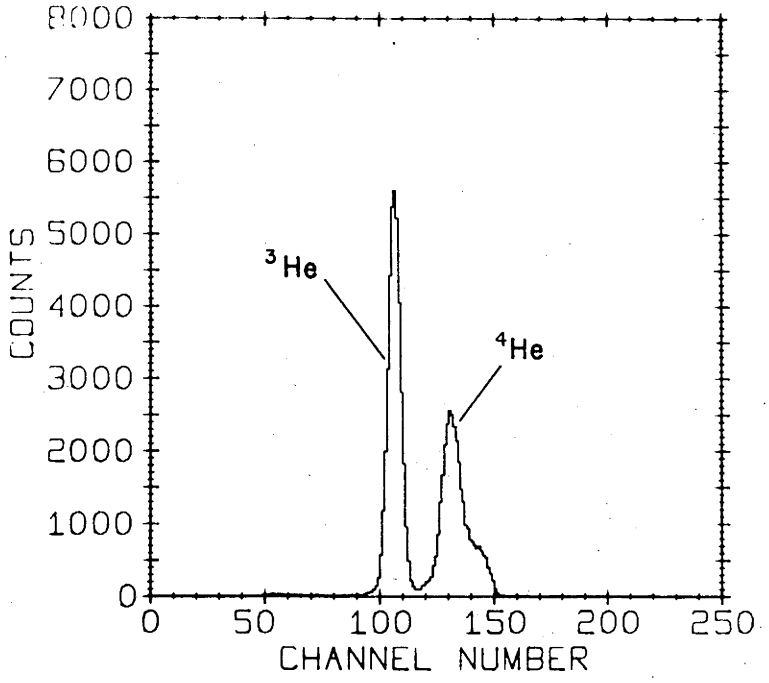

Figure (2.3)
The MZ^2 spectrum produced by the particle identification unit. The distinct separation of the ^{3}He and ^{4}He groups is clearly shown. A window was set on the ^{3}He peak to produce the ^{3}He energy spectrum shown in Figure (2.4).

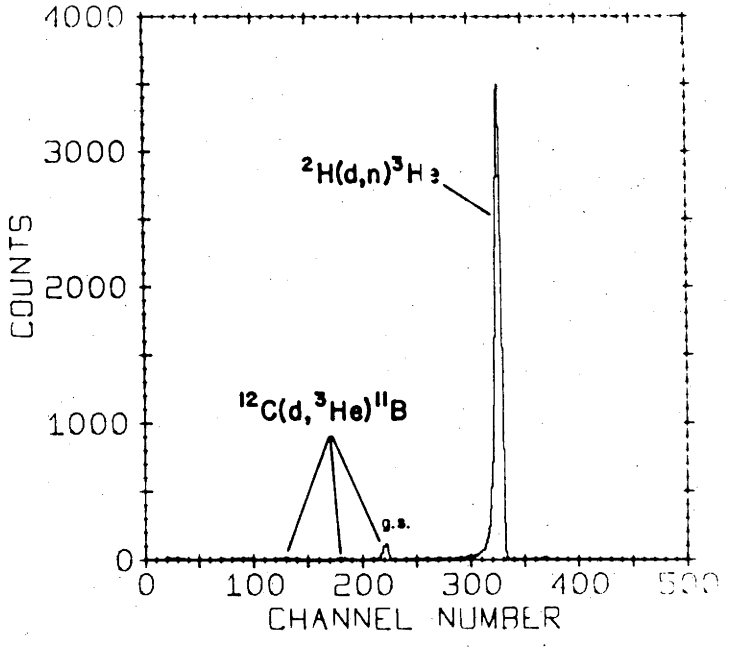

Figure (2.4)
The projection of the total energy spectrum with a window on the ^{3}He peak of the MZ^2 spectrum shown in Figure (2.3). Incident deuteron energy was 26 MeV with a ^{3}He scattering angle of 22.5° (Lab.).

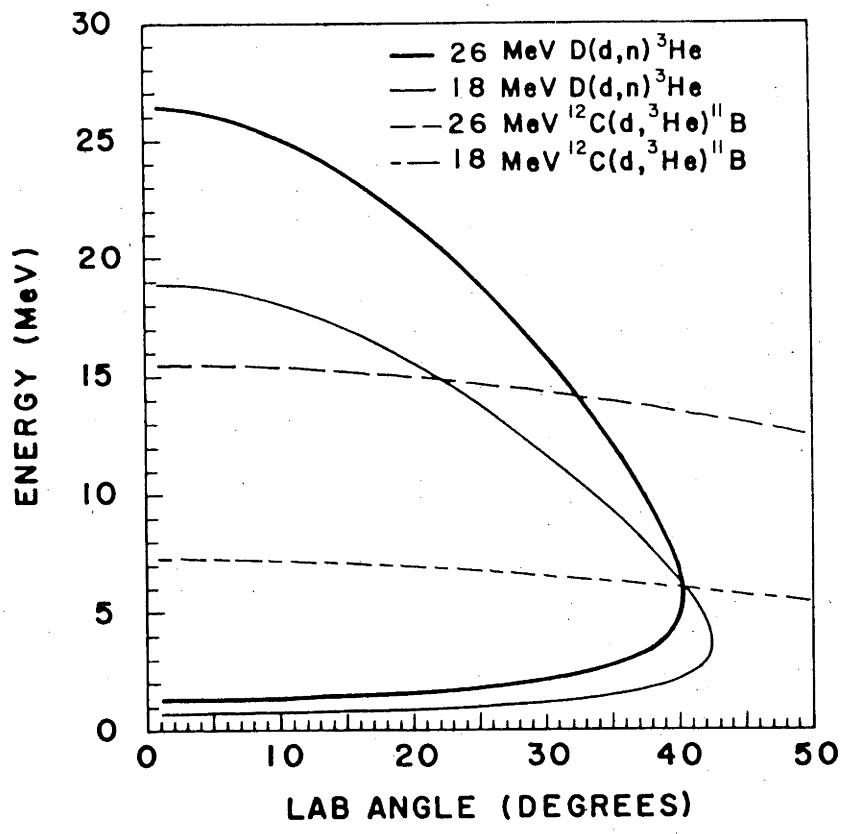

Figure (2.5)
A plot of the ^{3}He energies for the reactions D(d,n)^{3}He and ^{12}C(d,^{3}He)^{11}B for 18 and 26 MeV deuterons.

2.2. Results

The angular distributions were obtained by normalizing the ^{3}He yield obtained with the detector telescope particle identification system to the yield of the fixed monitor detector. Normalization of distribution at consecutive energies was governed by the change in the ratio of the monitor yield to the total collected charge. This ratio was dependent upon four items: the absolute value of the D(d,n)^{3}He cross section; the shape of the differential cross section; the centre of mass solid angle of the monitor

detector; and the target yield. The ratio of the monitor yield to the collected charge provided a combined measure of the first three quantities as long as the target yield was constant.

By plotting the number of monitor counts per collected charge for each data point versus the sum of the collected charge it was found that the target yield decreased by less than Ø.1% per 1ØØ uC of collected charge. The plot is shown in Figure (2.6). Over the range of two consecutive measurements (approximately 2Ø uC) the expected variation in the target yield was less than Ø.Ø2%. The horizontal nature of the lines at each energy in Figure (2.6) shows the essentially constant target yield, and the difference between the lines for different energies gave the change in the monitor yield due to cross section and solid angle differences. In order to normalize angular distributions at consecutive energies the ratios of the monitor yield to the collected charge for the last measurement at one energy and the first measurement at the next energy were compared.

The angular distributions thus obtained are presented in Table (2.1) and Figure (2.7). The 18 MeV data were normalized to the results of Dietrich, Adelberger and Meyerhof (Di72) to provide absolute cross sections.

Even order Legendre polynomials of the form

$$d\sigma/d\Omega\,(cm) = \sum_{n=0}^{n_{max}} A_{2n} P_{2n}(\cos\theta) \qquad (2.1)$$

were least squares fitted to the angular distributions (Table (2.2)). Only even order Legendre polynomials are required because the distributions are symmetric about 9Ø°

(c.m.) as a consequence of the identical nature of the incident and target particles. It may be possible that contaminants may have caused the breakthrough of odd order polynomials. The fitting of a combination of even and odd order polynomials was attempted but the coefficients obtained were not meaningful and provided no improvement over the fit obtained from only even order polynomials. Thus in the absence of the data beyond 90° c.m. which would be required to enable satisfactory fitting of odd order polynomials, and in view of the good fit achieved using only even order polynomials, it was not considered beneficial to pursue further the fitting of odd order polynomials.

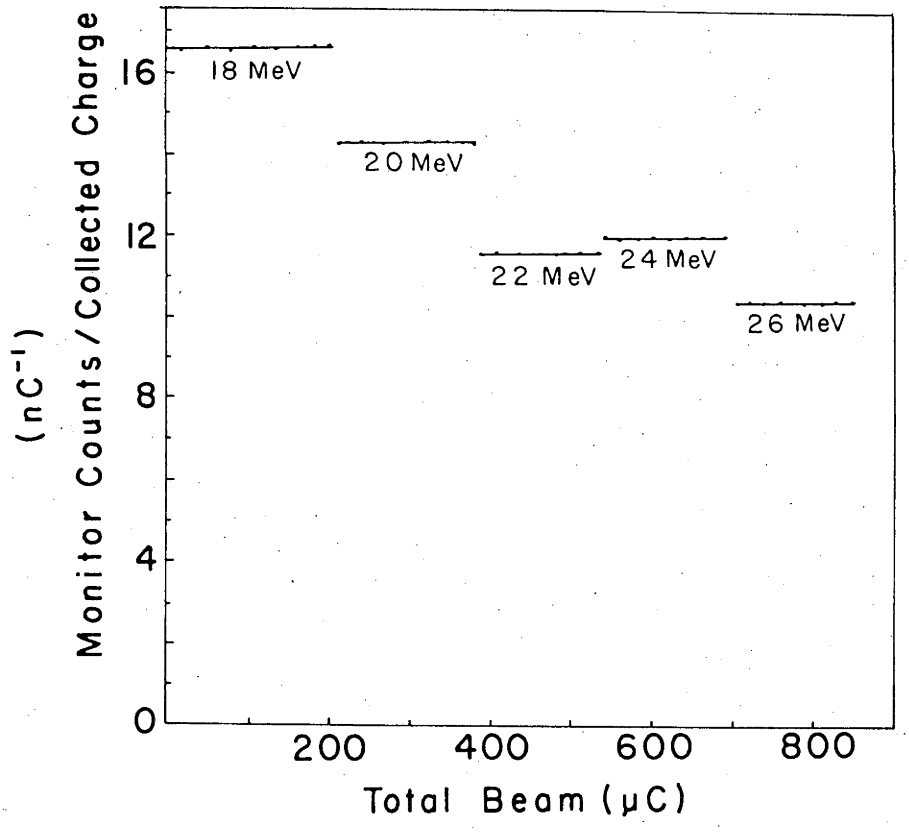

Figure (2.6)
Plot showing monitor counts per collected charge for each data point versus total collected charge.

Table (2.1)
$D(d,n)^3He$ c.m. differential cross sections.

18.Ø MeV		2Ø.Ø MeV		22.Ø MeV	
c.m. (deg)	$\frac{d\sigma}{d\Omega}$ (mb/sr)	c.m. (deg)	$\frac{d\sigma}{d\Omega}$ (mb/sr)	c.m. (deg)	$\frac{d\sigma}{d\Omega}$ (mb/sr)
17.4	25.54±Ø.31	17.6	23.76±Ø.37	17.7	21.44±Ø.33
19.9	21.92±Ø.31	2Ø.2	19.43±Ø.33	2Ø.2	17.68±Ø.31
22.4	17.28±Ø.24	22.6	15.Ø8±Ø.25	22.8	13.38±Ø.24
24.9	13.5Ø±Ø.21	25.1	11.63±Ø.21	25.3	1Ø.13±Ø.2Ø
27.4	9.61±Ø.18	27.7	8.2Ø±Ø.17	27.9	7.Ø5±Ø.15
32.5	4.96±Ø.11	32.8	4.13±Ø.Ø9	33.Ø	3.64±Ø.Ø8
37.6	2.92±Ø.Ø5	37.9	2.62±Ø.Ø5	38.2	2.5Ø±Ø.Ø4
44.Ø	2.52±Ø.Ø3	44.3	2.74±Ø.Ø4	44.7	2.84±Ø.Ø5
5Ø.4	3.47±Ø.Ø4	5Ø.9	3.77±Ø.Ø5	51.3	3.88±Ø.Ø5
57.Ø	4.26±Ø.Ø4	57.6	4.5Ø±Ø.Ø4	58.Ø	4.59±Ø.Ø5
63.8	4.49±Ø.Ø3	64.4	4.58±Ø.Ø4	64.9	4.57±Ø.Ø5
7Ø.6	4.16±Ø.Ø4	71.4	4.Ø3±Ø.Ø5	72.Ø	3.87±Ø.Ø5
77.8	3.5Ø±Ø.Ø4	78.6	3.21±Ø.Ø4	79.4	2.93±Ø.Ø4
85.2	3.Ø1±Ø.Ø3	86.2	2.65±Ø.Ø3	87.1	2.28±Ø.Ø4
93.1	2.86±Ø.Ø3	94.3	2.68±Ø.Ø4	95.5	2.36±Ø.Ø5

24.Ø MeV		26.Ø MeV	
c.m. (deg)	$\frac{d\sigma}{d\Omega}$ (mb/sr)	c.m. (deg)	$\frac{d\sigma}{d\Omega}$ (mb/sr)
17.8	2Ø.65±Ø.34	17.9	19.86±Ø.34
2Ø.3	17.31±Ø.29	2Ø.4	15.23±Ø.29
22.9	12.98±Ø.24	23.Ø	11.69±Ø.22
25.5	9.39±Ø.2Ø	25.6	8.27±Ø.18
28.Ø	5.98±Ø.13	28.2	5.88±Ø.13
33.2	3.27±Ø.Ø7	33.4	3.Ø8±Ø.Ø6
38.4	2.63±Ø.Ø3	38.6	2.53±Ø.Ø6
45.Ø	3.51±Ø.Ø5	45.2	3.4Ø±Ø.Ø5
51.6	4.54±Ø.Ø5	51.9	4.49±Ø.Ø5
58.4	5.14±Ø.Ø5	58.8	4.87±Ø.Ø5
65.4	5.Ø3±Ø.Ø6	65.8	4.47±Ø.Ø5
72.6	3.93±Ø.Ø5	72.7	3.55±Ø.Ø5
8Ø.Ø	2.87±Ø.Ø5	8Ø.6	2.42±Ø.Ø7
87.9	2.22±Ø.Ø5	88.6	1.81±Ø.Ø7
96.4	2.29±Ø.Ø6	97.3	2.Ø8±Ø.Ø5

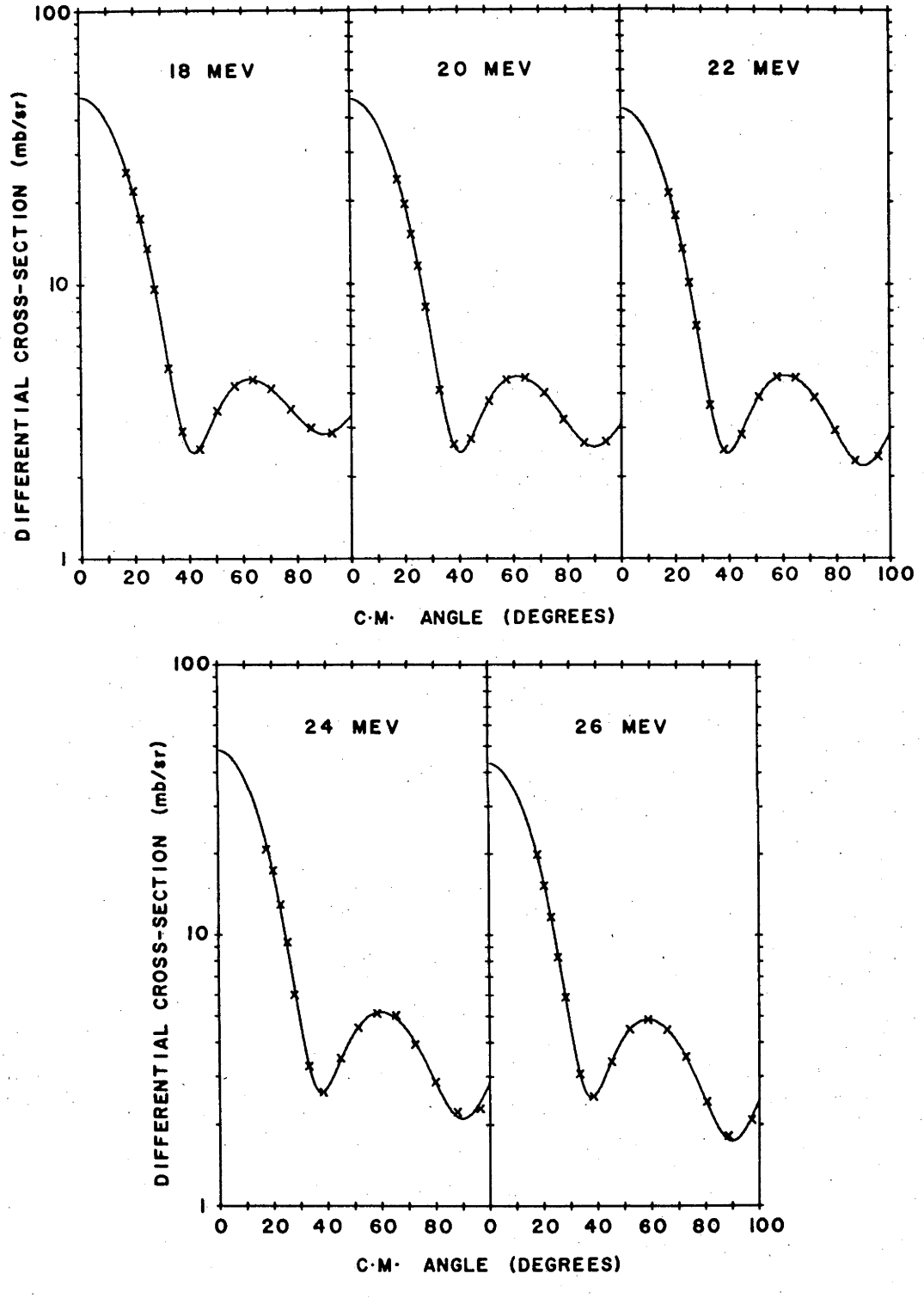

Figure (2.7)
The differential cross sections are shown with the fitted Legendre polynomial curves.

The errors assigned to the data points for the purpose of the fit were the statistical uncertainties plus the uncertainty due to the error in the scattering angle which was taken to be ±Ø.1 . The uncertainty in the cross sections due to this error depends on the slope of the angular distributions. The extreme limit was +1.4% at the highest energy and steepest slope. The errors given to the coefficients in Table (2.2) are the least squares fitting errors. When the inclusion of the highest order coefficient gave little or no improvement in the fit, the expansion was terminated. It was found that order 1Ø was sufficient for energies 18, 2Ø and 22 and order 12 for energies 24 and 26 MeV. Figure (2.8) shows a plot of the A_o coefficients and the normalized coefficients A_L/A_0.

It should be noted that the data taken by Van Oers and Brockman (Va63), who measured the differential cross sections for the $D(d,n)^3He$ reaction at 25.3 MeV, have an absolute value of approximately 4Ø% lower than the value one would expect from the current data normalized to the work of Dietrich, Adelberger and Meyerhof (Di72). Van Oers and Brockman did not fit Legendre polynomials to their data so Legendre polynomials were fitted using the same procedure as used for our own data. The discrepancy is quite obvious in the plot of A_o in Figure (2.8) whereas values for all other coefficients are in good agreement.

Van Oers and Brockman used a deuterium gas target and obtained their absolute differential cross section by measuring the gas pressure and the incident deuteron beam. Whereas Dietrich et al obtained their absolute values by

Table (2.2) Least squares Legendre polynomial fits to c.m. angular distributions.

	ENERGY (MeV) 18	20	22	24	26
A_0	6.12±.03	5.87±.03	5.54±.03	5.73±.03	5.30±.03
A_2/A_0	1.78±.01	1.72±.01	1.65±.02	1.59±.02	1.63±.02
A_4/A_0	2.26±.02	2.14±.02	2.00±.02	1.85±.03	1.80±.03
A_6/A_0	2.08±.02	2.18±.03	2.22±.03	2.32±.03	2.34±.03
A_8/A_0	.67±.02	.78±.03	.78±.03	.93±.03	.94±.03
A_{10}/A_0	.11±.02	.16±.02	.19±.02	.27±.02	.25±.03
A_{12}/A_0				.06±.03	.03±.03
σ_T (mb)	77.8	74.2	68.9	71.0	65.8

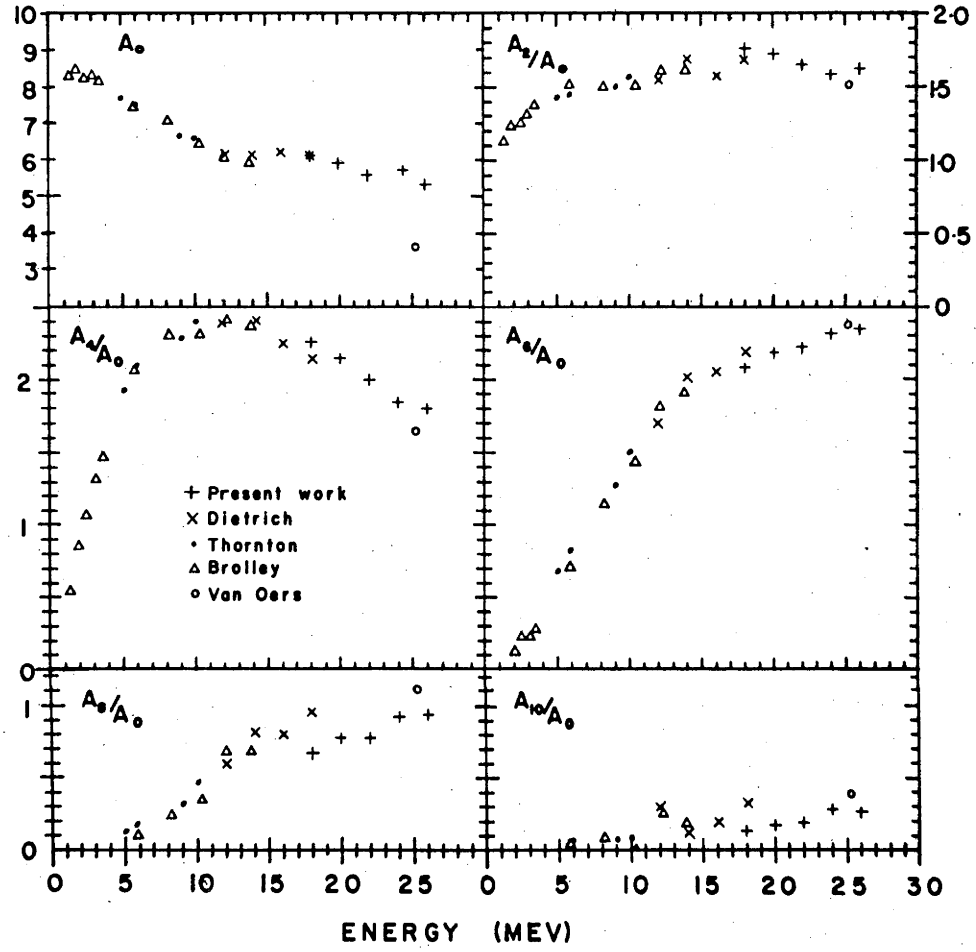

Figure (2.8)
The zeroth order Legendre polynomial coefficients and the normalized higher order coefficients for the current work are shown compared to earlier work of Dietrich et al (Di71), Thornton (Th69), Brolley et al (Br57) and Van Oers et al (Va63).

normalization against the measurements of Brolley, Putman and Rosen (Br57) who used photographic emulsions. Van Oers and Brockman counted the elastically scattered deuterons at 20° (Lab.) in conjunction with a Faraday cup measuring the incident deuteron beam to provide their absolute values. This is considered to be a more reliable technique than relying on a knowledge of the quantity of deuterium present in a multiplate camera and trying to count every ^{3}He event. There is thus a tendency to favour the technique of Van Oers and Brockman for establishing absolute values. In the light of this it is therefore possible that A_0 could be 40% lower.

If further measurements are to be made using a similar approach to the current method it is recommended that the information collected from the detector telescope or the monitor should include the elastically scattered deuterons. Doing so would enable accurate normalization of the angular distributions taken at each energy with the elastic scattering cross sections.

2.3. The 2^+ State in ^{4}He

The coefficients shown in Figure (2.8) follow the trends indicated by the lower energy data and thus further analysis as performed by Dietrich, Adelberger and Meyerhof would not yield any further information. The absence of any striking features attributable to the proposed resonance does not disprove the existence of the 2^+ state in ^{4}He for two reasons. Firstly, the broad nature of the proposed resonance, which was predicted to have a reduced width of 5

MeV, and thus a much wider experimental width, may be obscuring the effect. Secondly, the $D(d,n)^3He$ reaction may be a predominantly direct reaction, thus not yielding information about the ^4He system.

3. NEUTRON BEAM PROFILE

3.1. Introduction

An accurate knowledge of the neutron beam profile is essential if the $D(d,n)^3He$ reaction is to be used effectively as a neutron source of known flux and known energy spread. Such information enables the correct choice of scintillator size and separation from the source necessary to encompass the entire neutron beam. The parameters describing the beam profile are also necessary for Monte Carlo calculations involving neutrons from the source.

3.2. Experimental Method

The beam profile was measured using an NE102 scintillator mounted on an RCA8575 photomultiplier tube connected to an Ortec 269 tube base. The scintillator, with a diameter of 1.75 cm, was located 100.0 cm from the source thus subtending a solid angle of only 0.24 msr (0.79 deg^2). The experimental arrangement is shown in Figure (3.1). The electronics used were the ^3He particle identification system as described in Chapter 1 (Figure (2.2)) and a "time of flight" measuring system as shown in Figure (3.2). Two spectra were collected for each datum point: the pulse height spectrum of the scintillator; and the time of flight spectrum. The scintillator was moved in one degree steps in

both the horizontal and the vertical directions.

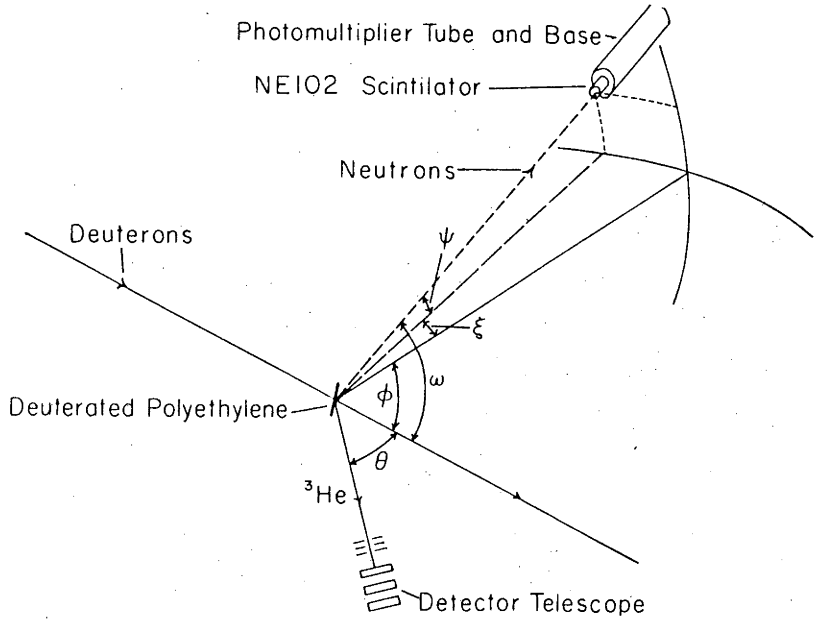

Figure (3.1)
Schematic diagram of the experimental arrangement. Angles θ and ϕ are is the same plane, being the ^{3}He detection and neutron production angles respectively. Angles ξ and ψ give the position of the detector relative to the angle ϕ in the horizontal and vertical directions. Angle ω is the total scattering angle for a detected neutron.

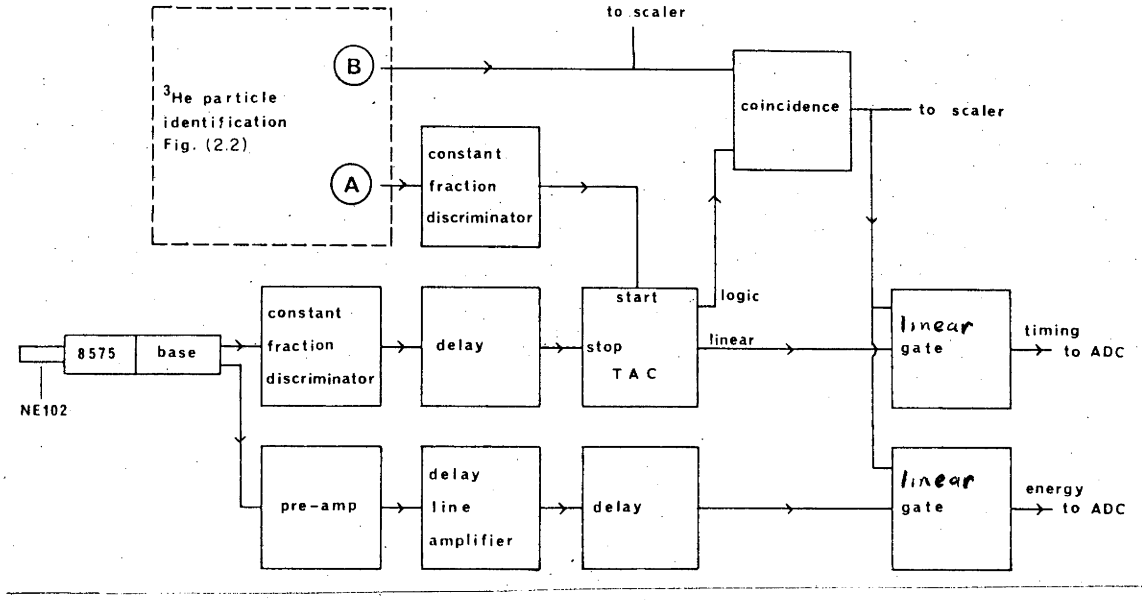

Figure (3.2)
Circuit diagram used for measurement of the neutron beam profile. The dashed area contains the circuit shown in Figure (2.2).

3.3. Results

The timing spectra obtained using the ^{3}He fast pulse as a start and the delayed output of a constant fraction discriminator connected to the fast output of the 269 tube base as the stop signal had a very good peak to background ratio (Figure (3.3)). This enabled accurate determination of the number of neutron events by means of simple integration and background subtraction.

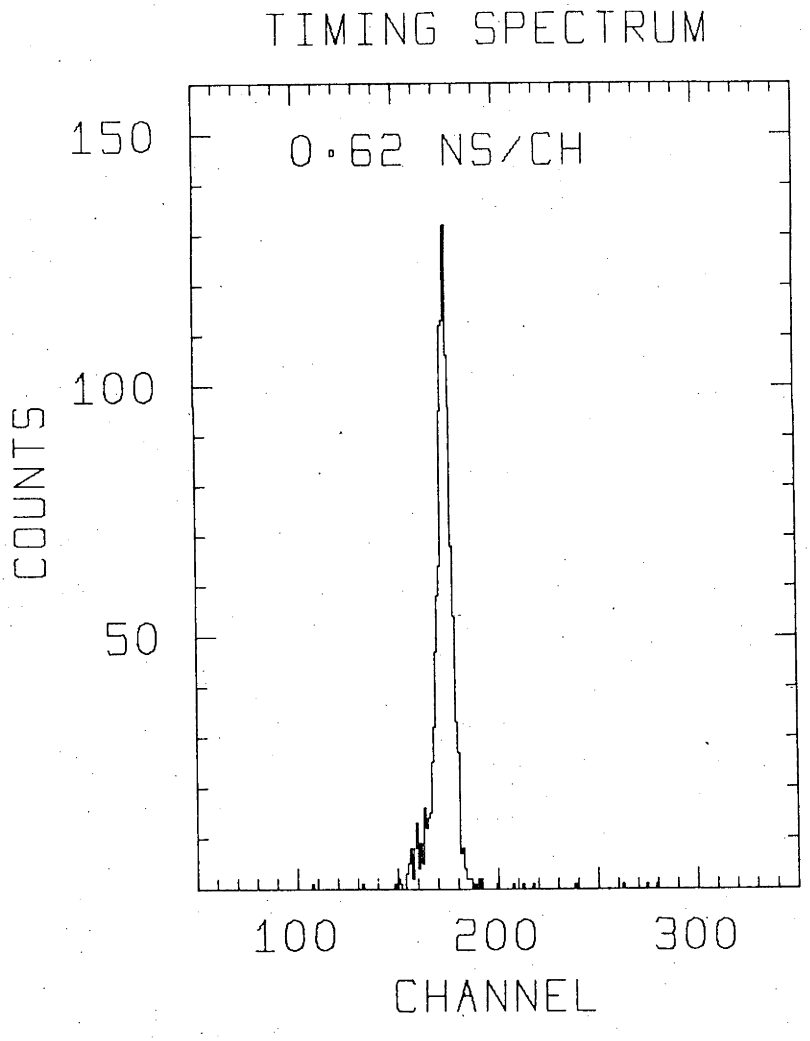

Figure (3.3)
The timing spectrum for 8 MeV neutrons produced by 12 MeV deuterons at ϕ =68.1° when ξ =1° and ψ =0°.

The lower level energy discrimination for the ^{3}He system was set by the ^{3}He constant fraction discriminator to ensure that the same energy range applied to both the timing start pulses and the ^{3}He logic pulses.

A narrow window set on the ^{3}He peak of the mz^2 spectrum (Figure (2.3)) produced by particle identification system. Such a window possibly excluded a small percentage of the ^{3}He events but was considered an acceptable compromise in order to exclude ^{4}He events completely. An "approximate" beam profile was obtained by dividing the number of scintillator neutron events which were obtained from the timing spectra, corrected for deadtime, by the number of ^{3}He logic pulses. Such a beam profile is given in Table (3.1) for 9.514 MeV neutrons produced at a scattering angle of 73.5° using 18 MeV deuterons. To these data a Gaussian of the form

$$C(x) = A/(\sigma\sqrt{2\pi}) \exp(\tfrac{-1}{2}((x-u)/\sigma)^2) \qquad (3.1)$$

where x is the scattering angle, either vertical or horizontal, σ is the standard deviation and u the mean, was least squares fitted. "A" is a constant. For data in the horizontal plane with a vertical deflection $\psi = 0°$, A=5508, σ=1.48 and u=-0.45. For the vertical plane with a horizontal deflection $\xi = 0°$, A=6202, σ=1.71 and u=-0.19 . The means of the two Gaussians are not zero partly due to misalignment of the apparatus and partly due to the variation of the neutron detector efficiency with energy. The neutron beam is thus well collimated with, in this case, 95.4% of the neutrons falling within 5.92° in the horizontal plane and 6.84° in the vertical plane. This information is

sufficient to allow the calculation of the scintillator size required to encompass the entire beam. However, it is not sufficiently accurate to be used as input data specifying the shape of a neutron beam in a Monte Carlo calculation. The efficiency of the scintillator to neutrons of differing energy must be considered.

Table (3.1)
An 'approximate' beam profile obtained by
c=(number of neutrons detected x 1ØØØØ)/(number of ^{3}He's)

ψ \ ξ	-6°	-4°	-2°	Ø°	2°	4°	6°
4°				51	27		
2°		58	296	65Ø	249	33	
Ø°	4	142	841	1425	363	4Ø	Ø
-2°		99	57Ø	847	181	21	
-4°		17	67	82	4Ø	8	

Efficiency measurements were carried out immediately following the beam profile measurements by moving the scintillator in to 17.Ø cm from the source without altering discriminator or gain settings. At this distance the scintillator subtended a solid angle of Ø.66msr(2.17 deg^2). For 8 MeV neutrons produced at 68.1° with 12 MeV deuterons, a Gaussian fit to the approximate beam profile yielded σ_V'=1.14 and σ_H'=1.43, which meant that the scintillator encompassed 96.4% of the neutron beam. The relative efficiency for the scintillator is thus given by

$$\epsilon = (\#\text{ of neutron events})(\text{dead time correction}) \;/\; (\#\,^3\text{He's}) \qquad (3.2)$$

Efficiency measurements were made at 7.Ø85, 7.511, 8.Ø16, 8.5Ø5 and 8.978 MeV by varying the detection angle. These are the average energies of the neutron beam incident upon

the detector. The average efficiency can, to a good approximation, be regarded as the efficiency for monoenergetic neutrons because the gradient of the efficiency versus energy function is small and approximately constant. These data were least squares fitted with a Gaussian function such that

$$\varepsilon(E) = 0.0564 \exp(-((E-9.166)/1.005)^{2}) + 0.0845 \quad (3.3)$$

with the restriction that $7.0 < E < 9.0$ MeV. The choice of function was purely empirical; the only criterion being that it provide a means of accurately interpolating the efficiency data. This criterion is shown to be fulfilled by Figure (3.4). A single set of beam profile measurements for an 8 MeV neutron beam involves measurements over horizontal (ξ) and vertical (ψ) angles ranging from -6° to $+6^{\circ}$ corresponding to the detection of neutrons with energies ranging from 7.2 to 8.8 MeV. It is therefore necessary to correct the approximate beam profile for detection efficiency.

The total scattering angle ω for a neutron detected at the position given by ξ and ψ, when the centroid scattering angle is ϕ (Figure (3.1)), is given by

$$\omega = \arccos\{\cos(\phi+\xi)\cos(\psi)\} \quad (3.4)$$

Thus using kinematics the neutron energy can be determined and the appropriate detector efficiency evaluated by equation (3.3). Table (3.2) shows a sample of the data for $\psi=0^{\circ}$ and $-6^{\circ} = < \xi = < 6^{\circ}$. A least squares fitted Gaussian of the form given in equation (3.1) yields the horizontal parameters $A_H(0)=5507$, $u_H(0)=-0.12$ and $\sigma_H(0)=1.50^{\circ}$.

Table (3.2)

Beam profile measurements for $\psi = 0^\circ$ and $-6^\circ < \xi > 6^\circ$ are shown with the appropriate energy of the detected neutron and the detector efficiency which is used to correct the beam profile data. The errors for the final results given in the right most column not only include the statistical uncertainties as shown for the raw data and the efficiency measurements, but also take into account the error introduced due to an alignment uncertainty of $\pm 0.1^\circ$. The final data points shown here are plotted as 'x' in Fig. .5.

ξ	#TAC x 1000 / #^{3}He	Energy (MeV)	Relative Efficiency	#TAC x 1000 / #^{3}He x Efficiency
-6	.8±60.%	8.845	.1380±2.4%	6 ± 5
-5	4.9±20.%	8.705	.1352±2.4%	36 ± 15
-4	12.5±12.%	8.565	.1316±2.5%	95 ± 30
-3	33.1±7.6%	8.424	.1274±2.7%	260 ± 69
-2	77.7±4.8%	8.284	.1228±2.8%	633 ± 119
-1	141.6±3.9%	8.144	.1181±2.8%	1199 ± 144
1	107.6±4.1%	7.863	.1088±2.8%	989 ± 126
2	50.7±6.1%	7.723	.1045±2.8%	485 ± 92
3	24.5±8.6%	7.783	.1007±2.8%	243 ± 59
4	7.8±15.%	7.442	.0974±2.7%	80 ± 28
5	1.4±43.%	7.302	.0945±2.6%	15 ± 10
6	1.2±50.%	7.162	.0921±2.5%	13 ± 10

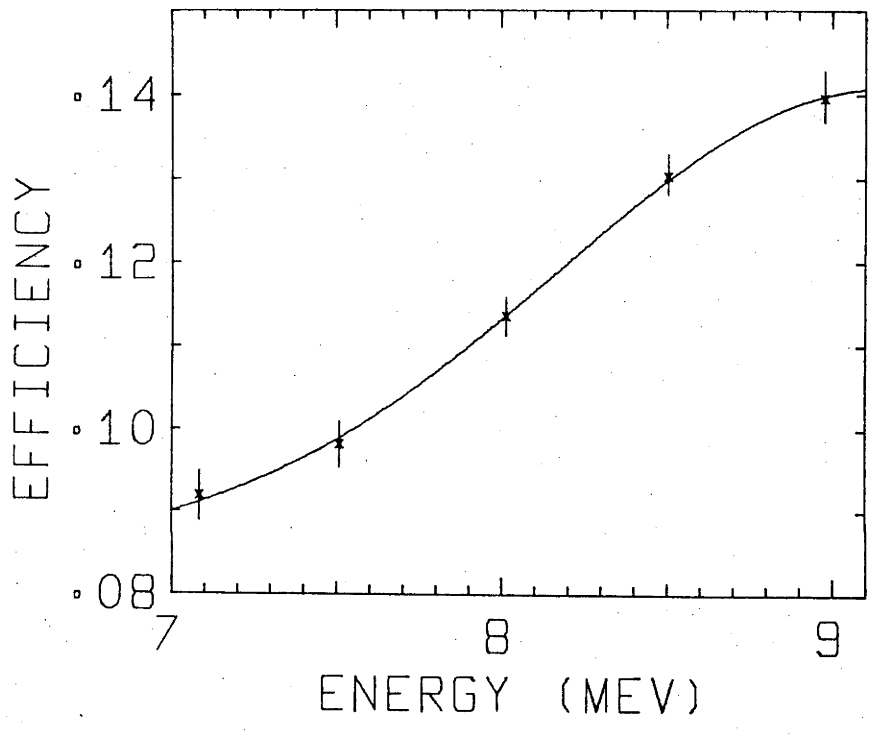

Figure (3.4)
Efficiency data for the beam profile scintillator fitted with the curve given by
$\varepsilon(E) = 0.0564\exp(-((E-9.166)/1.005)^{2}) + 0.0845$

For data taken in the vertical plane at $\xi=0^{\circ}$, the least squares fit yields $A_v'(0)=6435$, $u_v'(0)=-0.76$ and $\sigma_v'(0)=1.46^{\circ}$. Evaluating the later Gaussian at 0, 1, 2 and 3 gives

Ψ	$C_v(\Psi)/C_v(0)$	$A_H(\Psi)$
0	1.00	5507.
1	.55	3048.
2	.19	1056.
3	.04	230.

The Gaussians thus assumed for the data points in the various horizontal planes determined by different values of Ψ are given by the values of $\sigma_H(0)$ and $u_H(0)$ as fitted to the $\Psi=0^{\circ}$ data, with an amplitude given by

$$A_H(\Psi) = A_H(0)\, C_v(\Psi)/C_v(0) \qquad (3.5)$$

A plot showing the data and the Gaussian curves is shown in Figure (3.5). This clearly demonstrates that a good fit to the shape of the neutron beam profile is given by two Gaussian distributions, one for the horizontal direction and one for the vertical direction.

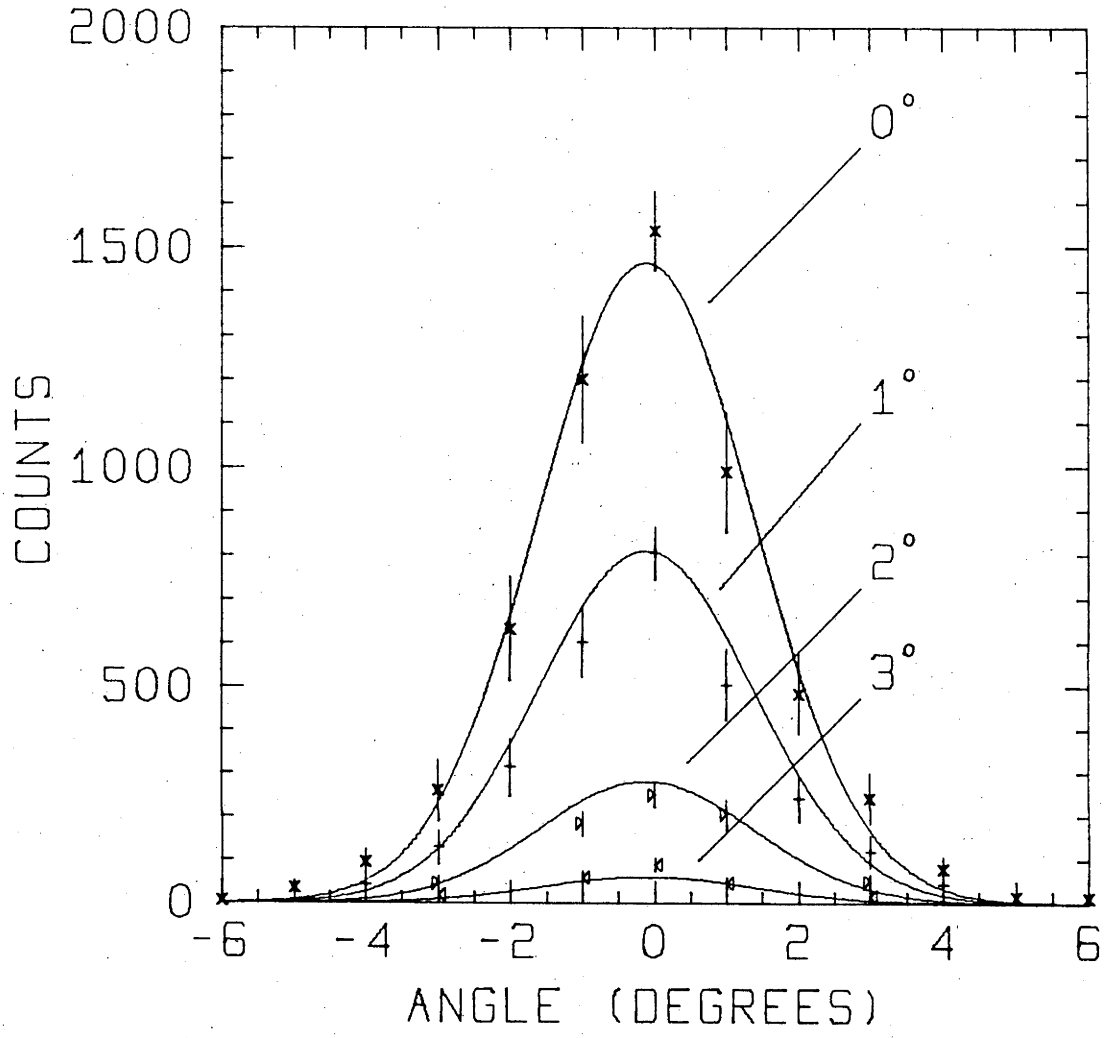

Figure (3.5)

Beam profile data points for four horizontal planes corresponding to $\psi = 0°$, $1°$, $2°$ and $3°$ are shown with Gaussian curves all having the same mean and standard deviation as the curve fitted to the $\psi = 0°$ data. The amplitudes for the curves with $\psi = 1°$, $2°$ and $3°$ were determined by the Gaussian fitted to the data in the vertical plane at $\xi = 0°$.

4. INTRODUCTION TO N-P SCATTERING

A fundamental problem in nuclear physics is the understanding of the nuclear force. However, despite efforts over the last 50 years, both experimentally and theoretically, there has not yet been a complete quantitative theory to explain the nuclear force.

It is generally considered that the simplest way to study the nuclear force is via the two nucleon interaction when only two nucleons are present. Such a two nucleon interaction can be regarded as the basis of all nuclear phenomena. In principle, the two nucleon force can be used to explain properties of complex nuclei after allowing for the possibility of many body forces, and the possible effect that neighbouring nuclei could have on the two nucleon force. Conversely, the properties of complex nuclei can also yield significant information about the two nucleon interaction.

Experiments have indicated that the nuclear force is: strong and short ranged; partly of an exchange character; has saturation properties; is spin dependent; and very nearly charge independent (Me68). Yukawa (Yu35) explained the nuclear force as the exchange of virtual spinless particles, thus it becomes necessary to consider the pion-nucleon force when attempting an understanding of the nucleon-nucleon force. It has since been postulated that multi-pion and heavier boson exchange contribute to the nucleon-nucleon force, with the heavier bosons accounting for the spin-orbit interaction (No63), and with ω-meson

exchange producing the repulsive core (Mc68).

The nuclear force is usually represented by a potential, the model for which can be either purely experimental, purely theoretical, or a combination of the two. In its most general form, the potential includes central, tensor and spin orbit components (Ok58). Exchange of a few mesons of low mass is often used to describe the long range interaction while the short range interaction, which is further complicated by multi-pion and heavier boson exchange, is described phenomenologically. Such an approach has been used reasonably successfully to describe experimental results (Ha62), but it has , up to the present time, not been possible to deduce uniquely a potential from experimental data.

In order to specify completely the nucleon-nucleon interaction it is necessary to know the elements of the transition matrix (t-matrix) for the interactions between all possible pairs of initial and final two-nucleon states, including those pairs that do not conserve energy and momentum. Nucleon-nucleon elastic scattering experiments (which conserve energy and momentum) yield information about the on-energy-shell elements of the t-matrix. The off-energy-shell elements may be obtained from, for example, deuteron breakup and nucleon-nucleon bremsstrahlung, being processes which do not conserve energy and momentum between the two nucleons. The off-shell behaviour of the t-matrix is almost unknown at present. If it were known it would be especially valuable in the calculation of the binding energy of the triton (and all nuclear matter), and would also be

useful in discriminating between various potential models. It is found that most potential models having similar on-energy-shell t-matrix elements have very different off-energy-shell elements.

4.1. Two Nucleon States

Because of the Pauli exclusion principle, T=1 states are antisymmetric in space-spin co-ordinates and T=Ø states are symmetric, which means that T,S,L must be added, where T, S and L denote isospin, total spin and total orbital angular momentum respectively. For the p-p and n-n systems only T=1 states are allowed, while for the n-p system T=Ø and T=1 are allowed. The first few states are thus

$$T=1 : {}^1S_0 \quad {}^3P_{0,1,2} \quad {}^1D_2 \quad {}^3F_{2,3,4} \quad \ldots$$

$$T=Ø : {}^3S_1 \quad {}^1P_1 \quad {}^3D_{1,2,3} \quad {}^1F_3 \quad \ldots$$

where the spectroscopic notation is ${}^{2S+1}L_J$ with $\underline{J}=\underline{L}+\underline{S}$ (underlining denotes vectors).

When charge independence and parity conservation are assumed only states with the some T, J and parity can mix, therefore mixing occurs only in the triplet (S=1) states and not in the singlet (S=Ø) states. For L<=3 only the states $({}^3S_1+{}^3D_1)$ and $({}^3P_2+{}^3F_2)$ can mix. The strength of the mixing is characterized by the mixing parameter ϵ_J.

4.2. Charge Independence

When considering charge independence it is more convenient to think in terms of two parts, short range and

long range. For close collisions one considers short range independence which concerns the eqivalence, after subtraction of the Coulomb effects, for p-p, n-p and n-n states, especially when l=Ø (Br36). This has been found to be only an approximation, for example in the $^1S_0$ state the n-p interaction is the stronger (Br68a).

Long range charge independence concerns states with high L. The interaction can be described by a one-pion-exchange potential and thus, after electromagnetic effects have been allowed for, the p-p, n-p and n-n states are equal. As yet there is no evidence to the contrary (Br71a).

The only bound state for the two-nucleon system is the ground state of the deuteron (both the diproton and dineutron are unstable), thus most information about the nuclear force comes from nucleon-nucleon scattering experiments. Of the four possible scattering processes, p-p, n-p, p-n and n-n, only the first two are practical because free neutron targets are not possible (the half life of a free neutron is 12 minutes). It is, however, possible to use deuterons as quasi-free neutron targets. There has been good agreement between p-d and n-p inelastic scattering (Ku61, St62), but theoretically such experiments are much more complicated.

Most investigation has been carried out using p-p scattering due to the easy availability of well-defined mono-energetic proton beams with almost any energy and any flux. In contrast to this, neutrons can only be produced by nuclear reactions (see Section 1.1) so that neutron beams

have larger energy spread and low fluxes. To offset these limitations neutron scattering has no Coulomb effects.

Nucleon-nucleon scattering is wholly elastic until the bombarding energy is large enough to create the π rest mass (of approximately 270 MeV Lab). Above this energy inelastic processes involving single pion production occur, for example,

$$n + p \rightarrow d + \pi^{\circ}$$

$$n + p \rightarrow n + n + \pi^{+}$$

$$n + p \rightarrow p + p + \pi^{-}$$

In principle, in order to specify the nucleon-nucleon interaction completely on the energy shell, 256 independent nucleon-nucleon scattering experiments are required at each energy for every angle and each isospin (Wo56) (see Appendix A). This impracticable number can be reduced to 5 (with one not in the same plane) by applying conservation and invariance laws and unitary conditions (Pu57). For identical particles, measurements can be performed in the range $0 \leq \theta \leq \frac{\pi}{2}$, but for the n-p case the range is doubled to $0 \leq \theta \leq \pi$ corresponding to the doubling of the number of states. If inelastic channels are open 9 experiments are required. Examples of the types of experiments that can be performed are those which measure: differential cross sections (Ro70); polarization which yields nuclear spin orbit force information (Mu71) [an effect which is due to the strong interaction between the spin and the orbital motion of the nucleus. This is called the nuclear spin orbit interaction which has a very much larger effect than the corresponding electromagnetic spin orbit interaction],

triple scattering; and spin correlation coefficients (Ma66,Li68).

4.3. Phase Parameter Analysis

In the absence of a complete theory of nuclear forces nucleon-nucleon scattering experiments are described using partial wave analysis. This involves the use of minimization of the experimental data to a smaller set of phase parameters which are elements of the scattering matrix (S-matrix). These parameters, the phase shifts $\delta_{L,J}$ and the mixing parameters ε_J completely characterize the data.

Due to the short range nature of the nuclear force it is expected that only a limited number of partial waves are required to describe scattering at a given energy. Since only a finite set of phase parameters can be determined from experiments in a limited energy range, phase parameter analysis can lead to a number of equivalent solutions for the phase parameters. It has been found that many of these ambiguities can be resolved by determining a solution which varies smoothly with energy.

Individual phase parameter determinations will change as more data are included in the analysis because no experimental data are exact. In fact, differences between phases shifts sets can only be resolved by using more data. Phase shift sets can also be obtained from nuclear potential models, and thus phase shifts provide a meeting ground between experiment and theory.

Due to the sparseness of n-p scattering data it is not

possible to perform an independent analysis to obtain a unique solution as is possible in the p-p case (Ma69). But, by using the T=1 phase parameters from p-p scattering experiments and correcting for short range charge dependence it is possible to analyse n-p data to give T=Ø phase parameters. A unique solution to the n-p data can thus be obtained (Ho71). These T=Ø n-p phase parameters are less accurate and contain any T=1 phase parameter errors. It is therefore important to obtain more accurate n-p scattering data.

The S-D coupling parameter (ε_1) characterizes the tensor forces to which most current models attribute the deuteron binding energy. The failure of such models to predict accurately the triton binding energy or to give sufficient binding in nuclear matter could be better understood if ε_1 and the $^3S_1$ and $^3D_1$ n-p phase parameters were known to high precision in the Ø to 5Ø MeV range. The behaviour of ε_1 in this range has not yet been determined by either experiment or theory. There have been both positive values (Ha62,La62) and negative values (Br58,An66) predicted by potential models and phase parameter analyses. [In order to fit the measured quadrupole moment for the deuteron (Ø.ØØ282 barns) a positive value for ε_1 is required.]

In addition the $\zeta(^1P_1)$ phase shifts are not well known in the 2Ø MeV region (Ro7Ø,Pi72), but it is expected (No63) to approach the one-pion-exchange value. Model predictions (Ho62,La62) bear this out. The differences in the predictions for the T=Ø phase parameter in this energy region are due to the scarcity of the n-p scattering data.

It is therefore hoped that improved data will resolve the problem.

In the 20 MeV region n-p scattering is dominated by S-waves and P-waves, but to be precise, calculations must include D-waves. Principal T=0 phase parameters are $\delta(^3S_1)$, ε_1, $\delta(^3D_1)$, $\delta(^3D_2)$ and $\delta(^1P_1)$. The $\delta(^3S_1)$ and ε_1 can be described using the one-pion-exchange potential (Si67). Major objectives of n-p scattering measurements in this energy region are to determine to what extent the interactions differ from pure S-wave scattering in T=0 states and to determine to what extent the other T=0 phase shifts (singlet P and triplet D) differ from their one-pion-exchange values.

There is, as shown, considerable interest in further measurements of n-p differential cross sections below 30 MeV. Available data are sparse and some have large uncertainties. The present work constitutes an attempt to obtain data to enable verification of the differential cross sections obtained from phase shift predictions by Yale (Se68) and Livermore (Ma69), and if possible to enable a preference to be established for one of the phase shift sets.

5. THEORY OF N-P SCATTERING

The first of the three major approaches used to study the n-p interaction is the phenomenological approach which attempts to determine the interaction by comparison of phase parameter calculations for a given reaction with experimentally determined phase parameters. At first static potentials were assumed, but more recently it has been found necessary to introduce exchange forces, spin orbit forces, and other more complicated L dependent forces.

The second approach is a purely theoretical one in which the interaction is derived from meson field theory. As yet no satisfactory derivation is available. Only the one-pion-exchange potential (OPEP) is known unambiguously. With current field theories it is not possible to treat two and multiple pion exchange unambiguously and so their effect on the nuclear force cannot be reliably calculated. There has also been considerable success using one-boson-exchange (OBE) models (Br63) in explaining n-p data (Si69). A variation of this approach was to use meson-nucleon exchange processes which involves the mathematics of dispersion relations.

The third approach is a compromise between the earlier two methods. In the region of weak interaction field theory is used and in the inner region of strong interaction the phenomenological approach is used. The recent increase in nucleon-nucleon scattering data has enabled the development of more accurate phenomenological and semi-phenomenological potentials based on meson theory. Some of these will be

discussed in the following section.

Experimental data are actually described in terms of phase shifts and coupling parameters (see appendix A) which are determined by a least squares fit. The most extensive phase parameter analyses, those carried out by Yale and Livermore, will also be discussed.

5.1. Potential Models

The most general non-relativistic velocity dependent two nucleon potential on the energy shell was proposed by Okubo and Marshak (Ok58) with the restrictions of

(i) hermicity
(ii) translational invariance
(iii) Galilean invariance
(iv) rotational invariance
(v) space reflection invariance
(vi) time reversal invariance
(vii) charge independence
and (viii) permutation symmetry.

Coulomb forces do not violate condition (vii) because we are only considering purely nuclear forces. The Okubo potential is

$$V=V_0+V_1(\underline{\sigma}_1\cdot\underline{\sigma}_2)+V_2 S_{12}+V_3(\underline{L}\cdot\underline{S})+V_4 L_{12} \tag{5.1}$$

where the spin operators are:

tensor $$S_{12}=[3(\underline{\sigma}_1\cdot\underline{r})(\underline{\sigma}_2\cdot\underline{r})]/\underline{r}^2-\underline{\sigma}_1\cdot\underline{\sigma}_2 \tag{5.2}$$

linear spin orbit $$\underline{L}\cdot\underline{S}=[(\underline{L}_1+\underline{L}_2)(\underline{\sigma}_1+\underline{\sigma}_2)]/2 \tag{5.3}$$

quadratic spin orbit

$$L_{12}=[(\underline{\sigma}_1\cdot\underline{L})(\underline{\sigma}_2\cdot\underline{L})+(\underline{\sigma}_2\cdot\underline{L})(\underline{\sigma}_1\cdot\underline{L})] \tag{5.4}$$

with

$$V_i = V_i(\underline{r}^2, p^2, L^2) \qquad i=0,\ 1,\ 2,\ 3,\ 4,\ldots$$

where

$\underline{r}$ = vector connecting the particles

L = orbital angular momentum

p = momentum operator.

The dependence of V_i on p^2 and L^2 is often neglected (Si69). Also, many authors do not use the Okubo-Marshak form for L_{12} as is given in equation (5.4). For n-p scattering the potential is the sum of the isospin T=1 and T=0 potentials, each of which is of the form (5.1). It is also common to use the concept of the repulsive infinitely hard core (Ja51) with a radius of the order 0.4 to 0.5 fm, in conjunction with a one-pion exchange tail. Thus, when the nucleon-nucleon separation is large (a few pion Compton wavelengths), the interaction can be obtained from the OPEP which can be determined unambiguously (Si69). In these cases the higher partial waves are evaluated from the OPEP pole in the scattering amplitude and the remainder are calculated from experimental data.

The second order one-pion-exchange potential is (Si69)

$$V=[f^2 m_\pi c^2 (\underline{\tau}_1 \cdot \underline{\tau}_2)(\underline{\sigma}_1 \cdot \underline{\sigma}_2 + S_{12}(1+(3/x)+(3/x^2)))e^{-x}]/3x \qquad (5.5)$$

where $x = ur$

$u = m_\pi c/\hbar$

m_π = pion mass

$\underline{\tau}$ = isospin operator

f^2 = renormalized pion-nucleon coupling constant.

The first general form of the phenomenological potential was proposed by Eisenbud and Wigner (Ei41) and had

the form

$$V = V_c + V_T S_{12} + V_{LS} (\underline{L}\cdot\underline{S}) \qquad (5.6)$$

where V_c , V_T and V_{12} denote the central, tensor and linear spin-orbit potentials respectively.

Later the Signell-Marshak (Si57,Si58) and the Brueckner-Gammel-Thaler (Ga57a,Br58) potentials were proposed independently. They both were of the Wigner type with a Yukawa (Yu35) shape outside the hard core. The Signell-Marshak potential was derived from the earlier Gartenhaus (Ga55) potential which was partly based on pion field theory. The Bruechner et al potential was constructed phenomenologically and improved upon the earlier Gammel-Christian-Thaler potential (Ga57) which had no spin-orbit term. Both potential models gave a reasonable explanation of cross sections and polarizations up to quite high energies.

Hamada-Johnston (Ha62) produced a potential containing the OPE tail and a hard core (radius Ø.485 fm in all states). They based their potential on a local, static potential using a phenomenological fit to nucleon-nucleon scattering and bound state data. The potential is

$$V = V_c + V_T S_{12} + V_{LS} (\underline{L}\cdot\underline{S}) + V_{LL} L_{12} \qquad (5.7)$$

where V_{LL} = quadratic spin orbit potential

and $L_{12} = (\underline{\sigma}_1\cdot\underline{\sigma}_2)L^2 - [(\underline{\sigma}_1\cdot\underline{L})(\underline{\sigma}_2\cdot\underline{L}) + (\underline{\sigma}_2\cdot\underline{L})(\underline{\sigma}_1\cdot\underline{L})]/2$

$$= [\delta_{ij} + (\underline{\sigma}_1\cdot\underline{\sigma}_2)]L^2 - (\underline{L}\cdot\underline{S})^2 \qquad (5.8)$$

with the specific forms of V_i (i=C, T, LS, LL) given by (Ha62).

A satisfactory fit to scattering and deuteron data below 315 MeV is obtained using this model. The S-wave

dominated low energy n-p scattering can be described using the effective range expansion (Si47,Be49): viz

$$k \cot\delta = -1/a + r_o k^2/2 - P r_o^3 k^4 + Q r_o^5 k^6 + \ldots \qquad (5.9)$$

where k = wave number of the relative motion at large separation

δ = scattering phase shift

a = n-p scattering length

r = n-p effective range

and P, Q, ... = shape parameters.

Comparing the experimental (En63) and the Hamada-Johnston parameters we have

	H-J (fm)	Expt. (fm)
^1a	-17	-23.714 ± .ØØ4
^1r_o	2.83	2.7Ø4 ± .Ø87
^3r_o	1.72	1.749 ± .ØØ8

where superscripts 1 and 3 denote singlet and triplet states respectively. The n-p scattering length ^1a is significantly lower than the experimental value, however, it is in good agreement with the p-p scattering length (corrected for Coulomb forces) of 17 ± 3 fm, thus demonstrating the well known apparent violation of charge independence of the ^1S_o state. It is possible to reduce ^1a to -23.7 and ^1r_o to 2.73 by choosing a hard core radius of Ø.ØØ28 fm, but such a choice does not give a faithful representation of p-p scattering.

In contrast to the local potentials Tabakin (Ta64) and Mongan (Mo68) developed non-local separable (different parameters for each partial wave) potentials. The Mongan

potential fits the data as well as the local potentials, however the t-matrix elements of both potentials differ greatly from those of the local potentials. The separability of these potentials makes phase shifts particularly easy to compute, but they do not contain a one-pion-exchange contribution since it is not separable or non-local.

Lomon and Feshbach (Fe56, Fe61, Lo67a) have, over many years, developed the Boundary Conditions Model which was first suggested by Breit and Bouricius (Br49). In this model the internuclear distance r is given by the field theory forms involving boson exchange for $r>r_B$ (r_B = boundary radius) and is described by energy independent boundary conditions for the wave function and its logarithmic derivative (applied at $r=r_B$ for each partial wave sensitive to the short range interaction) for $r<=r_B$. The Boundary Condition Model has obtained fits to both p-p and n-p data comparable with the best phenomenological fits below 350 MeV (Lo67).

Bressel, Kerman and Roulen (Br69) and Reid (Re68) have developed soft (finite core) potentials. The former group uses the Hamada-Johnston potential (equations (5.7) and (5.8) modified to allow for the charge dependence of the effective pion mass) for $r>r_c$ (the core radius). For $r<=r_c$ the potential forms are replaced by finite square wells.

The Reid potential has two versions, one with a hard core, and the other with a soft core of the Yukawa type. The difference between this and other potentials is that it is parameterized separately for each set of J, L and S

quantum numbers and cannot be separated into central tensor, linear spin orbit and quadratic spin orbit terms like other potentials.

Another soft core potential was developed by a Czech group (U17Ø) where the soft core applied to the triplet state which was computed as a superposition of Yukawa potentials to fit the experimental phase parameters below 31Ø MeV.

Yale have developed various potentials in order to give a better fit to their phase parameter analysis. Their original version (La62) was similar to the Hamada-Johnston potential in that it had a hard core (radius Ø.51 fm) and approached a OPEP at large distances. It was developed in an attempt to produce a potential that would give as good a representation of the experimental data as did phase parameter fitting. They attempted to approximate their phase parameters obtained in their YLAM and YLAN3M fits (Br6Øc, Ha61) by using a velocity dependent potential. It was, in fact, a modification of the earlier potential developed by Bryan (Br6Øb). The form was

$$V = V_{OPEP} + V_T S_{12} + V_{LS}\, \underline{L}\cdot\underline{S} + V_{LL}\left[(\underline{L}\cdot\underline{S})^2 + \underline{L}\cdot\underline{S} - \underline{L}^2\right] \qquad (5.1Ø)$$

where all potentials except V_{OPEP} have forms like

$$V = \sum_n a_n e^{-2x}/x^n \qquad (5.11)$$

where x = ur

r = internucleon distance

$u = m_\pi c/\hbar$

m_π = pion mass

and a_n = adjustable parameters. Values of a_n and the hard core radius were varied to provide a fit to YLAM and YLAN3M.

The most recent versions of the Yale potential (Br68a) were obtained by fitting the later Yale phenomenological phase parameter sets of the Y-IV series (Br67, Br68, Se68). One of the new potentials is a modified version of the Reid soft core potential (Re68) and is designated YRM. It has the following form

$$V(\text{soft core}) = V_{SC} = V_{OPEP} + [A_3 e^{-3x} + A_4 e^{-4x} + A_4 e^{-6x} + a_7 e^{-7x}]/x \qquad (5.12)$$

The other potential follows the Hamada-Johnston potential and is referred to as $Y_{H\text{-}J}$ and has the form

$$V(\text{hard core}) = V_{HC} = kg^2[1+A(e^{-x}/x)+B(e^{-x}/x)]\ (e^{-x}/x)$$

$$\text{for } (r>r_c) \qquad (5.13a)$$

and $$V_{HC} = +\infty \text{ for } (r<=r_c) \qquad (5.13b)$$

where k = a factor independent of r

r_c = hard core radius

$g^2 = (2M/m_\pi)^2 f^2$

f^2 = renormalized pion-nucleon coupling constant

and M = nucleon mass.

Although several other phenomenological and semi-phenomenological models of the two nucleon system have been developed over the years, those represented here are those which have been most used (Si69). It has become increasingly clear that at present no such thing as a realistic two nucleon potential exists or can be obtained with the presently available experimental data (Fi71). Scattering amplitudes alone do not determine the potential uniquely, it is necessary to have a knowledge of the off-energy-shell properties of the nucleon-nucleon interaction in order to discriminate between various

potential models (So63). Such information can be obtained, for example, by experiments on: nucleon-nucleon bremsstrahlung ($n+p \longrightarrow n+p+\gamma$ or $p+p \longrightarrow p+p+\gamma$); three body breakup (D+n-->n+n+p); photodisintegration of the deuteron ($D+\gamma \longrightarrow n+p$); n-p capture; and electron-deuteron elastic scattering.

Predictions for the n-p differential cross sections at 8 MeV based on the Yale and LRL phase shifts are shown in Figure (8.11). A comparison of some of the potential models mentioned and some phase parameter representations of nucleon-nucleon scattering data is given in Table (5.1). Column 5 gives values for the ratio of χ^2 to its statistically expected value due to experimental uncertainties which were evaluated for a representative proton-proton scattering data set in the energy range 8 to 320 MeV (No67a, Si69) where χ^2 is given by (Si69)

$$\chi^2 = \sum_n ((P_n - D_n)/\epsilon_n)^2 \qquad (5.14)$$

where P_n = model predicted value

D_n = experimental data

and ϵ_n = experimental uncertainties.

It can be seen that the best fitting potential tested with this J=1 data set was that of Bressel, Kerman and Rouben (Br69).

Table (5.1)
Ratio for potential model and phase parameter representation predictions.

Model	Ref.	Type	Core Radius (fm)	Ratio
Brueckner-Gammel-Thaler	Br58	Hard Core	Ø.4Ø	1Ø4
Lomon-Feshbach	Lo67a	Bound.Cond.	Ø.75	2.71
Bressel-Kerman-Rouben	Br69	Soft Core	Ø.7Ø	1.12
Reid	Re68	Hard Core	Ø.42	2.7Ø
Hamada-Johnston	Ha62	Hard Core	Ø.48	2.98
Yale	La62	Hard Core	Ø.51	3.77
Tabakin	Ta64	Nonlocal		27
Scotti-Wong	Sc65	OBE		2.54
Bryan-Scott	Br6Ø	OBE		3.93
YLAM	Br6Øc	Phase Param.		2.75
YRB1(K)	Br67a	Phase Param.		1.92
LRL-IV	Ar66	Phase Param.		1.41

5.2. Phase Parameter Analysis

Groups which have performed phase parameter analysis include Dubna (Ka67,Bi68), Harwell (Ba64,Pe67), Livermore (LRL - Lawrence Radiation Laboratory) (Ma69), Los Alamos - Michigan State (He69, Sh7Ø), Stanford (No64,No67) and Yale-Buffalo (Se68). Of these LRL and Yale are the only two who carried out large scale energy dependent analysis on the nucleon-nucleon scattering data and so the following discussion will be confined to these groups.

The phenomenological analysis undertaken by LRL and Yale used all the available data in the elastic region up to 750 and 350 MeV respectively. As well as the energy dependent analysis LRL fitted data at discrete energies and found the fits to be in good agreement.

Slightly different approaches were made by the two groups: the LRL approach was based on a theoretical standpoint with the resultant phase shifts reflecting in part the theoretical form used for each particular phase shift determination whereas the Yale approach was to keep theory to a minimum so that the resulting phase shifts were a representation of the experimental data and not of a specific theoretical model. Yale did however, calculate the high phase shifts from the OPEP. In practice, both approaches are similar in that both are flexible and both have some theoretical justification.

The ten articles in which most of the LRL phase analysis are represented are (Ma65)[I], (Ma65)[II], (No65)[III], (Ar66)[IV], (Ar67)[V], (Wr67)[VI], (Ma86)[VII], (Ma68a)[VIII], (Ma68b)[IX] and (Ma69)[X] where sets VII to X contain later data that were not used in sets I to VI. The respective solutions are designated LRL-I to LRL-X. The general form of the phase shifts used (Ma68) was

$$\delta_L^{(S,J)}(E) = \delta_{L_0}^{(S,J)}(E) + \sum_{i=1}^{n} \alpha_i^{(S,J)} F_{L_i}(e) \qquad (5.15)$$

where L = orbital angular momentum

J = total momentum

S = total spin

E = laboratory kinetic energy

and α_i = free parameters.

Using the $^1S_0$ phases δ_{00} taken from effective range theory (No64) and δ_{L0} (L=Ø) taken from the OPEP (Cz59) we have

$$F_{Li}(x_0) = (x_0-1)\int_0^1 Q_L\left(\frac{x_0-x}{1-x}\right)\frac{x^{i-\frac{1}{2}}}{(1-x)}\,dx \qquad (5.16)$$

where $x = 1 + 4u^2/ME$

$u = m_\pi c/h$

m_π = pion mass

M = nucleon mass

and Q_L = Legendre function of the second kind.

It was found that the initial phase shift analysis (unconstrained) yielded a negative value for the S-D coupling parameter, ε_1, at low energies. However, ε_1 is known to be positive from the deuteron quadrupole moment, so LRL constrained to positive values at low energies and produced a set of constrained phase shifts. It is this constrained set which is preferred (Ho71).

The Yale fitting procedure (Br60c,Br67a) was to change any one of the phase parameters $\delta^{(n)}(E)$ using values of $\delta^{(n-1)}(E)$ from the previous n searches, such that

$$\delta^{(n)}(E) = \delta^{(n-1)}(E) + \sum_i a_i^{(n)} f_i^{(n)}(E) \qquad (5.17)$$

where $f_i(n)$ = a set of conveniently chosen functions which in general vary at different stages of the search

and $a_i(n)$ = free parameters.

Yale's earlier versions of phase parameter fits such as YLAN4M and YRB1(Ko) (Br65a,Se66), YLAN3M' (Hu62), and YLANØ,

YLAN1, YLAN2, YLAN2m and YLAM (Hu61,Hu62,Hu62a) have been superseded by Y-IV (Br67,Br68,Se68,Br69b,Br71a).

In order to resolve the differences between the two phase shift set predictions, and indeed to verify the general trend implied by both sets, it is necessary to obtain more accurate data.

6. MONTE CARLO PROGRAM

The main reasons for writing this Monte Carlo program were (a) to enable multiple scattering estimates to be made for the passage of neutrons through a scintillator and (b) to investigate the sensitivity of pulse height distributions obtained from a scintillator subjected to a neutron flux to the predicted n-p differential cross sections.

Neither problem can be solved analytically. However, if the relative probabilities for the possible processes are known, the Monte Carlo method provides a meams of simulating the actual measurement by tracing out and recording the histories of a large number of individual neutrons.

In general, the Monte Carlo method involves a process of random sampling. In Monte Carlo computations, samples are drawn from some "parent population" through sampling procedures governed by specified probability laws. One is then led to inferences about the parent population through analysis of the statistical data collected from the samples.

When one wants to study a complicated system with very many interacting components, the behaviour of which is governed by known probability laws, it is possible, in principle at least, to incorporate these same laws into the Monte Carlo computation so that processes occurring during the course of the computation will be abstract analogues of processes in the real world. The Monte Carlo process is thus an analogue or direct simulation process.

6.1. Random Numbers

In order to perform a Monte Carlo calculation one requires a large number of "high quality" random numbers. Throughout the rest of this text, unless otherwise specified, a random number (r) is understood to be a particular value of a continuous random variable uniformly distributed on the interval zero to one (including zero but not one). One uses the qualification "high quality" to emphasize concern about the randomness of a random number sequence. Random numbers for Monte Carlo calculations have, in the past, been produced by: (a) extracting samples from tables ; (b) monitoring the output of some physical process (for example, resistor noise); and (c) calculation using a mathematical algorithm. Of these three, the most commonly used present day method is the third. It is obvious that random numbers produced in this fashion have been selected using a deterministic method and are not truely random. It is for this reason that they are often referred to as "pseudo-random" numbers. The important point to remember about these numbers is that they are uniformly distributed and are to a large extent uncorrelated. They, therefore appear to be, for all normal applications, random numbers.

The algorithm used in the present Monte Carlo code is a variation on the multiplicative congruential method that was proposed by Lehmer (Le49) which takes the form

$$x_i = a\, x_{i-1} \pmod{m} \qquad (6.1)$$

where x_0, a and m are positive integers (m large). [The

notation x=y(mod m) is read "x is congruent to y modulo m" and means x is the remainder of y upon division by m, Ø=<x<m.] The pseudo random numbers themselves are formed by the sequence (x_i/m).

The other important consideration when using an algorithm to produce pseudo random numbers is how many distinct numbers are produced before the sequence repeats itself. For the particular algorithm used

$$x(n) = x(n-1) + x(n-127) \bmod (2^{\omega}) \qquad (6.2)$$

the period length is $2^{127} - 1 > 10^{38}$ which is more than sufficient for our needs.

With a suitable supply of pseudo random numbers available, the problem becomes one of obtaining random samples from general probability distributions. The two most commonly used sampling methods are the direct (or inversion) method and the rejection method. Both used in the present code and so will be discussed briefly.

Consider firstly the direct method. If x is a random variable with a density function f(x), a=<x=<b, then we want to draw samples from the density function to construct a sequence of numbers t so that

$$P(a<t>b) = \int_a^b f(x)\,dx \qquad (6.3)$$

The cumulative probability function F(x) for X is then

$$F(x) = P(X=<x) = \int_A^x f(t)\,dt \qquad (6.4)$$

Now F(x) is such that Ø=< F(x) =< 1, which suggests that by generating random numbers r we can produce a random sample x

from the distribution F(x) by inversion. Figure (6.1) illustrates the general idea of this method. An example of the use of this method is found in section (6.4.2) where an exponential probability function was inverted to yield the neutron collision distance,

$$l = (-\ln(1-r))/\sigma_T \qquad (6.5)$$

Despite the general usefulness of the inversion method for sampling discrete or continuous functions, it can be computationaly awkward for certain continuous distributions. In these cases the rejection method has found favour. As the name implies, not all generated samples are used, some are rejected. However, despite this waste, rejection methods often reduce the average computational time per sample used because they can employ simpler formulae.

To understand this method, consider the probability density function f(x) such that f(x)=Ø for x<a , x>b and f(x)=< m for a=<x=<b, m being the least upper limit for f(x). We can then define g(x) as

$$g(x) = f(x)/m \qquad (6.6)$$

so that Ø=< g(x) =< 1 for a =< x =< b. Now by generating two independent random numbers r_1 and r_2 we can interpret $(a+r_1(b-a) , r_2)$ as a point in the rectangle with base (b-a) and height 1, as shown in Figure (6.2). If this point is above curve g(x) it is rejected. If it falls on or below g(x) it is utilized to generate a desired sample, that is, $t_i = a+r_i (b-a)$. This procedure is equivalent to random sampling from f(x). The rejection method of sampling is used in the present code to sample from the n-p differential cross sections as descibed in section (6.4.4b).

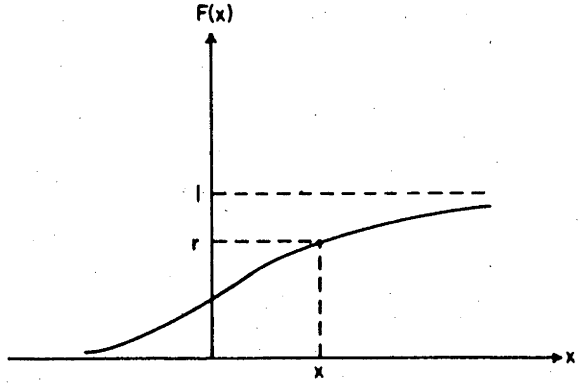

Figure (6.1)
The direct sampling method. By generating a random number r, a random sample x is obtained from the distribution F(x).

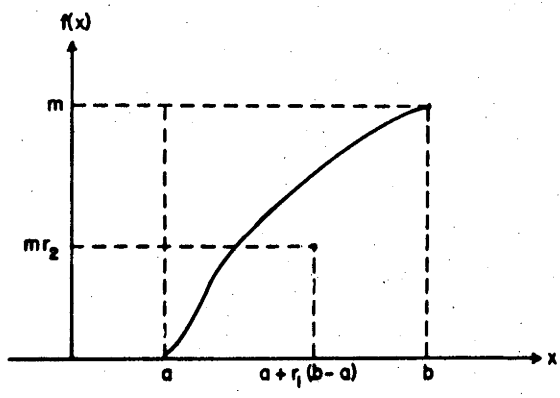

Figure (6.2)
The rejection sampling method. By generating two independent random numbers r_1 and r_2 , a point given by $\{a+r_1(b-a)\ ,\ mr_2\}$ is defined. If this point is on or below f(x) the desired sample is given by $t_i = a+r_i(b-a)$. If the point is above f(x), it is rejected and a new pair of random numbers is generated.

Another important concept in Monte Carlo methods is that of variance reduction. As the results of a Monte Carlo program are statistical in nature, one way of reducing the uncertainty in a result is to base it upon more observations. This is not always a practical solution due to the large increase in computational time required. It is therefore quite often profitable to change or, at least, distort the original problem in such a way as to reduce the variance and then at the end of the calculation to correct for the distortion. Such techniques are described by Spanier and Gelbard (Sp69). An example of such a technique is the requirement that every neutron entering a scintillator undergoes a collision (forced first collision) as described on section (6.4.2b). In this case the absolute scintillator efficiency is found by dividing the Monte Carlo result by a weighting factor.

The strategy involved in writing such a Monte Carlo program is best illustrated by the flow chart shown in Figure (6.3). Initiation of the program requires the input of the appropriate cross section data and the experimental geometry. A neutron, produced with the appropriate energy and direction, is forced to have a collision, the type of collision being governed by the cross section data. The scattering angle and the energy deposited in the scintillator are evaluted. The deposited energy is converted into a light output by means of response functions with corrections for light attenuation in the scintillator

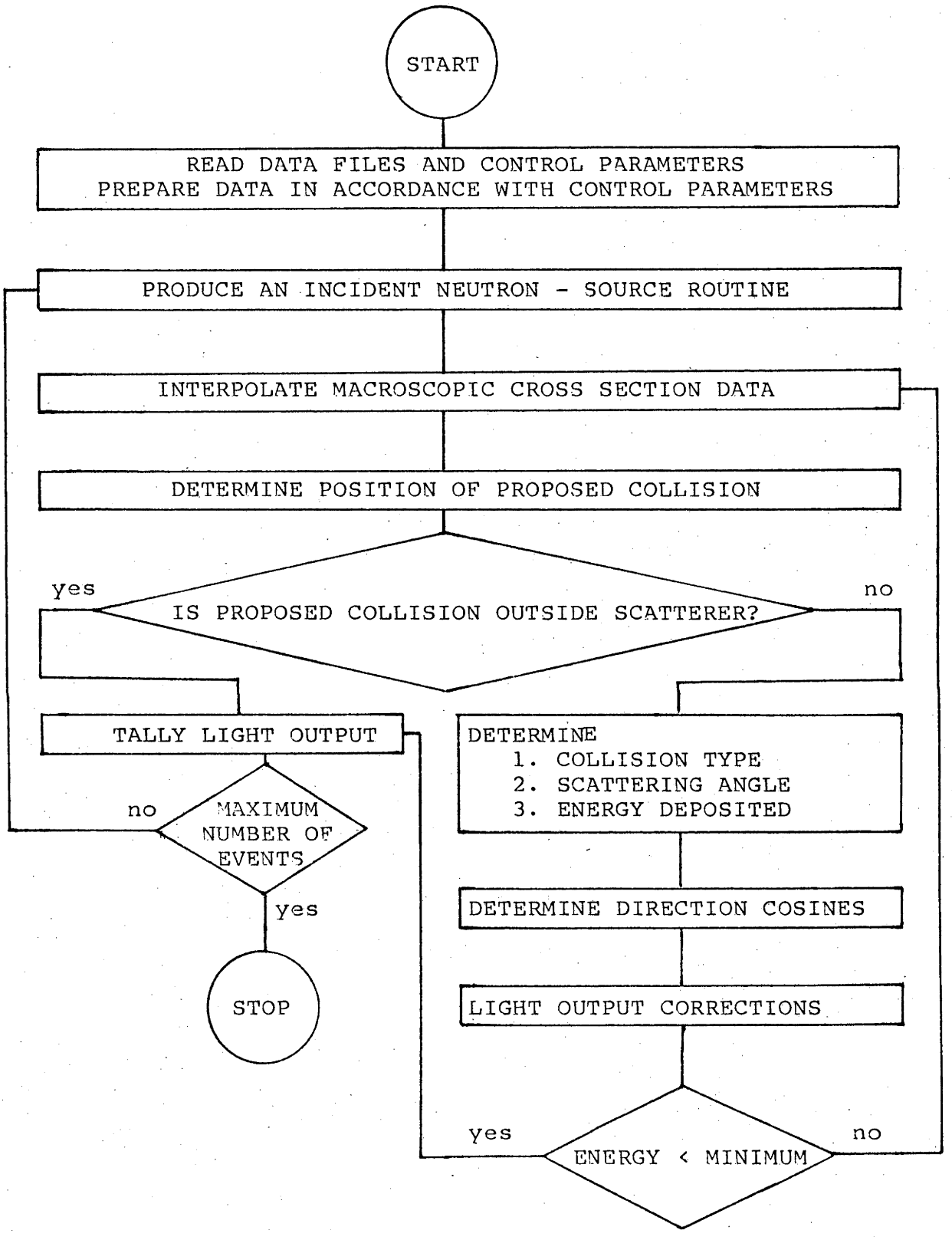

Figure (6.3)
Monte Carlo code master flow chart.

and for recoiling protons that leave the scintillator before loosing all of their energy.

6.2. Data Required

In order to reproduce accurately the results of an experiment, it is necessary to provide all the parameters which define the experiment. These include the dimensions, orientation and position of the scintillator and physical constants for the scintillator such as its density, ratio of the number of hydrogen atoms to the number of carbon atoms and its light attenuation length. These physical constants are used in conjuction with microscopic total scattering cross sections for n-p elastic, $n\text{-}C^{12}$ elastic and $n\text{-}C^{12}$ inelastic scattering to produce macroscopic cross section tables that are interpolated to yield the required cross sections. (The subroutine CROSS performs this operation). The microscopic data tables and the $n\text{-}C^{12}$ elastic differential cross sections data were supplied by E. Clayton.

Proton range data, for energetic protons in the scintillator are used for calculating the scintillator wall effects, that is, the reduction of light output due to an energetic proton leaving the scintillator before depositing all of its energy.

Scintillator response functions and neutron beam profile parameters are also required. These are measured for the particular experimental set up required.

6.3. Source Routine

6.3.1. Introduction

The purpose of the source routine is to produce a neutron flux which resembles as closely as possible the real neutron beam as produced by the $D(d,n)^3He$ reaction and particle identifaction system as described in section (2.1). It must produce the direction cosines, the total scattering angle with respect to the deuteron beam direction, thus determining the neutron energy, and the co-ordinates of the point where the neutron enters the scintillator. The direction of the neutron is controlled by two Gaussian distributions in order to simulate the real beam profile. The standard deviations of the Gaussians were determined experimentally as described in the section entitled Beam Profile.

A random number generator (RGAUS2) produces random numbers according to the Gaussian distribution

$$P_u(x,\sigma) = \exp(-(x/\sigma)^2/2) \qquad x_{min} =< x =< x_{max} \quad (6.7)$$

The limits x_{min} and x_{max} were placed upon x to avoid wasted computational time calculating parameters for experimentally unrealistic events, for example, when $x=10\sigma$. These random numbers provide the two scattering angles ψ and ξ as defined in Figure (3.1). It also shows the orientation and position of the cartesian co-ordinate system used by the program.

6.3.2. Direction Cosines and Total Scattering

The direction cosines u,v,w for a neutron whose direction is defined by the two angles ψ and ξ , where α, β and γ are the angles between the x, y and z axis and the neutron direction respectively, are

$$u = \cos \alpha = \sin\psi / M$$
$$v = \cos \beta = \sin\xi / M \qquad (6.8)$$
$$w = \cos \gamma = \cos\xi \cos\psi / M$$

where $M = (\sin^2 \psi + \sin^2 \xi + \cos^2 \psi \cos^2 \xi)$

The total scattering angle ω, the angle between the deuteron beam direction and the neutrons path is given by

$$\omega = \arccos(\cos(\phi + \xi) \cos(\psi)) \qquad (6.9)$$

where ϕ is the angle between the deuteron beam direction and the z-axis.

6.3.3. Neutron Incident on the Flat Face

(Subroutine SORCE1)

The equations of the line from P_1 (the position of the $D(d,n)^3He$ reaction) and P_2 (the point of intersection of the neutrons path with a sphere of radius D) are

$$x = (z+D) \sin\psi / (\cos\xi \cos\psi)$$
$$\text{and} \quad y = (z+D) \sin\xi / (\cos\xi \cos\psi) \qquad (6.10)$$

Solving these equations with the equation of the surface of the cylinder yields the co-ordinates of the point where the neutron enters the cylinder which is given by

$$x = D \tan\psi / \cos\xi$$
$$y = D \tan\xi / \cos\psi \qquad (6.11)$$

$z = \emptyset$

6.3.4. Neutron Incident on the Curved Surface

(Subroutine SORCE2)

In this case the cylindrical axis of the cylinder is parallel to the y axis. It is convenient to move the origin of the co-ordinate system to the centre of the cylinder. The co-ordinates of the point P_1 thus become $(\emptyset,\emptyset,-(D+R))$ where R is the radius of the cylinder. The equations of the line $\overline{P_1 P_2}$ thus become

$$x = (z+D+R) \tan\psi / \cos\xi \qquad (6.12)$$

$$y = (z+D+R) \tan\xi / \cos\psi \qquad (6.13)$$

Solving these with the equation of the cylindrical surface,

$$R^2 = x^2 + z^2$$

yields,

$$z = (-B - \sqrt{B^2 - 4AC}) / 2A \qquad (6.14)$$

where $A = \sin^2\psi + \cos^2\xi \cos\psi$

$B = 2(D+R) \sin^2\psi$

$C = (D+R)^2 \sin^2\psi - R^2\cos^2\xi \cos^2\psi$

Substituting this z co-ordinate into equations (1) and (2) gives the x and y co-ordinates for the point of the neutrons entry into the scintillator.

6.3.5. Neutron Energy

After evaluation of the direction cosines, scintillator entrance co-ordinates and total scattering angle ω, by

either SORCE1 or SORCE2 (depending on the desired scintillator orientation), the energy of the neutron is calculated using a relativistic kinematic formula. The subroutine RKINI, which is used once at the start of the main program evaluates the relativistic momentum, the total energy (E_T) and a constant A for the $D(d,n)^3He$ reaction for the appropriate incident deuteron energy. The constant A is given by

$$A = 2M_dT_d + 4M_dM_n + 2Q(2M_d - M_n) - Q$$

where M_d = the rest mass of the deuteron

M_n = the rest mass of the neutron

T_d = incident deuteron energy

Q = the Q value for the $D(d,n)^3He$ reaction.

The function subprogram RKINF then evaluates the neutron energy for the appropriate scattering angle according to the formula

$$T_n = (E_TA + P\cos\omega\sqrt{A^2 - 4M^2B})/2B - M_n$$

where $B = E_T^2 - P^2\cos^2\omega$

6.4. Collision Routine

6.4.1. Cross Sections

In order to determine the position of a collision, and indeed the type of collision, it is necessary to evaluate the scattering cross sections for the particular neutron energy being considered. Values for n-p elastic scattering (σ_p =SHE), n-C elastic scattering ($\sigma_{C_{el}}$ =SCE) and n-C

inelastic scattering (σ_{Cinel}=SCI) are interpolated from the macroscopic scattering cross section data tables prepared by the subroutine CROSS. From these values the total scattering cross section (σ_T=SSCAT=σ_p +σ_{Cel} +σ_{Cinel}) is known.

6.4.2. Distance to a Collision

(a) Normal Collision

If σ_T is the total macroscopic collision cross section for a uniform infinite medium then the number of particles left in a beam after travelling a distance ℓ is $n=n_o\exp(-\ell\sigma_T)$ where n_o is the number of particles in the beam at $\ell=0$. The probability distribution function for a first collision at distance =<l is thus given by

$$P(\ell) = \int_0^l \exp(-\sigma_T l)\sigma_T dl = 1 - \exp(-N\sigma_T l) \qquad (6.15)$$

The Monte Carlo determination of the distance ℓ from an arbitary point to a first collision is thus performed by

$$\ell = (-\ln(1-r)) / \sigma_T \qquad (6.16)$$

where $r = P(\ell) = 1 - \exp(-N\sigma_T)$

and r is a random number evenly distributed between zero and 1. However, 1-r is equi-distributed between zero and thus giving

$$\ell = (-\ln(r)) / \sigma_T \qquad (6.17)$$

If by travelling a distance ℓ the neutron is now outside the scintillator then it, the neutron, has exited from the scintillator without a collision.

(b) Forced First Collision

If the above approach were to be applied to every neutron entering the scintillator then a large proportion would pass through the scintillator without a single collision and thus a large amount of computational time would be wasted. To avoid this, each neutron is "forced" to have at least one collision inside the scintillator. In this case, the distance from the point of entry to the first collision is given by

$$\ell = (-\ln(1-rW)) \; / \; \sigma_T \qquad (6.18)$$

where $W = 1 - \exp(D\sigma_T)$ is a weighting factor. D is the distance to the boundary of the scintillator in the direction of the neutron's flight. It is thus necessary to evaluate a mean weighting factor in order to calculate the scintillator efficiency. The distance to the boundary is evaluated by the function subprogram DISTB for the case of the beam incident on the flat surface of the scintillator and by DISTC for the case of the beam incident on the curved surface.

6.4.3. Type of Collision

Once the distance to the next collision has been chosen then the position of the proposed collision can be determined. If this position is within the scintillator it is then necessary to determine whether it is a hydrogen collision, a carbon elastic collision or a carbon inelastic collision. This is determined by the relative macroscopic

scattering cross-sections. A random number $R=r\sigma_T$ is chosen where $\emptyset=<r<1$. Then if

$R < \sigma_{C_{inel}}$ it is a carbon inelastic collision

$R-\sigma_{C_{inel}} < \sigma_{C_{el}}$ it is a carbon elastic collision

and $r-\sigma_{C_{inel}} >= \sigma_{C_{el}}$ it is a hydrogen collision.

6.4.4. Neutron Scattering

For the general case of neutron elastic scattering the formulae of prime importance in a Monte Carlo calculation are

$$E' = E (S + Tu) \qquad (6.19)$$

and $$a = (1 + Au) / (1 + A^2 + 2Au)^{\frac{1}{2}} \qquad (6.2\emptyset)$$

where A = m(target) / m(neutron)

$S = (1 + R) / 2$

$T = (1 - R) / 2$

$R = (A - 1)^2 / (A + 1)^2$

E = neutron energy before scattering

E' = neutron energy after scattering

$u = \cos \omega'$

ω' = neutron scattering angle in c.m. system

$a = \cos \omega$

ω = neutron scattering angle in the laboratory system.

For the general case of scattering from hydrogen we have $A \approx 1$, which implies R = Ø and S = T = Ø.5 . Thus equations (6.19) and (6.2Ø) become

$$E' = E (1 + u) / 2 = Ea^2 \qquad (6.21)$$

$$a = ((1 + u) / 2)^{\frac{1}{2}} \qquad (6.22)$$

The problem is now simply one of choosing a value for u.

(a) Isotropic Scattering from Hydrogen

For isotropic scattering $d\sigma / d\Omega$ = a constant, so that $\cos\omega'$ is uniformly distributed between -1 and +1 so that

$$u = 2r - 1 \tag{6.23}$$

and $$a = \sqrt{r} \tag{6.24}$$

(b) Using LRL or Yale Differential Cross Sections

For either case the procedure is the same. Data sets have been prepared containing the values of the differential cross sections for 21 values of cos at 25 energies from Ø.1 to 3Ø MeV. Data file DIFFDATA. contains the data for both sets, the main program reading in the required set.

The appropriate data set is interpolated to yield a differential cross section for the required energy and this distribution is used to weight the selection of the scattering cosine, $\cos\omega$.

(c) Carbon Elastic Scattering

For carbon elastic scattering tables of cumulative probability for scattering between zero and a c.m. angle ,

$$Q(u,I) = \{ \int_{1}^{u} [d\sigma(I)/d\Omega] \, du \} \; / \; \{ \int_{-1}^{1} [d\sigma(I)/d\Omega] \, du \} \tag{6.25}$$

where $u = \cos\omega'$ are tabulated in Ø.1 steps in u for 9 energy groups (identified by I). The value of u is then randomly selected using values interpolated from the data tables to bias the result.

(d) Carbon Inelastic Scattering

For the case of inelastic scattering the equations (6.19) and (6.2Ø) become

$$E' = E \left(S - (A/(1+a))^2 \left(\mathcal{E}_c/E \right) + TuB \right) \quad (6.26)$$

and $$a = (1 + AuB) / (1 + A^2(1-(\mathcal{E}_c/E)) + 2AuB) \quad (6.27)$$

where $B = \sqrt{1 - (\mathcal{E}_c/E)}$

$\mathcal{E}_c = \mathcal{E}$ (m(target) +m(neutron)) / m(target

$\mathcal{E}$ = excitation energy.

The first excited state of carbon is $\mathcal{E}$ =4.43 MeV thus giving $\mathcal{E}_c$ = 4.8Ø17 MeV.

The values for the scattering cosine u were selected according to an isotropic distribution. However, the experimentally measured differential cross sections for carbon inelastic scattering are not isotropic. They are relatively close to isotropic, but the features they do have vary dramatically for a small change in energy. This makes the methods used for interpolating differential cross section data sets for a few energies impractical, and it is considered that the isotropic distribution provides a better approximation of the physical situation.

6.4.5. Direction Cosines after Scattering

The scattering cosine a=cos ψ ,which is evaluated using the formulae given in section 6.4.4, defines the cone to which the scattered neutron is confined. It is now necessary to choose a particular path along this conical

surface by choosing a value for δ (see Figure (6.4)).

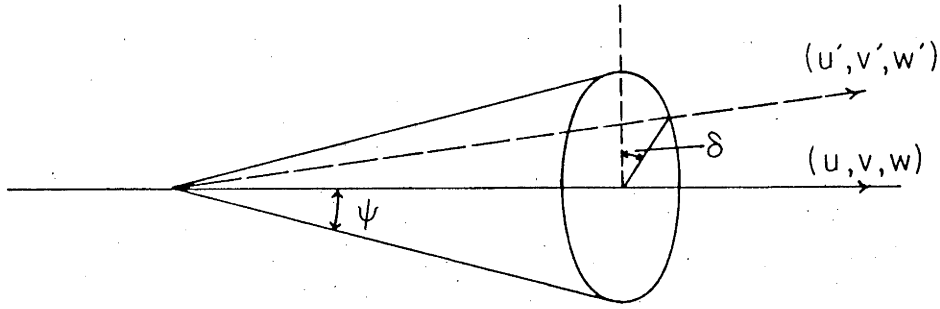

Figure (6.4)
The angles specifying a position on the conical section are defined as in this figure.

All values $\emptyset=<\delta>2\pi$ are equally probable and so δ is chosen by $\delta=2\pi r$ (r is a random number such that $\emptyset=<r>1$) in which case the direction cosines after scattering (u',v',w') in terms of the direction cosines before scattering (u,v,w) are given by

$$u' = (bcwu - bdv) / (1-w)^{\frac{1}{2}} + au$$
$$v' = (bcwv - bdu) / (1-w)^{\frac{1}{2}} + av \qquad (6.28)$$
$$w' = -bc\,(1-w)^{\frac{1}{2}} + aw$$

where $a = \cos\psi$ $\quad b = \sin\psi$

$c = \cos\delta$ $\quad d = \sin\delta$

For the case where |w| is close to unity these expressions are poor computationally and are in fact indeterminate at |w|=1. In such cases it is better to use

$$u'=bc$$
$$v'=bd \qquad (6.29)$$
$$w'=aw$$

6.5. Pulse Height Output Routine

In order that the Monte Carlo program can be used to determine a preference for a particular phase shift set it must be able to produce pulse height spectra. In order to do this the response functions of the scintillators must be known. These are determined from measurements taken concurrently with the actual pulse height spectra that the Monte Carlo is trying to reproduce. A detailed description of the response functions and how they are obtained is given in the section entitled Response Functions.

The response functions are used in the function subprogram SCINA to evaluate the equivalent gamma ray energy for a given proton or carbon recoil. The appropriately scaled gamma ray responses are used as the pulse height for the particular event. To this pulse height it is then possible to perform corrections for edge effects and light attenuation within the scintillator.

6.5.1. Edge Effects

The edge effect correction is necessitated by the fact that not all recoiling protons lose all of their energy before exiting from the scintillator. In order to perform such a correction it is necessary to know the range of protons in NE102. Craun and Smith (Cr70) have tabulated values of dE/dx for protons in NE102. These values were integrated to provide range (cm) versus energy (MeV) data, according to $R(E) = \int_0^E 1/(dE/dx)\, dE$. Table (6.1) shows the

values for range versus energy. These data were fitted with two functions, one giving the proton range as a function of energy, the other giving proton energy as a function of range. They are

$$R_p(E) = a_1E+a_2E^2+a_3E^3+a_4E^4+a_5[(E-a_6)^2+a_7]^{-1} \quad (6.30)$$

where $a_1 = 1.3528\text{x}10$ $a_2 = 1.3700\text{x}10$

$a_3 = -2.0590\text{x}10$ $a_4 = 3.2105\text{x}10$

$a_5 = -3.1218\text{x}10$ $a_6 = 0.7945$

$a_7 = 0.1714$

and $$E_p(R) = 38.630\ R^{\frac{1}{2}} - 10.650\ R^{\frac{1}{3}} + 2.2551\ R^{\frac{1}{4}} \quad (6.31)$$

[The Lorentzian term on the end of equation (6.30) was necessary to accommodate a shallow dip that the polynomial alone could not adequately fit. The effect of this dip on the inverse function was found to be much less significant thus not requiring such a term.] From the point of computational efficiency and accuracy the use of these two functions was better than interpolation of the data table.

Using equation (6.30) the range of 8 MeV protons in Ne102 is .0896 cm, thus for the smallest scintillator used [diameter 3.80 cm and depth 1.27 cm] scintillations occurring in approximately 22% of the volume may require edge effect correction. In order to perform this correction the direction of the recoiling proton must be known. Given that M_1, E_1 and M_2, E_2 are the masses and energies of the scattered neutron and recoiling proton respectively, and that ψ is the neutron scattering angle in the laboratory system, the recoil angle ξ is given by $\sin\xi = (M_1E_1/M_2E_2)^{\frac{1}{2}}\sin\psi$. Using this value of ξ (which is evaluated by the function subprogram RECOIL) and the

TABLE (6.1)

Craun and Smith (Cr70) give dE/dx versus E data for protons in NE102 which have been integrated to give the proton range versus energy values shown here. This has been fitted with two functions yielding range as a function of energy {R(E)} and energy as a function of range {E(R)} (see text), values for which are shown in columns 3 and 4.

ENERGY (MEV)	RANGE (CM)	FITTED RANGE R(E)	FITTED ENERGY E(R)
.00	.0000	.0000	.00
.31	.0004	.0005	.33
.61	.0012	.0012	.62
.92	.0022	.0022	.92
1.22	.0036	.0036	1.23
1.53	.0051	.0052	1.53
1.84	.0070	.0070	1.84
2.14	.0090	.0090	2.14
2.45	.0113	.0112	2.44
2.76	.0137	.0137	2.75
3.06	.0164	.0164	3.05
3.37	.0194	.0193	3.35
3.67	.0225	.0225	3.66
3.98	.0259	.0259	3.96
4.29	.0294	.0294	4.27
4.59	.0333	.0332	4.58
4.90	.0373	.0373	4.89
5.20	.0414	.0415	5.19
5.51	.0458	.0459	5.50
5.82	.0505	.0505	5.81
6.12	.0553	.0554	6.12
6.43	.0604	.0604	6.43
6.73	.0656	.0656	6.74
7.04	.0711	.0710	7.05
7.35	.0767	.0767	7.35
7.65	.0825	.0825	7.66
7.96	.0885	.0885	7.97
8.27	.0946	.0946	8.28
8.57	.1010	.1010	8.58
8.88	.1076	.1076	8.89
9.18	.1143	.1143	9.20
9.49	.1213	.1212	9.51
9.80	.1284	.1283	9.81
10.10	.1356	.1356	10.12
10.41	.1431	.1430	10.42
10.71	.1507	.1507	10.73
11.02	.1585	.1585	11.03
11.33	.1664	.1665	11.34
11.63	.1746	.1746	11.64
11.94	.1829	.1829	11.95
12.25	.1914	.1914	12.25
12.55	.2000	.2000	12.55
12.86	.2088	.2089	12.86
13.16	.2178	.2179	13.16

Table (6.1) contd.

ENERGY (MEV)	RANGE (CM)	FITTED RANGE R(E)	FITTED ENERGY E(R)
13.47	.227Ø	.227Ø	13.46
13.78	.2363	.2364	13.76
14.Ø8	.2458	.2458	14.Ø7
14.39	.2555	.2555	14.37
14.69	.2653	.2653	14.67
15.ØØ	.2753	.2753	14.97

direction cosines of the incident and scattered neutron, the direction cosines of the recoil proton are determined. Subroutine DIRECA evalutes these direction cosines by solving the scattering equations using polar co-ordinates and then transforming back to the cartesian system.

It is then possible to determine the distance between the point of collision and the wall of the scintillator in the direction of flight of the recoiling proton using the function subprogram DISTB. If this distance is smaller than the range of the recoil proton as given by equation (6.3Ø) then the energy of the proton as it exits from the scintillator is given by equation (6.31) and the light output is reduced accordingly.

6.5.2. Light Attenuation Effects

The light collection process in a scintillator has been described by Clark (C16Ø) as a random diffusion of the fluorescence photons throughtout the detector volume. The photons undergo absorption by the scintillator medium and at reflection from the scintillator walls before arriving at

the photomultiplier tube. Following the ideas developed in this description Clark developed an approximate relation for the scintillation pulse height. Part of this expression gives the fraction of the light produced that reaches the photocathode. For a cylindrical scintillator the fraction F is given by

$$F = st / (1-rt(1-s)) \qquad (6.32)$$

where r = the reflection coefficient of the scintillator walls,

s = the fraction of the total solid angle subtended the base of the scintillator to the point of scintillation,

and t = the average survival probability for a photon between successive reflections, which is given by $t = \exp(-a\langle p\rangle)$.

The light absorption coefficient 'a' for NE102 is given by the manufacturers (Nuclear Enterprises) to be a=1/170 cm. For a cylindrical scintillator it is assumed (Sc69) that the average photon path length is given by $\langle p\rangle = 4V/S$ where V is the volume and S is the total surface area.

Equation (6.32) was initially thought only to be significant correction for large scintillators, however, it was suggested by Faissner (Fa63) that it might also be significant for smaller scintillators of sizes comparable to those used here. This suggestion was verified by Kujper et al (Ku66) and DeLeo et al (De74). It was also indicated by the early work of Evans and Bellamy (Ev59) who obtained a smaller pulse height for a 5.08 cm scintillator than they did for a 1.27 cm scintillator when bombarded with protons

with energies up to 14 MeV.

Thus for every scattering event the fraction as given by equation (6.32) is evaluated by the function subprogram FRAC. The subprogram uses the function subprogram FSA to evaluated the fraction of the total solid angle subtented by the base using a numerical integration technique.

7. RESPONSE FUNCTIONS

The response of the NE1Ø2 scintillators, used in the present experiments, to protons is of primary importance if the Monte Carlo code is to reproduce accurately the pulse height spectrum. Organic scintillators fluoresce as a result of ionization by charged particles. Neutrons and gamma rays are detected because of the recoil nuclei and electrons they produce. The fluorescence produced is a characteristic of the molecular structure of the scintillator and involves only a small fraction of the total ionization energy most of which is dissipated non-radiatively as heat. The fraction of the ionization energy converted to fluorescence, that is, the scintillation efficiency, depends on the ionizing particle, and is smaller for more heavily ionizing particles of the same energy.

This feature of organic scintillators can be understood in terms of quenching. The fluorescent emission is produced by: the decay of molecular states excited by the incident particle; by secondary electrons produced by the particle; by ion recombinations; or by X-ray or ultra-violet photons emitted following ion recombination (Br79). The fluorescent emission is reduced, however, when there is a region of high excitation density because, in addition to the normal radiative decay channels, non-radiative decay channels become accessible through mutual interactions of the excited molecules. These quenching processes compete strongly with the rapid ($< 10^{-10}$ secs) de-excitation processes which feed the radiative states. The quenched process produces the

fast (2 to 30 nsec) decay component of an organic scintillator. Whereas the slow component (typically > 300 nsec) is attributed to the decay of states excited by ion recombination. In this case the quenching effect has been substantially reduced because the time delay has resulted in a reduction of the ionization density. Thus the relative integrated intensities of the prompt and delayed components depend on the dE/dx of the particle producing the ionization which provides the basis for particle identification by means of pulse shape analysis (PSA) which will be discussed later.

It has been found that the electron response for NE102 is linear above 125keV (Cr70), whereas the response for protons and carbon is non-linear up to much higher energies. Birks (Bi51) proposed a very successful semi-empirical model to describe these phenomena taking into account the quenching processes which are governed by the energy deposited per unit distance along the particle's path. The relation between the specific fluorescence dL/dx (which represents the number of scintillation photons emitted per unit distance) and dE/dx was given by Birks to be

$$dL/dx = S\,(dE/dx) \,/\, (1+kB(dE/dx)) \qquad (7.1)$$

where kB represents the density of quenching centres and S the scintillation efficiency. This expression was modified by Chou (Ch52) with the inclusion of an additional parameter such that

$$dL/dx = S\,(dE/dx) \,/\, (1 + kB(dE/dx) + C'(dE/dx)^2) \qquad (7.2)$$

which reduces to equation (7.1) for small values of dE/dx. From equation (7.2) the total light emitted by a charged

particle which loses all of its energy E within the scintillator is given by (Cr70)

$$L(E) = S \int_0^{\epsilon} [1 + kB(dE/dx) + C'(dE/dx)^2] \, d\epsilon \qquad (7.3)$$

In the case of electrons $dE/dx \approx 0$ for $E >= 125keV$ and so equation (7.3) reduces to

$$L_e(E) = SE + L_o \qquad (7.4)$$

7.1. Data Analysis

Of the two methods of measuring the response of the scintillators, the direct method of bombarding the scintillators with beams of charged paricles was not convenient for the type of detector used. The indirect method of using neutrons and gamma rays to produce recoil charged particles was used. The use of this method has the advantage of minimizing surface effects. If the scintillators were bombarded with a beam of protons most scintillations would occur near the bombarded surface, whereas by using the indirect method scintillations occur throughout the whole volume of the scintillator.

7.1.1. Electron Response

The electron response for each scintillator was obtained by irradiating the scintillators with gamma ray sources and measuring the pulse height spectra. In organic materials the predominant gamma ray absorption mechanism is the interaction with atomic electrons via the Compton effect

(at least at the energies considered). Thus by determining the Compton edge in a pulse height spectrum the electron response is given for an electron energy E_e by

$$E_e = E_\gamma / (\emptyset.511/2 + E_\gamma) \qquad (7.5)$$

The Compton edges of the gamma ray's pulse height spectra of the scintillators used are not readily determinable. In order to overcome this problem the approach of Chikkur and Umakantha (Ch73) was followed in which the high energy region of the pulse height distribution for a particular gamma ray was fitted with a Gaussian from which the channel number for the Compton edge n_e is given by

$$n_e = u + 1.177\sigma \qquad (7.6)$$

where u is the mean and σ the standard deviation of the fitted Gaussian. Chikkur et al only used this approach for liquid scintillators, but because of the similar nature of the scintillation mechanisms in the liquid and plastic scintillators the use of the same approach is justified. The results of such a fitting method are shown in Table (7.1a) and plotted along with fitted functions in Figure (7.1). The high degree of linearity confirms the applicability of equation (7.6). As a further check, the method was used to predict the known Compton edge of a spectrum produced by resolution folding a Compton scattering spectrum produced by a subroutine supplied by Ophel (Op78). The method of Chikkur et al was found to accurately give the Compton edge as can be seen in Figure (7.2).

Table (7.1)

Values for the channel number are given corresponding to the Compton edge for gamma-rays (a) and the proton response obtained using neutrons of various energies (b). The channel numbers were calculated by fitting a Gaussian to the later part of the pulse height spectrum and applying equation 7.6 as used by Chikkur(Ch73). The errors given are the least squares fitting errors. The equivalent electron response was calculated after the fitting of equation 7.4 to the electron data.

(a)

Gamma Energy (MeV)	Electron Energy (MeV)	Channel Number	Error +or-
1.27 cm scintillator			
.511	.341	44.46	.Ø3
.662	.477	64.39	.Ø2
.835	.639	88.7Ø	2.15
.898	.699	91.32	2.94
1.173	.963	136.63	.55
1.275	1.Ø62	143.94	4.53
1.332	1.117	156.54	.41
1.836	1.611	2Ø9.76	5.7Ø
2.54 cm scintillator			
.511	.341	42.42	.Ø3
.662	.477	61.63	.Ø3
.835	.639	85.88	1.5Ø
.898	.699	86.21	1.Ø1
1.173	.963	128.98	.42
1.275	1.Ø62	139.9Ø	1.53
1.332	1.117	149.15	.5Ø
5.Ø8 cm scintillator			
.511	.341	34.52	.Ø2
.662	.477	47.89	.Ø3
.835	.639	63.38	.63
1.275	1.Ø62	1Ø2.48	.89

Table (7.1)

(b)

Neutron Energy (MeV)	Channel Number	Error +or-	Equivalent Electron Energy (MeV)
1.27 cm scintillator			
2.304	115.82	.57	.871
3.007	162.20	2.74	1.220
4.004	225.11	1.04	1.693
5.006	276.99	1.21	2.083
6.011	319.35	1.95	2.401
7.003	357.86	3.01	2.691
8.016	405.99	.62	3.053
2.54 cm scintillator			
2.304	108.13	.10	.789
3.007	152.68	.37	1.114
4.004	210.95	.73	1.540
5.006	264.04	1.50	1.927
6.011	306.40	1.44	2.236
7.003	346.51	1.65	2.529
8.016	390.50	.26	2.850
5.08 cm scintillator			
4.004	146.74	.79	1.561
5.006	185.78	1.04	1.976
7.003	242.09	.93	2.575
8.016	273.40	.43	2.909

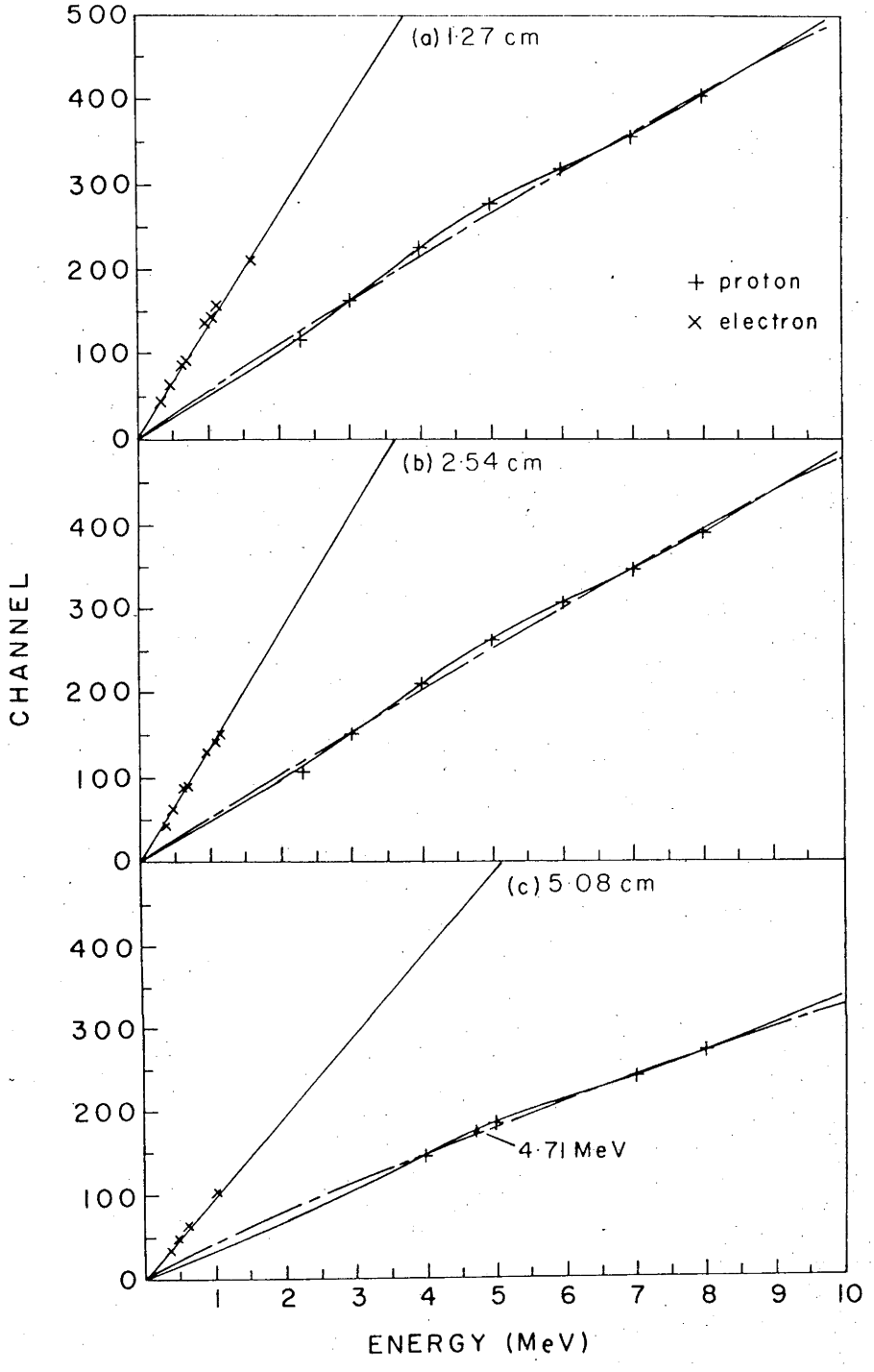

Figure (7.1)

The response data for the three scintillators are shown the electron response data are least squares fitted with eq. (7.4) and the proton response data are fitted with eq. (7.3) { solid line } and eq. (7.7) { dashed line }. Note that in part (c) the independantly obtained 4.71 MeV point is shown to be in good agreement with the points obtained using the Chikkur approach.

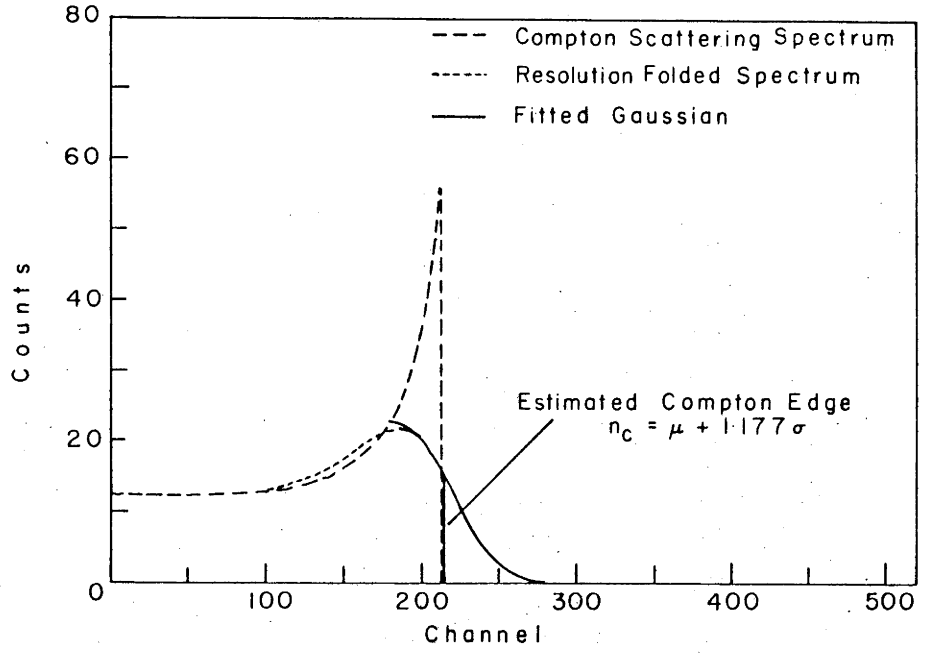

Figure (7.2)
A resolution folded Compton scattering spectrum was fitted with a Gaussian and the Compton edge determined using eq. (7.5) shows good agreement with the real Compton edge.

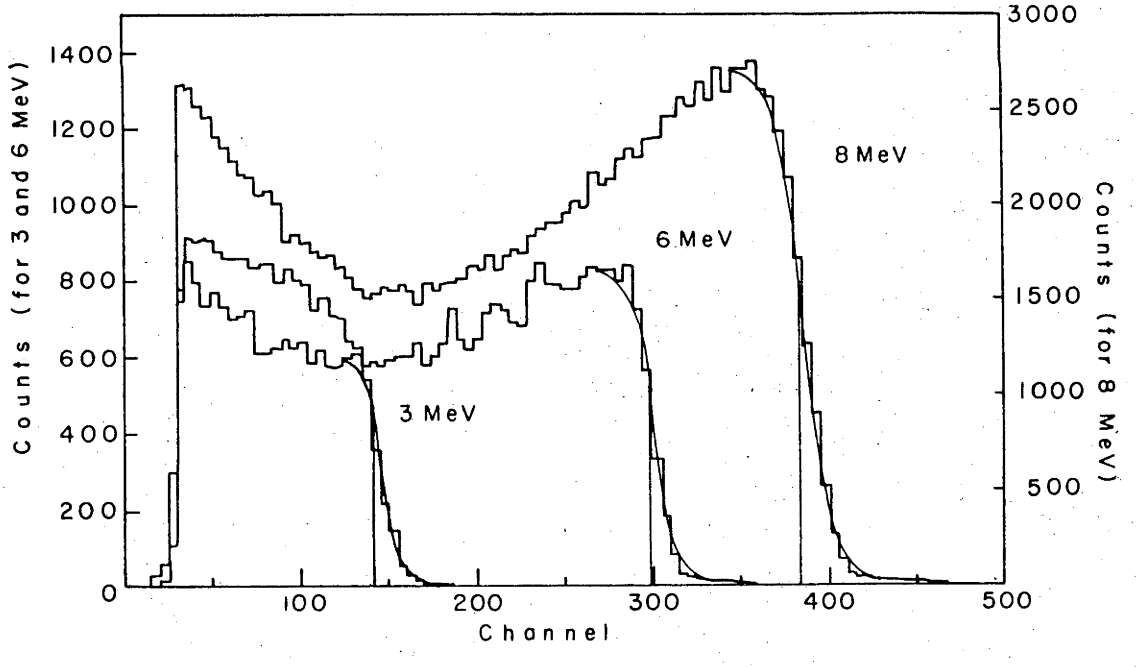

Figure (7.3)
Pulse height spectra produced by neutron beams of 4, 6 and 8 MeV are shown with the proton response channel number determined using eq. (7.6).

7.1.2. Proton Response

A similar problem is encounted in the determination of the proton response from the pulse height spectra produced by a beam of monoenergetic neutrons. In this case the maximum recoil proton energy was due to the incident neutron scattering through 180° c.m.. The Chikkur approach was tried on a set of neutron spectra for the 5.08 cm scintillator resulting in a response curve which fitted the definite response evaluated for E_p = 4.71 MeV in the n-p scattering experiment (continuous, see Chapter 8).

The success of this approach in fitting the data obtained for the 5.08 cm scintillator justifies its use with the other two scintillators. Some neutron spectra for the 2.54 cm scintillator fitted with the appropriate Gaussian functions are shown in Figure (7.3) where it can be clearly seen that the fitted response evaluated by this method is reasonable. Table (7.1b) gives the neutron response data for the three scintillators.

7.2. Results

Electron response data were fitted using a least squares method, with equation (7.4), where L_e (E) corresponding to the channel number and L_o=0 (L_e(0) was set to be zero). The value for the scintillation efficiency parameter S obtained with these fits is the same value for both the electron and the proton data because both sets of

data were taken under identical conditions. Thus the same value for S obtained in fitting equation (7.4) to the electron data was used in fitting equation (7.3) to the proton data. The results of the fits are given in Table (7.2b) along with a comparison of the values of kB and C' obtained by Craun and Smith (Cr70).

The main aim, however, in fitting functions to the response data was not to check the Chou formula, but to provide a means of accurately estimating the pulse height obtained for a proton recoil with any energy within the range of these experiments. Eq. (7.3) would be very time consuming in a Monte Carlo calculation since interpolation of dE/dx data tables and numerical integration would be involved. It is therefore deemed more appropriate to use an expression of the form

$$L_p(E) = AE + B\exp[-((E-C)/D)^2)/2] \qquad (7.7)$$

where A, B, C and D are constants. Equation (7.7) was least squares fitted to the proton response data, the fitted values being given in Table (7.2a). It can be seen from Figure (7.1) that the expression provides a better fit to the data and it was much quicker computationally.

The Monte Carlo program actually requires expressions for the proton and carbon response in terms of the equivalent electron response. For the case of protons the values of $L_p(E)$ obtained from the fitting of equation (7.7) are divided by the values of S obtained from the fitting of equation (7.4) to the electron response data. As no carbon response data were measured, the carbon response was calculated using equation (7.3) and the fitted values of kB,

C' and S, as was done by Batchelor et al (Ba61). An expression fitted to these values gives $L_e(E) = Ø.14E$. This is obviously not as accurate as the proton response function, but due to the carbon response being approximately 3Ø times smaller than the proton response for the same energy deposited, and the small recoil energies for carbon nuclei compared to the recoil energies of the protons, the larger error in the carbon response function becomes unimportant.

Table (7.2)

(a) Fitting equation 7.4 to the electron response data of Table 7.1a gives the values for S shown. The proton data were fitted with equation 7.7 yielding the values for A,B,C and D. The equivalent electron energy for a proton is thus given by evaluating equation 7.7 using the given parameters and dividing by S.

(b) In order to compare the values of kB and C' to those given by Craun and Smith (Cr70) the response data were normalized such that the response for a 0.525 MeV electron is 1000, thus the arbitary units for S. Craun and Smith give $kB=1.29\times10^{-2}$ and $C'=9.59\times10^{-6}$ for NE102 to which the present values compare favourably.

(a)

Scintillator (cm)	S (Ch# MeV^{-1})	Fit using Eq. 7.6 A	B	C	D	χ^2
1.27	133	50.6	25.8	4.71	1.15	5.2
2.54	137	48.7	21.0	4.96	1.14	8.9
5.08	94	34.1	15.1	5.00	1.13	1.9

(b)

Scintillator (cm)	S (Arb. Units)	kB ($g.cm^{-2}.MeV^{-1}$)	C' ($g.cm^{-4}.MeV^{-2}$)	χ^2
1.27	1905	1.26×10^{-2}	4.50×10^{-5}	66
2.54	1905	1.30×10^{-2}	5.49×10^{-5}	83
5.08	1905	1.47×10^{-2}	3.30×10^{-5}	55

8. N-P SCATTERING EXPERIMENT - DISCRETE

Two different experimental approaches were tried to provide a preference for a phase shift set. The first approach by measuring the n-p differential cross section at a discrete angle for a particular energy is presented in this chapter. The second approach, an attempt to unfold a complete differential cross section from the energy spectrum of the recoil protons, is dealt with in Chapter 9. Both approaches required the use of the Monte Carlo program described in Chapter 6, the first to evaluate multiple scattering and edge corrections, and the second to reproduce the energy spectrum from the phase shifts.

8.1. Experimental Procedure

The experimental arrangement is shown schematically in Figure (8.1). It consisted of the neutron source as described in Chapter 3, arranged so that 8 MeV neutrons were produced using an incident deuteron energy of 12 MeV. A cylindrical NE102 plastic scintillator with a diameter of 5.08 cm and a height of 5.08 cm served both as the proton target and as the recoil proton detector. The detector axis was positioned 26.7 cm from the neutron source, the axis being perpendicular to the $D(d,n)^3He$ reaction plane. The scintillator thus subtended an angle of 10.9° encompassing the whole of the neutron beam which had a beam profile defined by a Gaussian with a standard deviation of 1.50° (see Chapter 3). Neutrons scattered through $50.0^\circ \pm 0.1^\circ$ lab

(100.2° ± 0.2° c.m.) by the NE102 scintillator (hereafter referred to as the "scatterer") were detected by an NE213 liquid scintillator (hereafter referred to as the "detector") positioned so that its front surface was 50.0 cm from the axis of the scatterer. The deuteron beam which passed through the deuterated polyethylene target was collected by a Faraday cup mounted 339 cm from the target. The ratio of the ^{3}He count rate to the beam current provided a continuous monitor of the target yield.

The scatterer was painted with Nuclear Enterprises white scintillator paint to provide a reflective surface and bound with a double layer of black plastic tape (0.36 mm thick) to exclude external light. The scintillator was optically coupled to an Amperex 56AVP photomultiplier tube which was mounted on a specially designed base. The circuit diagram for the base is shown in Figure (8.2). The difference between this and a standard base was that the last five resistors in the potential divider resistor chain were replaced by 75 volt zener diodes to ensure greater voltage stability for dynodes 10 to 14, especially at high count rates when the dynode current was no longer negligible compared to the current through the resistor chain. The current drawn by dynodes 1 to 9 was never sufficient to significantly alter the voltage on these dynodes and so zener diodes were not required. The modified base ensured a constant gain independent of the scintillator count rate.

The detector scintillator consisted of NE213 liquid in a metal can 6 cm in diameter and 8 cm in depth. A window at one end of the can was optically coupled to an Amperex 56AVP

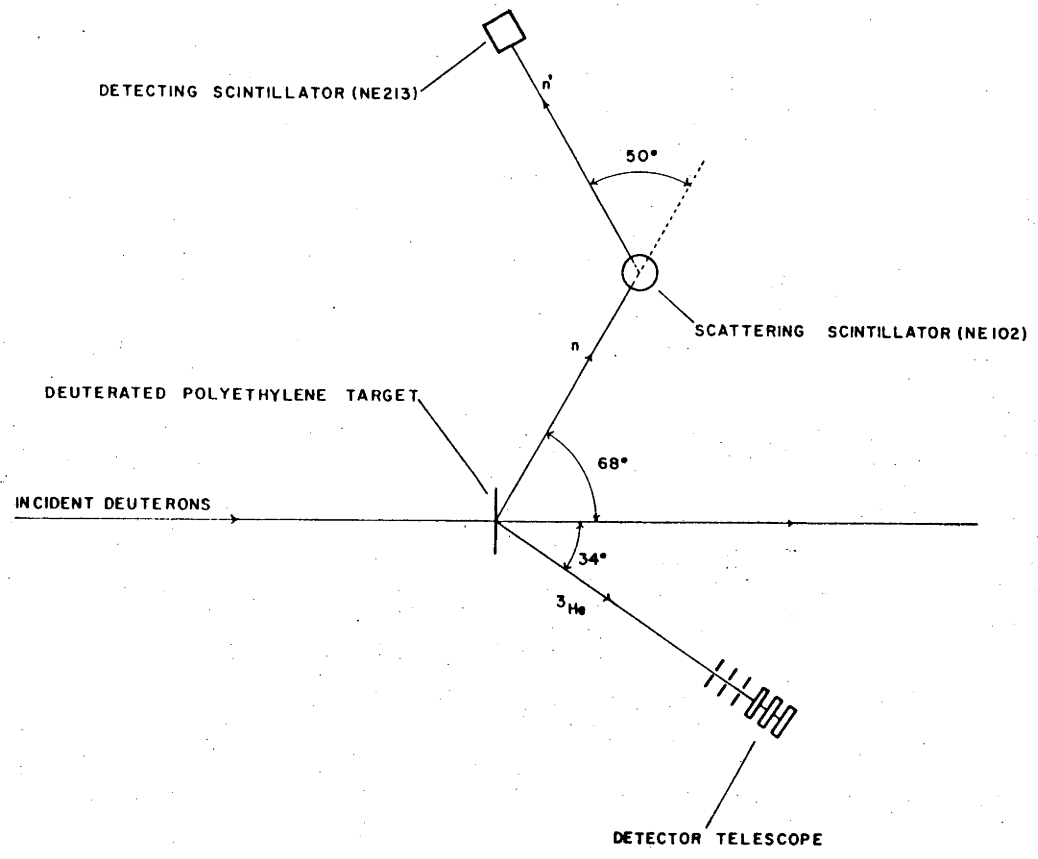

Figure (8.1)
Schematic representation of the experimental arrangement for the multiple scattering experiment.

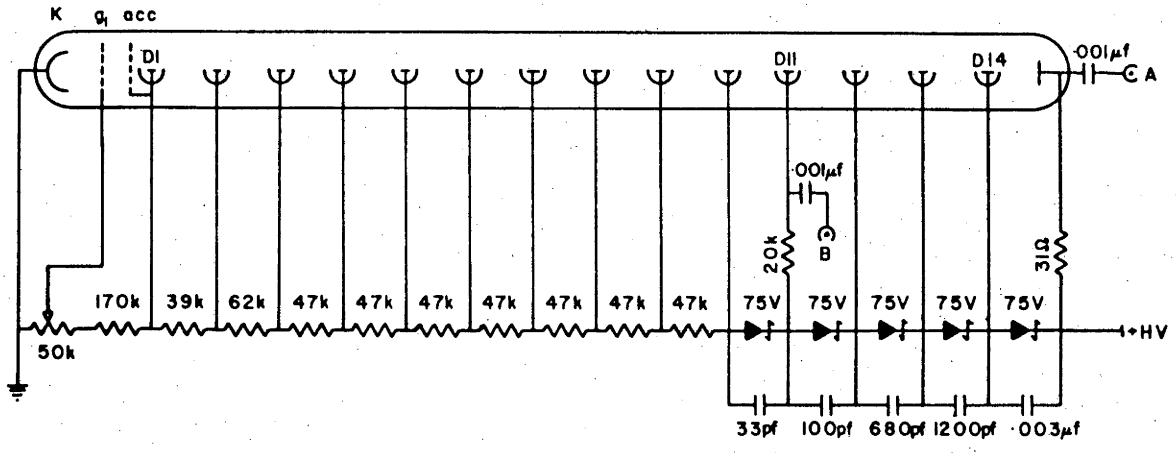

Figure (8.2)
Circuit diagram for the modified photomultiplier tube base used with the scatterer. The zener diodes were included to provide good gain stability over a large dynamic range. The timing and linear signals were taken at points A and B respectively.

photomultiplier tube mounted on an Ortec 269 tube base.

The electronics used consisted of the ^{3}He particle identification electronics, as described in Chapter 3, plus two timing circuits, one for the scatterer and one for the detector, as shown in Figure (8.3). Both "time to amplitude converters" (TACs) used a start pulse generated by a ^{3}He event with the stop pulses being derived from the appropriate scintillator. The output of the ^{3}He$\longrightarrow$detector TAC and the scatterer pulse height signal were gated when a three way coincidence occurred between a ^{3}He logic pulse, a logic pulse from the ^{3}He$\longrightarrow$scatterer TAC and a logic pulse from the pulse shape analyser (PSA) connected to the detector. The two spectra were collected in event mode using an IBM 1800 disk mega collection system. The ^{3}He-scatterer TAC spectrum was gated using the same triple coincidence but was collected separately on a Nuclear Data 2400 multichannel analyser. The logic pulse from the ^{3}He-scatterer TAC was obtained from a single channel analyser with a window set on the peak corresponding to n-p scattering events. The window setting is shown in Figure (8.4).

The pulse shape analyser was set to eliminate a large number of gamma ray events in the detector. As an absolute cross section was being measured it was important not to exclude any neutron events, consequently it was necessary to allow some gamma events within the PSA window. The tight restrictions on timing were imposed to eliminate the remaining gamma events. Figure (8.5) shows the position of the window on the PSA spectrum.

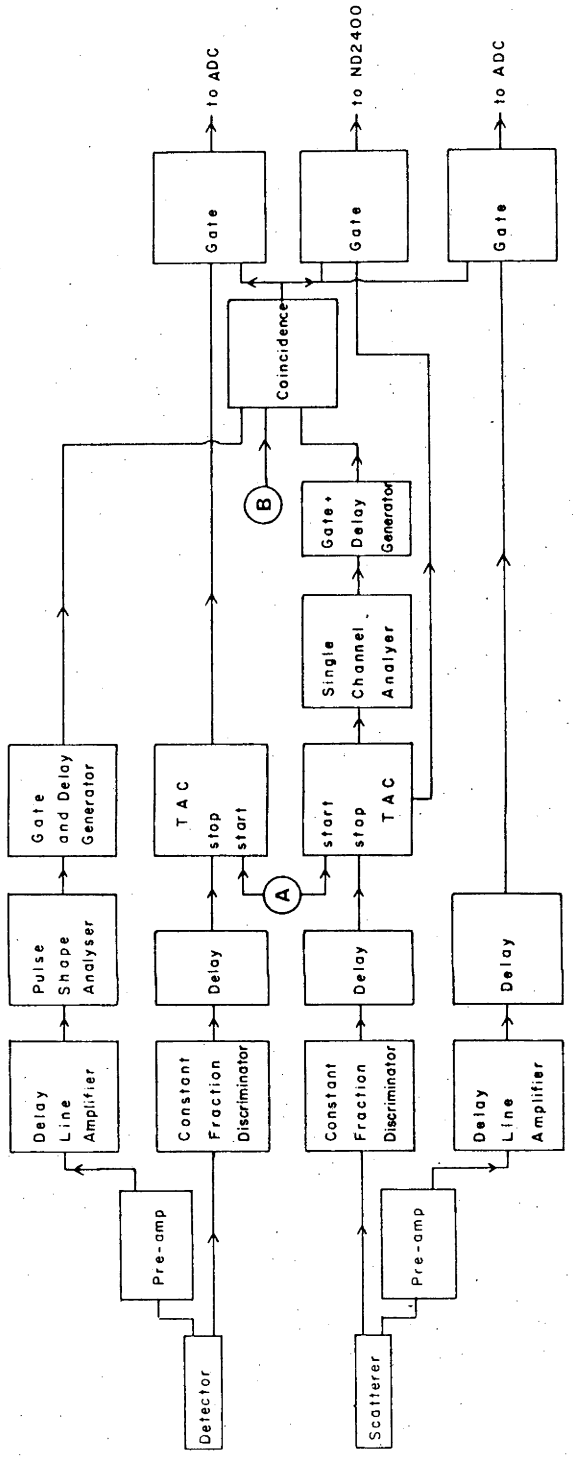

Figure (8.3)
Circuit diagram used for the double scattering experiment. Points A and B are inputs from the ^{3}He particle identification circuit shown in Figure (2.2).

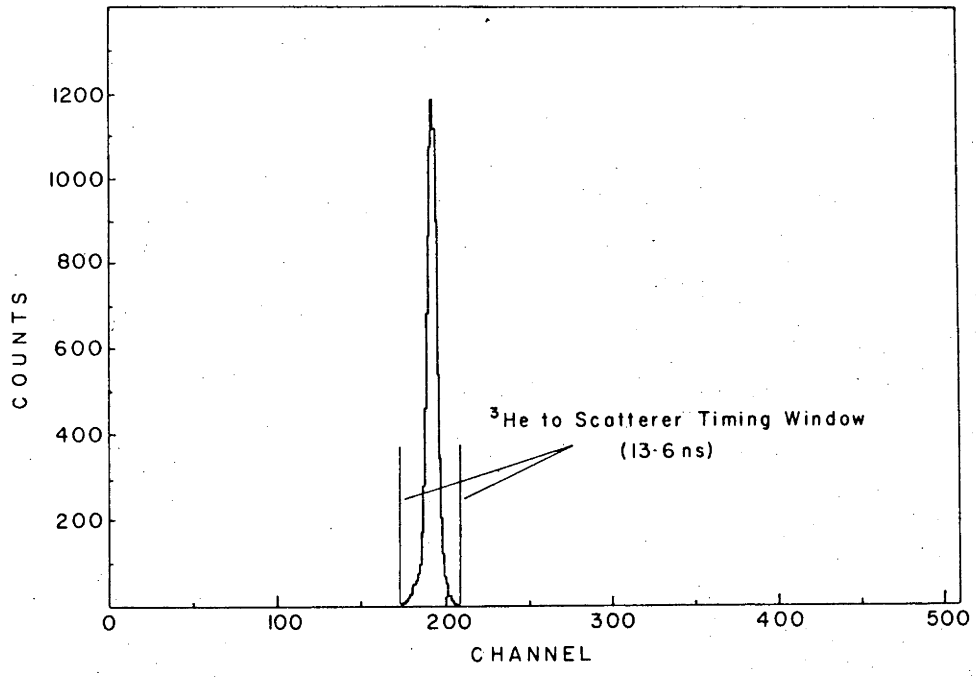

Figure (8.4)
Timing spectrum for the ^{3}He ⟶ scatterer TAC showing the position of the timing window.

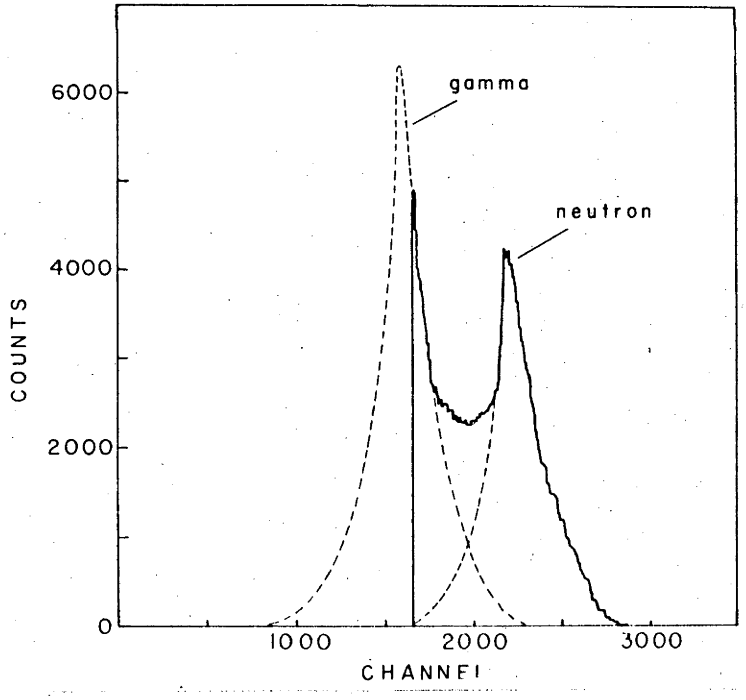

Figure (8.5)
Pulse Shape Analyser spectrum. The solid line shows the spectrum produce with the window applied and the dashed lines show the extensions of the gamma and neutron peaks.

8.2. Results

Data were collected for 23.7 hours yielding 20 x 10^6 ^{3}He events. Total projections of the collected data are shown in Figures (8.6a) and (8.7a). The timing spectrum, Figure (8.6a), consists of the main timing peak with a broadening at the base on the faster side. The small peak near channel 50 is probably due to gamma rays emitted from the deuteron beam collimator.

The linear energy spectrum for the scatterer, Figure (8.7a), clearly shows a large peak centred near channel 35 which corresponds to the 4.71 Mev recoil protons produced by a single n-p interaction involving the scattering of 8 MeV neutrons through 50° (lab.). The other smaller peaks in this spectrum will be discussed in section (8.3.1) on multiple scattering.

By setting a window on the 4.71 MeV recoil proton peak (channels 26 to 43) to project the timing spectrum, a much cleaner timing spectrum results, as shown in Figure (8.6b). The width of this peak is primarily due to the solid angle of the detector which was such that neutrons scattered between 46.6° and 53.4° (lab.) were detected. This range of angle with the depth of the detector meant that the difference in the time of flight of the detectable neutrons at either extreme was 6.1 ns. Additional broadening was caused by the energy spread of the neutron beam. The detector's geometry was also responsible for a 0.96 MeV spread in the scatterer energy spectrum. A projection of the energy spectrum with a window on the timing peak

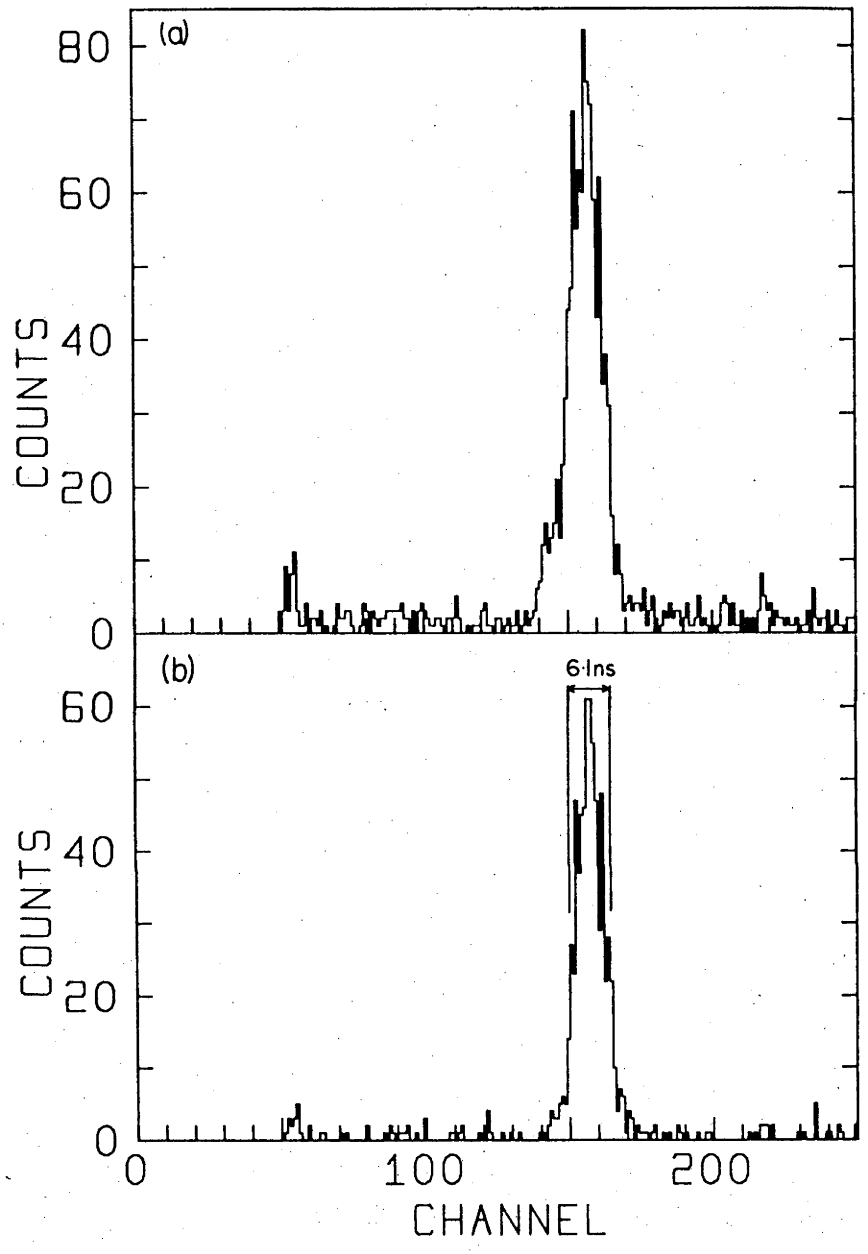

Figure (8.6)
The timing spectrum produced by the $^{3}He \longrightarrow$ detector TAC. Part (a) is a total projection and part (b) is a projection with a window set on the scatterer energy spectrum (Figure (8.7)) between channels 26 and 43.

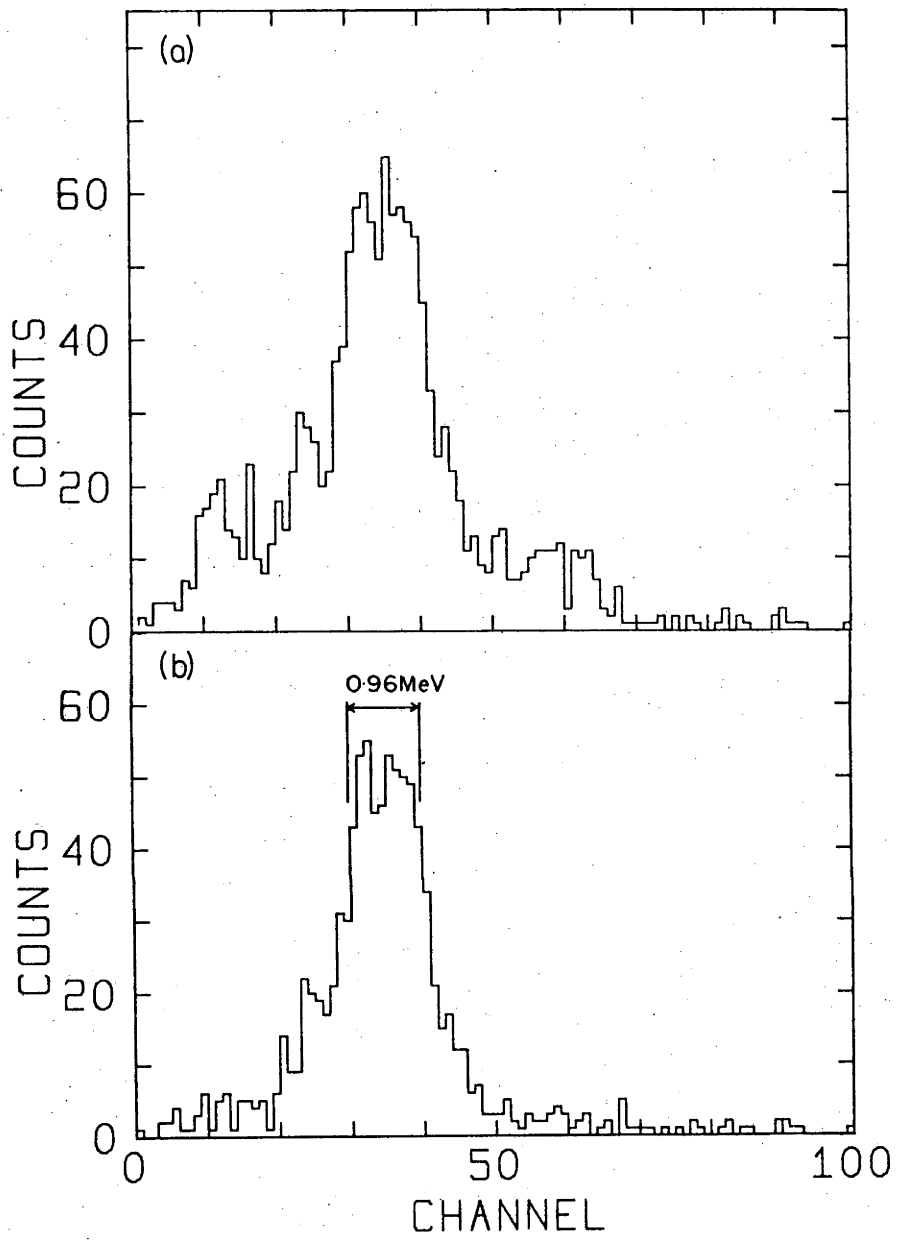

Figure (8.7)
The linear energy spectrum of the scatterer with the background subtracted. Part (a) is a total projection and part (b) is a projection with a window set on the $^{3}He \longrightarrow$ detector TAC spectrum (Figure (8.6)) between shannels 146 and 170. This spectrum was produced by summing groups of 5 channels to compress the original 512 channel spectrum.

(channels 146 to 170) gave the much cleaner energy spectrum, shown in Figure (8.7b). Integrating the 4.71 MeV peak of Figure (8.7b) yielded 712 ± 28 counts.

8.3. Corrections

8.3.1. Multiple Scattering

In order to gain a better understanding of the energy spectrum of Figure (8.7) with regard to multiple scattering, the Monte Carlo program was used to simulate the experiment. Figure (8.8a) shows the simulated scatterer spectrum with a break down of this total spectrum shown in parts (b) to (f). Part (b) shows the well defined peak produced by single n-p scattering events. The width of the peak is determined by the spread in the incident neutron energy and the finite solid angle of the detector. As expected, the peak is quite square due to the square profile of the detector used in the Monte Carlo code. In the actual experiment the detector profile was circular thus producing a peak with a rounder shape. The Monte Carlo code also failed to take into account the resolution of the scatterer. To correct for this resolution folding was performed producing the total spectrum shown in Figure (8.8g).

Parts (c), (d), (e) and (f) of Figure (8.8) show the spectra produced by double n-p scattering, triple n-p scattering, a n-p scattering event followed by a n-C scattering event and a n-C scattering event followed by a

n-p scattering event respectively. The smaller peak near channel 60 is clearly shown by parts (c) and (d) to be due to multiple n-p scattering whereas the peak at the lower energy is contributed to by multiple scattering involving both a hydrogen and a carbon scattering event as shown by parts (e) and (f). One interesting feature that all the multiple scattering components have in common is their essentially flat nature in the region of the single n-p scattering peak. This indicates that by fitting a Gaussian with a background to the 4.71 MeV peak of Figure (8.7b) one is eliminating all the multiple in-scattering events. In-scattering is a sequence of two or more scattering events, one of which is an n-p scattering event, which results in a neutron being scattered towards the detector. The sequence must contain a hydrogen scattering event since the discriminator threshold on the scatterer was set above the maximum light output for both carbon recoils and alpha particles from reactions with carbon.

The opposite effect, out-scattering occurs when a neutron, initially scattered towards the detector by a hydrogen event, is subsequently scattered away from the detector by either a hydrogen or a carbon in its path. This is in fact a standard exponential attenuation of the outgoing neutron beam. The Monte Carlo code was used to estimate the reduction in the number of detected neutrons due to out-scattering. The value obtained was 30.5%. [The code gave the in-scattering value to be 35.4%. This is not a measure of the background as they are spread over the entire spectrum and not just in the peak of interest.]

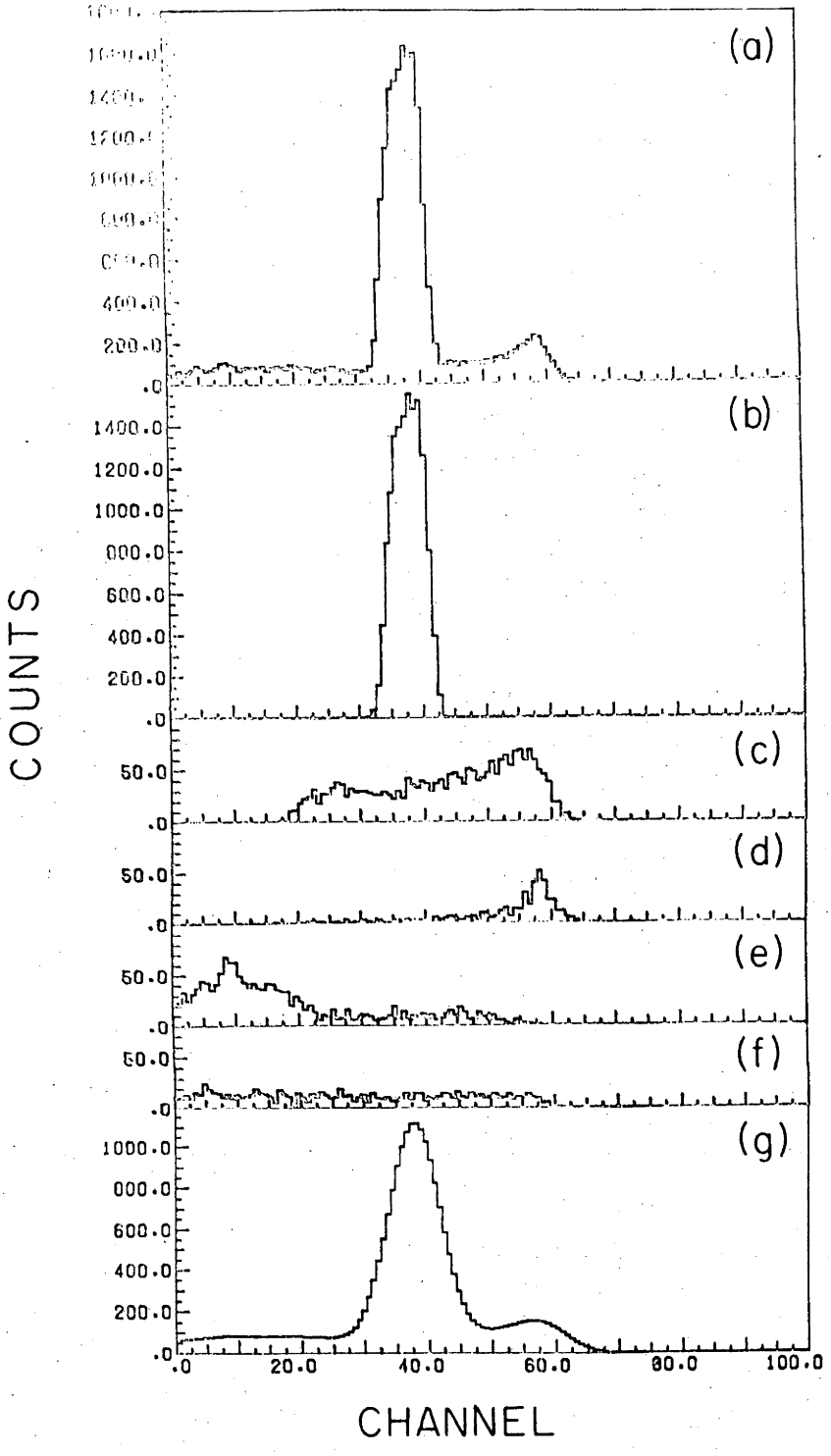

Figure (8.8)

A Monte Carlo simulation of the linear energy spectrum. Part (a) is the total spectrum. Parts (b), (c), (d), (e) and (f) show the spectra produced by single n-p scattering, double n-p scattering, triple n-p scattering, an n-p scattering event followed by an n-C scattering event, and an n-C scattering event followed by an n-p scattering event respectively. Part (g) shows part (a) after resolution folding was performed.

8.3.2. Attenuation Outside the Scatterer

The effect of exponential attenuation of the neutron beam between the source and the scatterer, and between the scatterer and the detector must also be considered. Between the source and the scatterer the neutron beam was attenuated by the 0.87 mm of the stainless steel scattering chamber wall, the air, and the layer of plastic tape with a combined effect of a 3.67% attenuation. The neutrons scattered towards the detector by the scatterer were attenuated by the layer of plastic tape and the air resulting in a 1.51% attenuation. The attenuation effect of the detector's metal container are taken into account in the detector's efficiency measurements.

8.3.3. Attenuation Within the Scatterer

The equation used to evaluate the differential cross section (equation (8.5)) was based on the approximation that the neutron beam was constant throughout the scatterer. This approximation is only good for a thin target. For the size of the scintillator used here the attenuation of the neutron beam is quite significant and so a correction must be applied to the result obtained from equation (8.5).

To evaluate the correction the scatterer was partitioned into 25 segments (5 in the horizontal and 5 in the vertical plane). The mean differential cross section $\bar{\sigma}(\bar{\theta})$ for the mean scattering angle $\bar{\theta}$ is thus given by

$$\bar{\sigma}(\bar{\theta}) = (1+\zeta)\sigma(\theta) \qquad (8.1)$$

where

$$(1+\delta) = \left[\sum_{i=1}^{25} P_i T_i T_i' (V_i/V)(d_{13}/d_i)^2 \right]^{-1} \qquad (8.2)$$

P_i is the fraction of the incident neutron beam reaching the ith segment. T_i is the transmission of the incoming neutron beam through half the thickness of the ith segment. T_i' is the transmission of the outgoing neutron beam through the remainder of the scintillator towards the detector. T_i' was set to 1 for the evaluation of equation (8.2) as the correction for out-scattering has already been made. T_i' was assigned the correct value when used in equation (8.3). V_i is the volume of the ith segment and V the total scintillator volume. The distance from the centre of the 13 th segment (the centre of the scintillator) to the detector is d_{13} and the distance from the centre of the ith segment to the detector is d_i. The factor $(d_{13}/d_i)^2$ thus corrects for the varying solid angle subtended by the detector at different parts of the scintillator. The value of δ was 0.401 for the present experimental configuration.

The average scattering angle $\bar{\theta}$ was calculated using

$$\bar{\theta} = \left[\sum_{i=1}^{25} \theta_i V_i P_i T_i T_i' (1/d_i^2) \right] / \left[\sum_{i=1}^{25} V_i P_i T_i T_i' (1/d_i^2) \right] \qquad (8.3)$$

where θ_i is the scattering angle at the centre of the ith segment. It was found that $\bar{\theta} = 50.02^\circ$ which was within the uncertainty of θ.

8.3.4. Wall Effects

In the case of a n-p scattering event near the edge of

the scintillator the recoil proton may escape from the scintillator before depositing all of its energy. Thus it is possible that the detected energy is below the window set for a valid event, which meant that valid events went undetected. To correct for this the Monte Carlo code was again used (section (6.5.1). The correction to the differential cross section was determined to be Ø.Ø8%.

8.4. Detector Efficiency

The absolute measurement of the detector efficiency was performed immediately following the double scattering experiment so that the efficiency measurements were made using exactly the same discriminator and gain settings as used during the experiment.

The efficiency measurements were made using the same logic circuit , shown in Figure (3.2), with the number of neutron counts evaluated in the same way as for section (3.2). The detector efficiency was given by

$$\varepsilon = (\text{no. of n's} + \text{attenuation correction})/(\text{no. of } {}^{3}\text{He's}) \qquad (8.4)$$

The attenuation correction takes into account the neutron attenuation in the scattering chamber wall and the air, but not the scintillator container. The attenuation in the container was the same during the efficiency measurement as during the experiment and so was considered to be an intrinsic part of the detector efficiency.

Efficiency measurements were made at the neutron energies 1Ø, 8, 7, 6, 5, 4 and 3 MeV with the detector at

distances ranging from 17.Ø cm to 47.Ø cm from the neutron source. It was found that the efficiency varied as a function of distance from the source , shown in figure (8.8), in the case of 7 MeV neutrons. It can be seen that the efficiency was maximum when the whole of the detector was irradiated with neutrons. The efficiency was reduced when the distance was such that neutrons missed the detector and was also reduced when the distance was such that the neutron beam passed through only the centre region of the scintillator. The maximum efficiency was taken to be the efficiency applicable to the experiment because the whole of the scintillator was essentially uniformly irradiated during the experiment.

The efficiency, as a function of energy, is shown in Figure (8.9). As expected it decreased as the energy was reduced below 6 MeV due to the discriminator threshold. The efficiency for 3.29 MeV neutrons was interpolated to be Ø.111 $\pm$ Ø.ØØ1 .

8.5. Discussion

The differential cross section prior to applying any of the corrections is given by

$$\sigma_{\Omega}(1ØØ.17^{o}\text{c.m.}) = C/(N_{o}\,\varepsilon\,\Omega\,\bar{N}) \qquad (8.5)$$

where C = number of neutrons detected at 1ØØ.17 c.m.

N_o = number of incident neutrons

ε = detector efficiency

Ω = the detector solid angle (c.m.)

and $\bar{N}$ = the mean number of scattering centres per unit

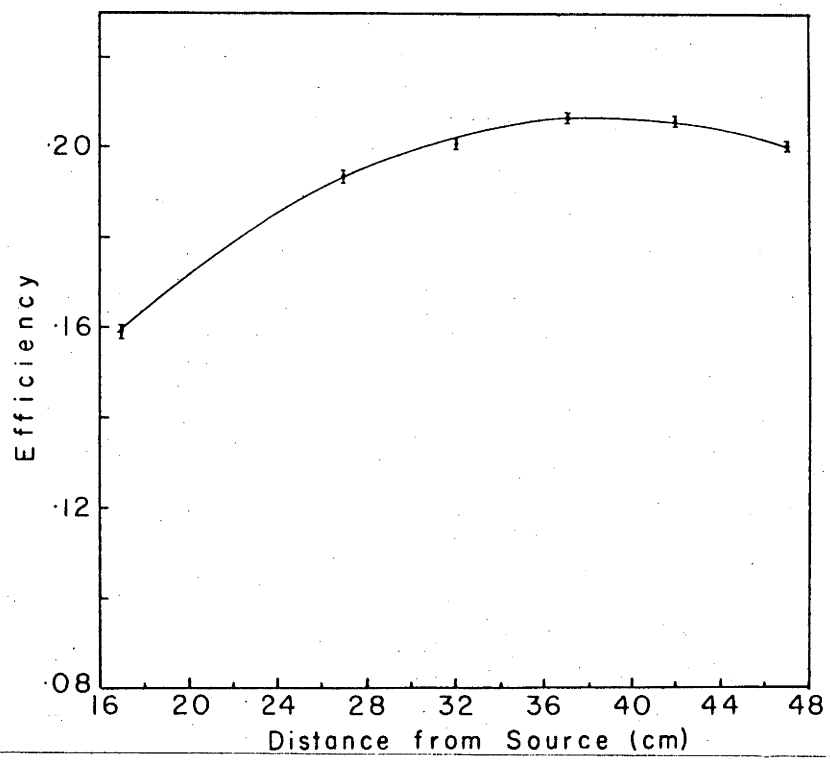

Figure (8.9)
Efficiency of the detector for 7 MeV neutrons as a function of distance from the neutron source.

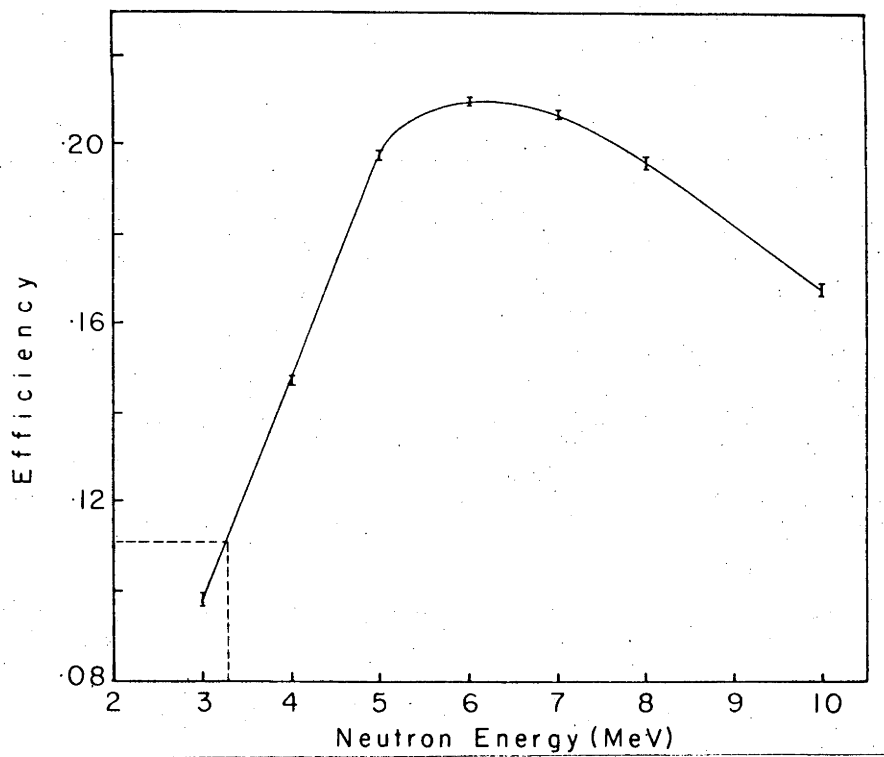

Figure (8.10)
Efficiency versus neutron energy for the detector showing the efficiency for 3.29 MeV neutrons.

area. $\overline{N}$ is obtained by multiplying the number of scattering centres per unit volume by the mean neutron path length through the scatterer $\overline{L}$. Calculation of $\overline{L}$ involved the weighting of the geometric path length with the beam profile Gaussians, which were determined in chapter 3. Evaluation of equation (8.5) gave σ_{λ} (100.17° c.m.) = 50.5 ± 6.2% mb/sr. Applying the corrections as discussed in section (8.3), the result became σ_{λ} (100.17° c.m.) = 88.9 ± 5.5 mb/sr. No uncertainty was applied to the corrections. This result is consistent with the values obtained from the LRL and Yale phase shifts as reported by Hopkins and Breit (Ho71). Figure (8.11) shows the current result in relation to the predictions.

The major problems associated with the current experimental approach are the slow count rate and the large corrections which need to be applied. The slow count rate (<1 per minute) meant that a data collection for approximately 80 hours would be required to obtain sufficient counts for a statistical error of less than 2%. During such a long period it would be unrealistic to expect gain and discriminator settings to remain sufficiently constant. The count rate could be increased by using an array of detecting scintillators so as to increase the solid angle but not the angular acceptance. (In the current experiment only 2% of the neutrons scattered through 50° and within the angular acceptance range were incident upon the detector.) Increasing the yield of the neutron source would be difficult.

The large corrections, which were needed for this

experiment, would be dramatically reduced if a a smaller scattering scintillator were used. (This nett reduction in the corrections required would be greatly reduced in spite of the increasing wall effect). This would have meant redesigning the scattering chamber to allow the scatterer to be positioned closer to the neutron source to ensure that the entire neutron beam was encompassed.

It has been demonstrated that Monte Carlo techniques have enabled the use of a large scintillator which involves large corrections to be calculated. However, it is desirable to reduce the size of these of corrections, and perhaps more importantly, to improve the statistics for the experiment.

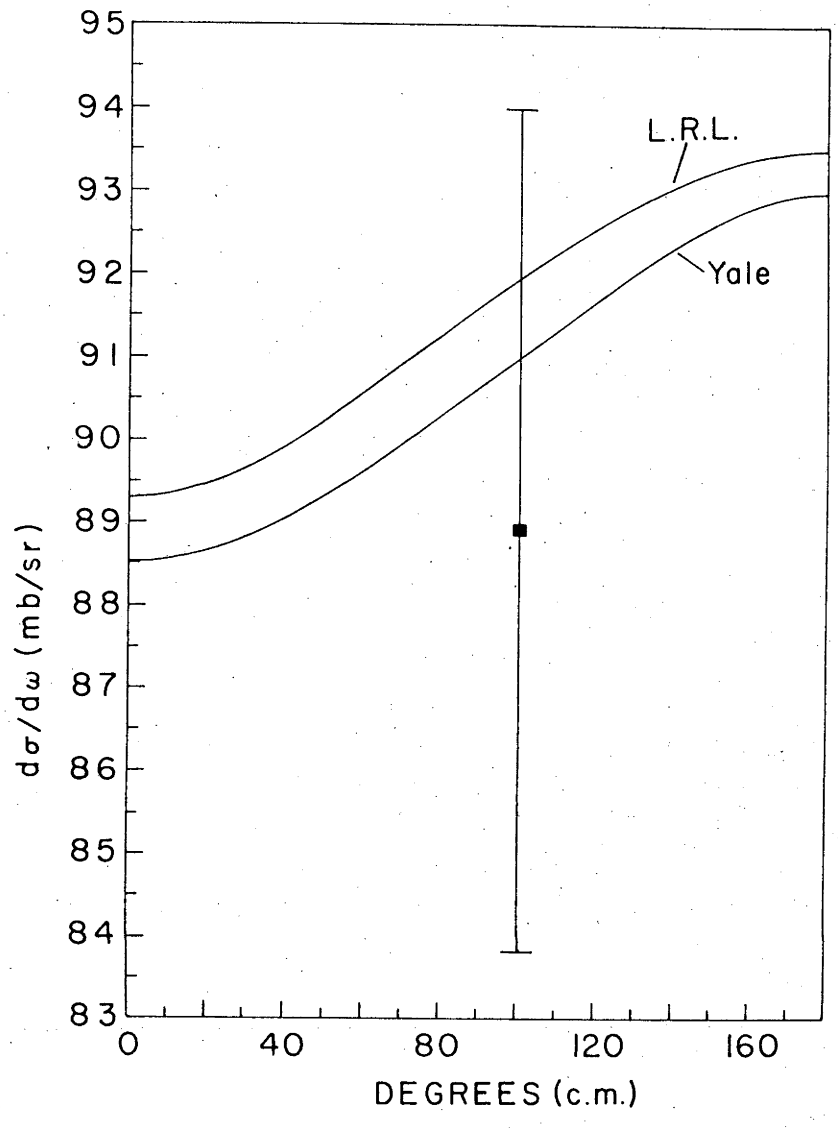

Figure (8.11)
The data point obtained is shown compared to the phase shift set predictions from Yale and LRL. The large error bars are primarily due to the poor statistics.

9. N-P SCATTERING EXPERIMENT - CONTINUOUS

The continuous approach was based on the fact that the shape of the recoil proton spectrum in a scintillator is determined in part by the angular distribution for n-p scattering. In principle, a Monte Carlo program can be used to reproduce the experimental spectrum provided that the program is given the angular distribution. It should therefore be possible to extract the angular distribution with the use of a Monte Carlo program.

9.1. Experimental Procedure

The experimental arrangement consisted of a cylindrical scintillator aligned axially with the neutron beam. The front surface of the scintillator was positioned 18.5 cm from the neutron source. The neutrons were obtained using the neutron source arrranged so that 12 MeV deuterons produced 8.Ø16 MeV neutrons. As before, the transmitted deuteron beam was collected in a Faraday cup 339 cm from the deuterated polyethylene target. The integrated charge together with the ^{3}He yield provided a continous monitor for the target. A schematic diagram of the arrangement is shown in Figure (9.1).

Two sets of measurements were made, both using NE1Ø2 scintillators 3.81 cm in diameter. The scintillators thus subtended an angle of 11.8^{o} which encompassed the whole of the neutron beam. The neutron beam profile was defined by a Gaussian with a standard deviation of 1.5Ø^{o} (see Chapter 3).

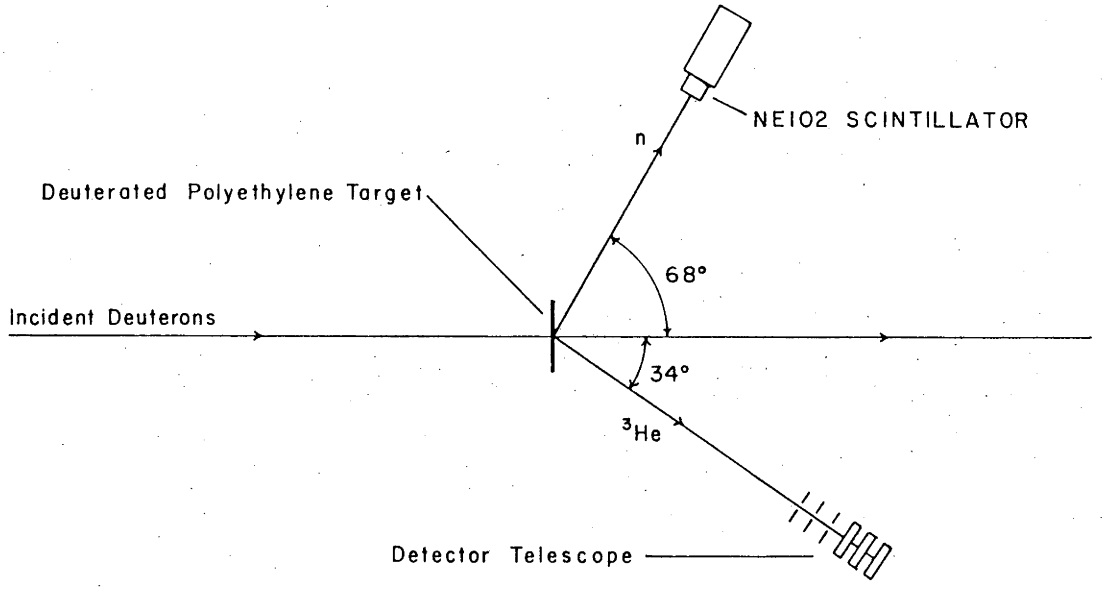

Figure (9.1)
Schematic diagram of the experimental arrangement

The depths of the "small" and the "large" scintillators were 1.27 cm and 2.54 cm respectively. Both scintillators were painted with white reflecting paint (manufactured by Nuclear Enterprises). When in use each scintillator was optically coupled to an RCA 8575 photomultiplier tube. The scintillator and tube were housed in a light proof, water-cooled jacket which incorporated the photomultiplier tube base. A Ø.16 mm thick brass entrance window in front of the scintillator caused only Ø.42% attenuation for 8 MeV neutrons. The water-cooled jacket ensured excellent gain stability despite temperature variations in the target room.

The electronics consisted of the ^{3}He particle identification electronics as described in Chapter 3 (Figure (3.2)). The scintillator energy spectrum and the ^{3}He $\longrightarrow$ scatterer timing spectrum were collected in event mode using

an IBM 1800 tape collection system. The ^{3}He particle identification spectrum was collected simultaneously by a Nuclear Data 2400 multichannel analyser. Timing constraints were imposed on the energy spectra during the sorting of the data.

Spectra were recorded for both scintillators at neutron energies of 8.016, 7.003, 6.011, 5.006, 4.004, 3.007 and 2.304 MeV. In addition, spectra from gamma ray sources were collected to provide a gamma ray calibration. These neutron and gamma ray data were used to obtain the response functions as described in Chapter 7.

9.2. Results

Data were collected for 7.5 hours at 8 MeV yielding 3.5×10^{6} ^{3}He events. For the other energies, collection times were less than an hour with 2.5×10^{5} ^{3}He events. The spectra produced by 8 MeV neutrons in the large scintillator are shown in Figure (9.2) parts (a) and (b). Part (a) shows the timing spectrum and part (b) the projection of the energy spectrum sorted with a window on the timing peak (channels 300 to 336). Projections of the energy spectra for other incident neutron energies are shown in Figure (7.3).

The timing spectra were very clean with only a very small tail on the fast side of the main peak. All events in the energy spectra can thus be considered to be neutron events. The energy spectra showed clearly the lower level discriminator setting of 0.65 MeV equivalent neutron energy. The upper end of the spectra (channel 365 for 8 MeV neutrons)

yielded the resolution of the detection system. The resolution of the system for a given energy was evaluated following the approach of Chikkur and Umakantha (Ch73), where a Gaussian was fitted to the upper edge of the spectrum. Standard deviations thus obtained were later used in a Gaussian resolution folding routine which was used to simulate the resolution properties of the detection system to allow spectra produced by the Monte Carlo program to be compared with the experimental spectra. For 8 MeV neutrons the resolution folding constant was 4.4 channels.

9.3. Analysis

Initial spectra produced by the Monte Carlo program were obtained assuming isotropic n-p scattering. In order to produce a spectrum with acceptable statistics 200,000 neutron events were required, with the program "forcing" every neutron to have at least one collision (see section 6.4.2). In the process of forcing a collision, a weighting factor was calculated to derive absolute efficiencies. Such a calculation involving 200,000 neutrons required 80 minutes execution time on the ANU Univac 1100 computer. It had initially been hoped that an iterative technique could be applied to the Monte Carlo calculations so that a set of differential cross sections could be obtained which exactly reproduced the data. But such a process would have caused difficulties in the execution time (80 minutes per iteration) had the quality of the fit to the experimental data been good enough to enable it to be performed.

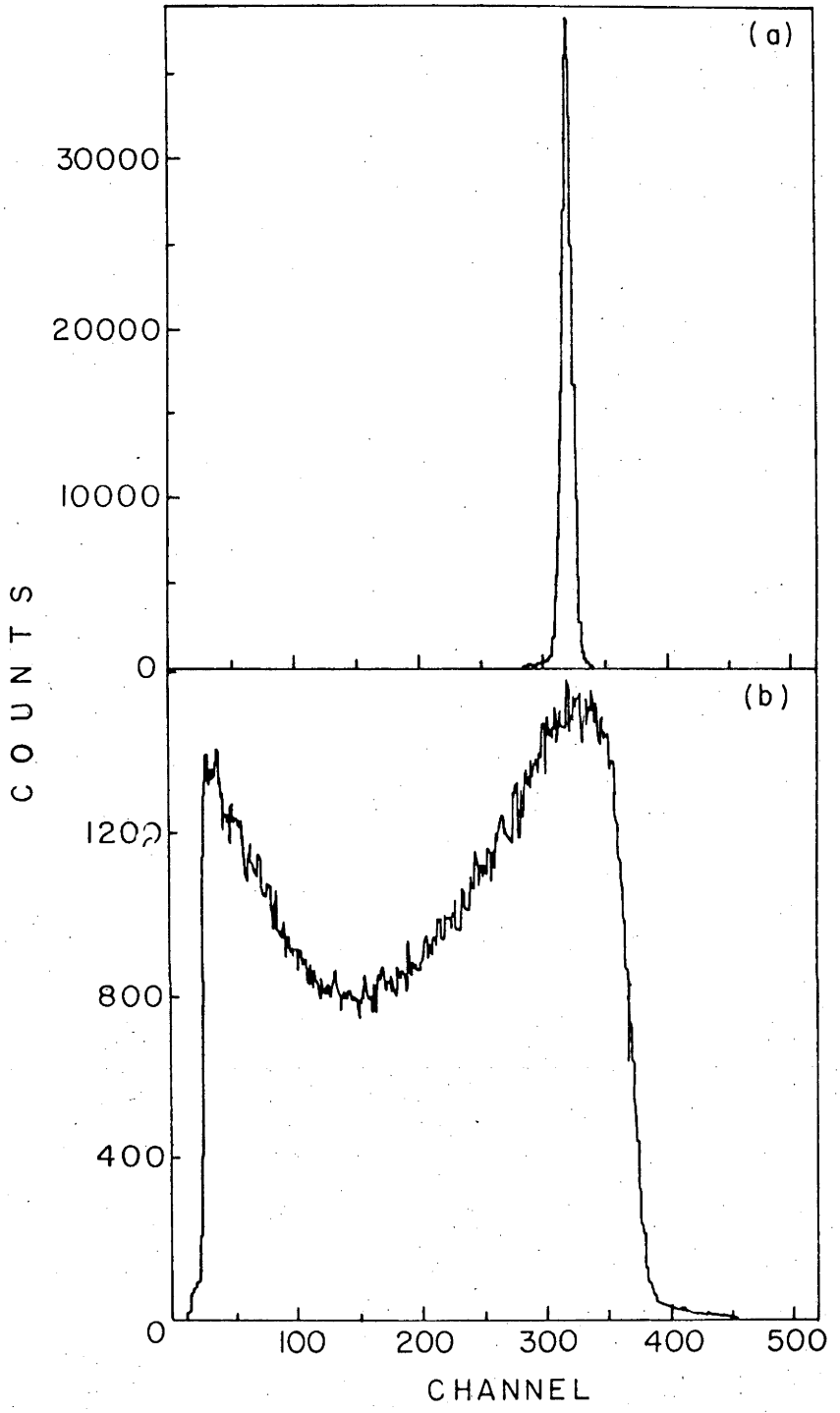

Figure (9.2)
Spectra obtained for the large (2.54 cm) scintillator. Part (a) shows the timing spectrum. A window on the timing peak was used in the projection of the energy spectrum shown in part (b).

Table (9.1)
A breakdown of the relative occurrence of different types of scattering events.

Type of Event	Small Scintillator		Large Scintillator	
	% Valid	% Total	% Valid	%Total
Single n-p scattering	71.8	35.Ø	62.2	31.5
Single n-C scattering	Ø	47.6	Ø	44.5
Double n-p scattering	7.3	3.6	9.2	4.7
Triple or more n-p scattering	2.2	1.Ø	3.1	1.6
n-p plus n-C scattering	12.5	9.5	15.5	12.3
n-p plus n-C plus other	6.2	3.3	1Ø.Ø	5.5
Total multiple scattering	28.2	17.4	37.8	24.1

When the differential cross sections obtained from the Yale and LRL phase shift sets (as reported by Hopkins and Breit (Ho72)) were applied to the Monte Carlo calculations, the fit to the experimental spectra improved by approximately 1.2%. But the fit was still not good enough to provide a preference for one or other of the phase shift sets. Figure (9.3a) shows the results. In order to obtain a better understanding of how the experimental spectra were made up, the contributions from single n-p scattering events and different types of multiple scattering events were calculated as shown in Figure (9.3) parts (b) to (f). The major deviations between the experimental and the Monte Carlo spectra occurred in the upper region near channel 375 where the Monte Carlo spectra peaked more sharply than the experimental spectra, and near channel 175 where the Monte Carlo spectra contain a slight hump. The origins of these effects were readily determined from the breakdown of the spectra.

Consider the small scintillator. Part (b) of Figure (9.3) shows the contribution to the spectrum from single n-p scattering events. These account for 35.0% of the events in the scintillator. While single n-C scattering events made up 47.6% of the total number of events, however all these single n-C scattering events produced pulses below the lower level discriminator threshold and so were not regarded as valid events. Table (9.1) gives the breakdown of the occurrence of types of events in each scintillator. The high proportion of multiple scattering events involving carbon nuclei is to be

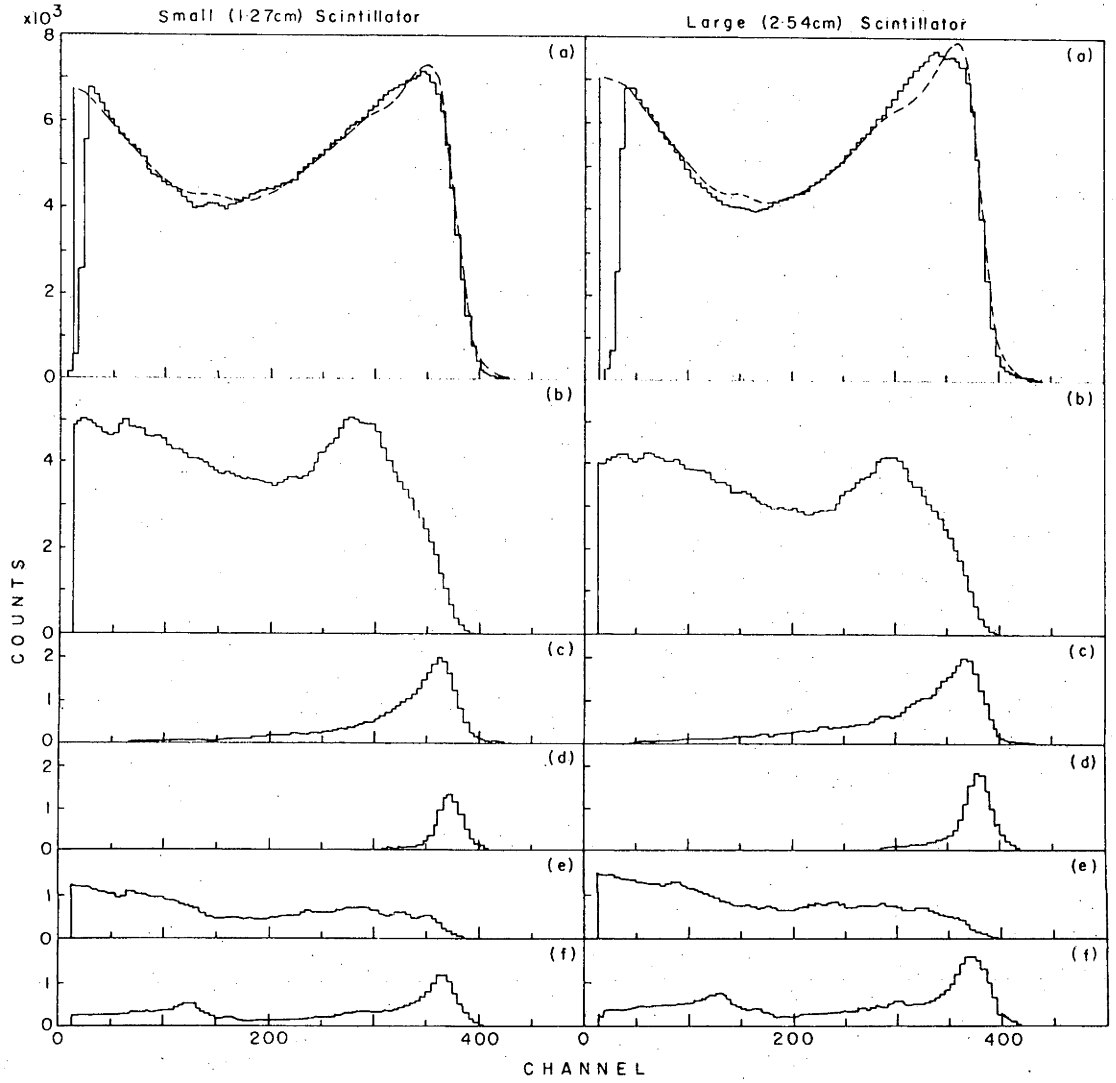

Figure (9.3)

A breakdown of the Monte Carlo spectra for both the large and the small scintillator is shown. Part (a) shows the Monte Carlo spectra (dashed lines) compared to the experimental spectra (solid lines). Parts (b), (c), (d), (e) and (f) show the components due to single n-p scattering, double n-p scattering, triple and higher order n-p scattering, double scattering involving one n-p and one n-C scattering event, and triple and higher order scattering invloving at least one n-p and one n-C scattering event respectively. The Monte Carlo spectra in part (a) has been resolution folded whereas the components in the other parts have not.

expected in view of the large attenuation coefficient for n-C scattering in NE102. A plot of the n-p, n-C(elastic) and n-C(inelastic) attenuation coefficients obtained from the cross section data supplied by Lucas Heights (C177), is shown in Figure (9.4).

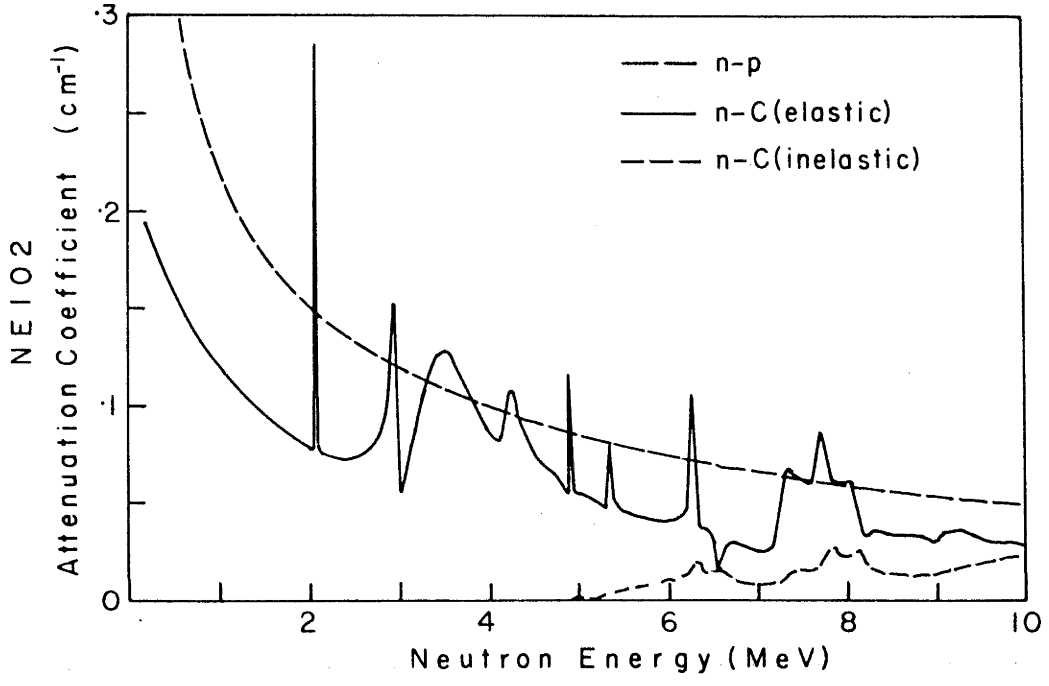

Figure (9.4)
Attenuation coefficients for n-p, n-C(elastic) and n-C(inelastic) scattering for NE102. Of particular interest is that at 8 MeV the total carbon coefficient is 43% larger than the proton coefficient.

Thus, of the vaild events in the small scintillator, 71.8% were single n-p scattering events. The remaining 28.2% was due to multiple scattering comprising: double n-p scattering, 7.5% (part (c) of Figure (9.3)); triple and higher order scattering, 2.2% (part (d)); double scattering

involving one n-p scattering event and one n-C scattering event in either order, 12.5% (part (e)); and triple and higher order scattering involving at least one n-p scattering event and one n-C scattering event, 6.2% (part (f)) [if no n-p scattering event occurrs in the sequence then the total sequence is not recorded due to the light output being below the discriminator threshold].

The spectra in parts (c), (d) and (f) of Figure (9.3) all have peaks in the region of channel 375. Thus it is clearly indicated that the peaking near channel 375 in the total spectrum (part (a)) is due to multiple n-p scattering and multiple scattering involving more than three events one of which must be an n-p scattering event and one of which must be an n-C scattering event. Part (f) of Figure (9.3) also contains a hump in the region of channel 35. This indicates that the hump near channel 35 in the total spectrum is due to multiple scattering events one of which is an n-C(inelastic) scattering and one of which is an n-p scattering event. The energy level in carbon which is populated by such an event has an excitation energy of 4.43 MeV, thus producing a hump approximately 4.43 MeV equivalent neutron energy below the maximum light output.

The time between the first and last event of a multiple scattering sequence can be of the order of a few nanoseconds. The Monte Carlo program takes no account of this, and accordingly the calculated light output for the entire scattering sequence is obtained by linearly adding the light output from each individual scattering event. In the actual experimental situation, this is not necessarily

the case. It would be, if the two light pulses were emitted simultaneously, but in general they are not. It is likely that due to the response time of the scintillator (2.4 ns), the recovery time of the photomultiplier tube and the time constant of the electronics causes the recorded pulse for the total sequence to have a magnitude somewhat less than the maximum value which would be obtained by linear addition of the individual light pulses. The extent to which the recorded event is less than the maximum depends on the time distribution between the individual parts of the multiple scattering sequence.

Another situation which was not taken into account by the Monte Carlo calculations was the 4.43 MeV gamma rays from the $^{12}C(n,n'\gamma)$ reaction. These were produced either by single n-C scattering events or as one of a multiple scattering sequence. In order to reduce the effect of these gamma rays in the experimental spectra, pulse shape analysis was attempted during the data collection. Unfortunately, unlike the NE213 scintillator used in Chapter 8, the NE102 scintillators did not provide sufficient separation of the proton and gamma ray events to be of any use. Therefore it was possible that the experimental spectra could contain events with gamma ray contributions.

Multiple scattering events which involved carbon nuclei produced a further problem in that the n-C differential cross sections cannot be precisely determined. The Monte Carlo program uses tables of cumulative scattering probabilities for given energies and angles (see section (6.4.4c)) and performs a two dimensional interpolation to

Table (9.2)
Summary of the fits obtained using various differential cross sections and corrections.

Result #	1 n-p Scattering Type	2 n-C Isotropic Scattering	3 Light Atten-uation Correction	4 Edge Effect Correction	5 Normalized Fit (%)
Small Scintillator					
1	Isotropic	*			7.16
2	Isotropic				7.Ø3
3	Yale				5.91
4	Yale		*		5.71
5	Yale	*	*	*	5.86
6	Yale		*	*	5.22
7	LRL	*	*		5.85
8	LRL		*		5.72
9	LRL		*	*	5.23
Large Scintillator					
1Ø	Isotropic	*			7.4Ø
11	Isotropic				7.24
12	Yale				5.87
13	Yale		*		5.6Ø
14	Yale	*	*	*	5.85
15	Yale		*	*	5.38
16	LRL	*	*		5.83
17	LRL		*		5.62
18	LRL		*	*	5.36

choose the scattering angle for a given energy. For such an interpolation to provide accurate results the differential cross sections must be smoothly varying between consecutive energy entries in the data tables. This, unfortunately, is not the case for n-C(elastic) differential cross sections as is illustrated by Figure (9.5). The two n-C(elastic) differential cross sections shown are for consecutive energies using the available data. The 7.Ø3 MeV and the .54 MeV differential cross sections are so different that an estimate of what the differential cross section would be at an intermediate energy cannot be legitimately obtained using interpolation. Because of this, a Monte Carlo calculation was performed using isotropic n-C(elastic) scattering. The result of this calculation gave a decrease in the quality of the fit to the experimental spectra.

A summary of the fits obtained in the experimental spectra, using different combinations of differential cross sections and correction routines in the Monte Carlo calculations is given in Table (9.2). Column 1 describes the type of n-p differential cross sections that were used, either isotropic or the Hopkins and Breit predictions from the Yale and LRL phase shift sets. Column 2 shows an asterisk whenever n-C(elastic) scattering was considered to be isotropic instead of using the differential cross sections from the data table. Light attenuation corrections are indicated by an asterisk in column 3 and edge effect corrections by an asterisk in column 4.

The measure of the fit of the Monte Carlo spectra to the experimental spectra was a normalized difference factor,

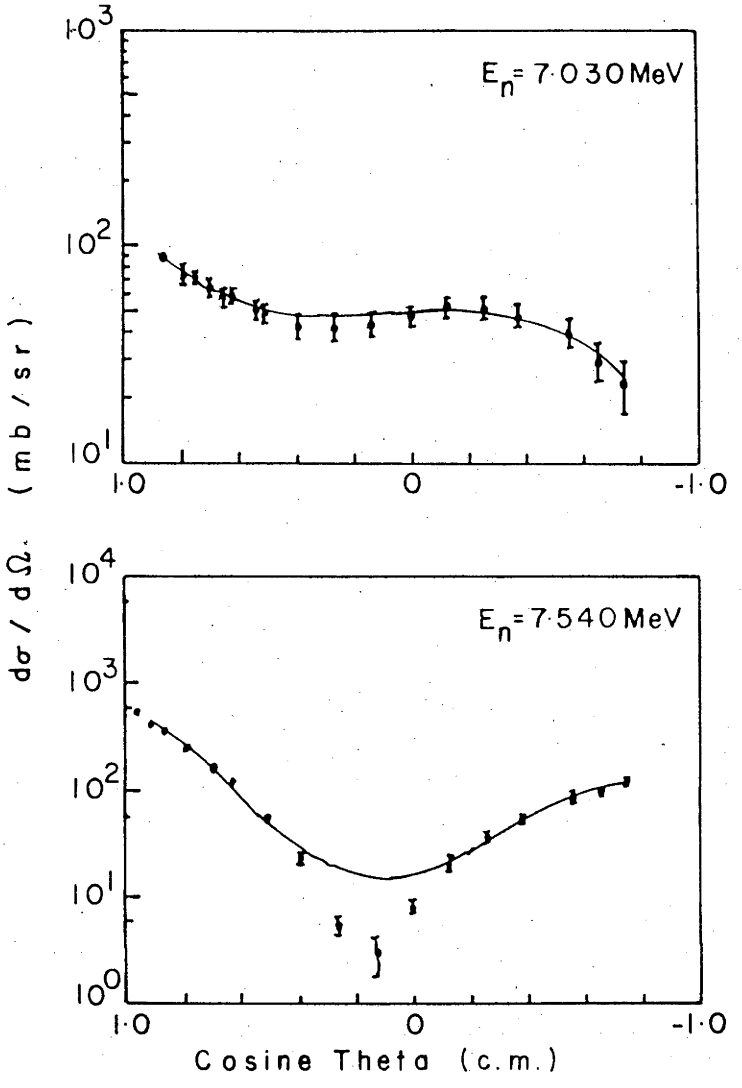

Figure (9.5)
Differential cross sections for n-C(elastic) scattering. The large variation between the two sets of data makes interpolation for an intermediate energy very suspect. (Taken from National Neutron Cross Section Centre publication ref. BNL400.)

given as a percentage, which was defined by

$$F = 100\left[\sum_{i=1}^{n} |a_i - b_i|\right] / \left[\sum_{i=1}^{n} a_i\right] \qquad (9.1)$$

where the sum is over all channels in the spectra

a_i = number of counts in the experimental spectrum

and b_i = number of counts in the Monte Carlo spectrum.

For both scintillators the fit was improved by using differential cross section data for both n-p and n-C scattering as opposed to isotropic scattering. The application of the light attenuation correction provided a slightly better improvement in the large scintillator than it did in the small one. The edge effect correction provided a greater improvement of fit in the smaller scintillator as was to be expected.

In both cases, the Yale differential cross sections gave a slightly better fit to the data than did the LRL differential cross sections. However, the difference is so small that it can not be used to provide support for the Yale phase shift set over the LRL set. What can be concluded is that the use of the differential cross section predictions from the phase shift sets provides a better fit to the experimental data than does isotropic n-p scattering. This is a promising result and indicates that the present work was heading in the right direction. It seems promising that the Monte Carlo technique will become a very useful tool in the future enabling researchers to extract information from their data which would otherwise not be obtainable.

1Ø. CONCLUSION

The associated particle technique using the $D(d,n)^3He$ reaction has proven to be a most satisfactory method of producing a mono-energetic neutron flux. By carefully choosing the kinematic scheme to be used it is possible to optimize the neutron yield while minimizing the energy spread. In choosing the best kinematic scheme for a particular application the $D(d,n)^3He$ differential cross sections need to be considered as they can vary by more than an order of magnitude over the range of neutron production angles.

The present work has accurately measured the $D(d,n)^3He$ angular distributions between 18 and 26 MeV incident deuteron energy. These angular distributions were normalized to earlier data (Di71) at 18 MeV. However, a single data point at 25.3 MeV (Va63) has put some doubt on the accuracy of the absolute value of the 18 MeV data used. Despite this, the relative values of the differential cross sections that were measured in this work are very good as great care was taken to normalize consecutive data sets. Using the results of the present work in conjunction with earlier data at lower energies (Br57, Va63, Th69, Di71), it is now possible to optimize the production of a neutron flux with neutron energies from 2 to 2Ø MeV. This neutron flux has a well defined profile which can be expressed by two Gaussian distributions as was shown in Chapter 3. The beam profile was shown to have a standard deviation of only 1.5° for 8 MeV neutrons.

The $D(d,n)^3He$ differential cross section measurements did not provide any additional support for the proposed 2^+ state near 30 MeV in ^4He (Ta66, We68, To65, Ba66, Me69, Th70, Er70, Er71). This does not disprove the existence of the level as the broard nature of the level may be obscuring its observation and also because the $D(d,n)^3He$ reaction may be a predominantly direct reaction, thus not yielding information about the ^4He system.

The measurement of n-p differential cross sections using the $D(d,n)^3He$ reaction as the neutron source has proved to be a difficult task for two reasons. Firstly, the spread of the neutron beam and the dimensions of the scattering chamber used, combined to necessitate the use of large scintillators as the proton targets. This caused considerable multiple scattering to occur. [The mean free path of 8 MeV neutrons in NE102 is 6.5 cm is comparable to the size of the scintillators used. Ideally the mean free path should be much larger than the dimensions of the scintillator.]

Secondly, the low neutron production rate (approximately 500 per second) meant that using the experimental arrangement, as described in Chapter 8, required an unrealistic data collection time in order to provide the required statistics. The problem could be overcome with the use of a more efficient detection system for the scattered neutrons.

Monte Carlo calculations have proved a valuable asset in the calculation of multiple scattering and edge effect

corrections. They also provided a means of analysing in depth the experimental n-p scattering spectra (Figures (8.8) and (9.3)). Despite the lack of success in getting the Monte Carlo code to exactly reproduce the experimental spectra, it is felt that, with improved n-C angular distributions and more information on the behaviour of the scintillator-photomultiplier collection system with regard to multiple scattering events, the Monte Carlo code could produce a much better fitting spectra.

The present work on n-p scattering was not able to provide a preference for either the Yale or the LRL phase shift sets. It has, however, proved to be a valuable exercise in the combining of experimental and Monte Carlo techniques in the solving of difficult problems.

APPENDIX A

Phase Parameters

This appendix gives a brief description of how phase parameters are introduced into nucleon-nucleon scattering theory. For a fuller treatment of this and other aspects of nucleon-nucleon scattering theory the reader is referred to the reviews by Wolfenstein (Wo56), MacGregor (Ma60) and Nigam (Ni63).

The observables in nucleon-nucleon scattering experiments may be described in terms of the elements of the spin transition matrix (M-matrix). Data in terms of the M-matrix are, in practice, difficult to analyse and so results are usually expressed in terms of phase parameters which are elements of the scattering matrix (S-matrix). A third matrix, the reaction matrix (R-matrix) relates the M and S matrices. The relationships are (Ma60, Ni63)

$$M(k,k') = (4\pi/2ik) \langle \theta\phi | R | \theta'\phi' \rangle \qquad (A.1)$$

$$S = R + 1 \qquad (A.2)$$

where k, (θ, ϕ) and k', (θ', ϕ') are the momenta and directions of the incoming and scattered particles respectively in the centre of mass frame. [The centre of mass frame is used throughout this appendix.]

When the S-matrix is parameterized in such a way that it is unitary, phase parameters may be introduced. Rotational invariance dictates that only the quantum numbers specifying the constants of motion, J and J_Z, can be used to

specify states of a system (Wi63). Odd and even L states do not mix due to parity conservation. It is thus possible to define a unique phase shift set for triplet states with L=J, but, a nondiagonal matrix must be defined so that the L=J±1 states before and after the collision can be related.

The R-matrix can then be represented by a series of 2 X 2 matrices (all other elements vanish) by grouping in pairs the two states L=J±1 for S=1 and the two states S=(1/2)±(1/2) for L=J. Using equation (A.2) the S-matrix must also have this form. Three constants are now required, the phase shifts $\delta_{J+1,J}$ and $\delta_{J-1,J}$ and a coupling parameter ε_J (Ma60,Wi63). These sub-matrices may be written (B152,Ma60):

$$S = \begin{pmatrix} \cos\varepsilon & -\sin\varepsilon \\ \sin\varepsilon & \cos\varepsilon \end{pmatrix} \begin{pmatrix} e^{2i\delta_-} & 0 \\ 0 & e^{2i\delta_+} \end{pmatrix} \begin{pmatrix} \cos\varepsilon & \sin\varepsilon \\ -\sin\varepsilon & \cos\varepsilon \end{pmatrix} \tag{A.3}$$

or (St57,Ma60):

$$S = \begin{pmatrix} e^{i\bar{\delta}_-} & 0 \\ 0 & e^{i\bar{\delta}_+} \end{pmatrix} \begin{pmatrix} \cos 2\bar{\varepsilon} & i\sin 2\bar{\varepsilon} \\ i\sin 2\bar{\varepsilon} & \cos 2\bar{\varepsilon} \end{pmatrix} \begin{pmatrix} e^{i\bar{\delta}_-} & 0 \\ 0 & e^{i\bar{\delta}_+} \end{pmatrix} \tag{A.4}$$

where $\delta_- = \delta_{J-1,J}$ and

$\delta_+ = \delta_{J+1,J}$ are the phase shifts

$J\pm1$ = L is the orbital angular momentum

$\varepsilon = \varepsilon_J$ is the mixing parameter.

The parameters in equation (A.3) are known as the Blatt and Biedenharn phase parameters and those of equation (A.4) as the nuclear bar phase parameters. Another parameterization which has been derived (Ph59) is essentially an extension of equation (A.3).

The mixing parameter gives the proportions in which an incoming beam in one channel (partial wave) divides between the two outgoing channels. It essentially measures the degree to which L is not conserved. Using the Born approximation the phases are given by simple matrix elements of the interaction energy and Coulomb effects can be subtracted to the lowest order by subtracting the Coulomb phases from the total phases (St57). The representation (A.4) is used for most phase parameter analyses. Strapp et al (St57) gives the equations relating the two types of phase parameters.

Experimental parameters can be expressed in terms of the elements of the M-matrix which can be expressed in terms of the elements of the R-matrix. They are thus related to the phase parameters. The relationships between the elements of the different matrices are tabulated in the literature (St57,Ma6Ø).

APPENDIX B

The Monte Carlo Program

The Monte Carlo program described in Chapter 6 is listed on pages B-2 to B-13, with the relevant subroutines listed on pages B-14 to B-25. The version of the program shown is designed to consider a neutron beam incident on the curved surface of a cylindrical scintillator. To alter the program for use with a neutron beam incident on the flat surface of a scintillator the following changes need to be made.

(a) Replace SORCE1 with SORCE2, line 280.

(b) Replace DISTC with DISTB, lines 319 and 504.

(c) Replace line 345 with

```
RADPAR = X(1)*X(1) + X(2)*X(2)
```

and line 349 with

```
IF(X(3).LT.0.0.OR.X(3).GT.D)GO TO 3007
```

The system subroutines required are RAND, DRANF and GRAND. These are all random number generators. RAND and DRANF both produce random numbers uniformly distributed with ranges $0 \leq r < 1$ and $-1 \leq r < 1$ respectively. GRAND produces random numbers according to a Gaussian distribution.

```
      DOUBLE PRECISION WTSUM
      REAL   TITEL,DNAME
      REAL   EPMUS,UMUS,PMUS,QUS
      DIMENSION ABIAS(20)
      DIMENSION EPC(513),ANEP(512),PMID(512),ACTS(512),
     * APULH(513)
      DIMENSION INOCOL(5)
      DIMENSION X(3),U(3),SIGMA(2),TWIDTH(2),UO(3),UR(3)
      DIMENSION EPMUS(9),PMUS(21,9),UMUS(21,9),QUS(21,9)
      DIMENSION TITEL(20),DNAME(10)
      DIMENSION EBIAS(20),NGT(20)
      DIMENSION SPEC1H(512),SPEC2H(512),SPEC3H(512),SPEC1C(512),
     &SPEC2C(512)
      DIMENSION ETAB(600),SCAR(600),SIC(600),SHD(600)
      DIMENSION THETS(21),DHE(25),DDIF(21),DHDIF(25,21),KCARB(5)
      DATA EPMUS/.15,1.5,1.975,3.5,3.65,4.2,4.875,5.6,13.5/
      DATA MURANG/9/
C
C     THE FOLLOWING DATA IS FOR CARBON DIFFERENTIAL CROSS SECTIONS
C     PMUS = P(UMUS)
C
      DATA UMUS/
     &-1.,-.9,-.8,-.7,-.6,-.5,-.4,-.3,-.2,-.1,0.,.1,.2,.3,.4,.5,.6,.7,
     &.8,.9,1.0,
     &-1.,-.92,-.83,-.74,-.65,-.56,-.47,-.38,-.28,-.18,-.08,.02,.12,.22,
     &.33,.44,.55,.66,.77,.88,1.0,
     &-1.,-.9,-.8,-.7,-.6,-.5,-.4,-.3,-.2,-.1,0.,.1,.2,.3,.4,.5,.6,.7,
     &.8,.9,1.0,
     &-1.,-.9,-.8,-.7,-.6,-.5,-.4,-.3,-.2,-.1,0.,.1,.2,.3,.4,.5,.6,.7,
     &.8,.9,1.0,
     &-1.,-.9,-.8,-.7,-.6,-.5,-.4,-.3,-.2,-.1,0.,.1,.2,.3,.4,.5,.6,.7,
     &.8,.9,1.0,
     &-1.,-.9,-.8,-.7,-.6,-.5,-.4,-.3,-.2,-.1,0.,.1,.2,.3,.4,.5,.6,.7,
     &.8,.9,1.0,
     &-1.,-.92,-.83,-.74,-.65,-.56,-.47,-.38,-.28,-.18,-.08,.02,.12,.22,
     &.33,.44,.55,.66,.77,.88,1.0,
     &-1.,-.92,-.83,-.74,-.65,-.56,-.47,-.38,-.28,-.18,-.08,.02,.12,.22,
     &.33,.44,.55,.66,.77,.88,1.0,
     &-1.,-.9,-.8,-.7,-.6,-.5,-.4,-.3,-.2,-.1,0.,.1,.2,.3,.4,.5,.6,.7,
     &.8,.9,1.0/
      DATA  PMUS/
     &21*0.5,
     &.447,.44,.435,.435,.434,.437,.442,.448,.453,.461,.472,.485,.497,
     &.51,.524,.541,.557,.575,.593,.612,.634,
     &.862,.784,.708,.643,.592,.544,.5,.459,.428,.4,.39,.39,.4,.407,
     &.421,.431,.441,.455,.465,.476,.486,
     &1.47,1.22,.972,.767,.576,.406,.267,.157,.0733,.0183,0.,.0131,
     &.0655,.144,.241,.367,.532,.725,.933,1.14,1.37,
     &1.28,1.07,.892,.714,.556,.423,.314,.232,.17,.125,.104,.116,.144,
     &.192,.258,.349,.474,.644,.848,1.09,1.38,
     &1.3,1.03,.812,.642,.516,.414,.336,.278,.236,.209,.19,.18,.175,
     &.178,.197,.246,.357,.564,.856,1.21,1.54,
     &.121,.14,.144,.156,.188,.233,.377,.496,.521,.461,.378,.309,.262,
     &.269,.312,.394,.484,.644,.937,1.46,2.67,
     &.844,.835,.809,.772,.672,.52,.405,.316,.333,.359,.342,.286,.241,
     &.222,.228,.262,.338,.462,.681,.939,1.36,
     &.0981,.0981,.121,.136,.166,.196,.226,.234,.234,.211,.189,.181,.158
     &,.151,.166,.211,.385,.792,1.41,2.51,4.9                    /
```

```
59C
60       IINN=18
61       ACON=0.0
62       ELEVEL=4.433
63       EMIN=1.E-3
64C
65C      READ IN INITIAL VALUES FROM FILE IVALS, LOGICAL UNIT NUMBER 16
66C
67C      DESCRIPTION OF PARAMETERS
68C        IRAN   - RANDOM NUMBER GENERATOR INITIATOR
69C        ITRIG  - CONTROLS WRITING TO A FILE, + TO WRITE
70C        IPRT   - CONTROLS PRINTING OF OUTPUT, + TO PRINT
71C        IBOUND - CONTROLS PROTON RANGE NEAR BOUNDARY, + IF NEEDED
72C        IISO   - CONTROLS ISOTROPIC H SCATTERING, 0 FOR ISOTROPIC
73C        IANAL  - CONTROLS SPECTRUM ANALYSIS, + FOR ANALYSIS
74C        AN     - DETECTOR MEAN PHOTOELECTRONS
75C        ACON   - VARIANCE FOR LIGHT ATTENUATION
76C        DIAM   - DIAMETER OF DETECTOR, IN CENTIMETERS
77C        D      - DEPTH OF DETECTOR, IN CENTIMETERS
78C        ORIEN  - ORIENTATION OF DETECTOR, - FOR INCIDENT ON CURVED FACE
79C        NPS    - NUMBER OF PARTICLES
80C        E      - ENERGY
81C        EMAXP  - NEUTRON ENERGY OF MAXIMUM CHANNEL NUMBER
82C        NCH    - NUMBER OF CHANNELS
83C                 SPECTRUM GOES.
84C        DS     - DISTANCE OF DECTOR FROM SOURCE
85C        SIGMA  - ARRAY OF STANDARD DEVIATIONS OF BEAM PROFILE
86C        TWIDTH - ARRAY GIVING TOTAL WIDTH OF BEAM PROFILE
87C        DEUTEN - INCIDENT DEUTERON ENERGY FOR D(D,N)HE3 REACTION
88C        TSCATA - AVERAGE NEUTRON SCATTERING ANGLE
89C        NBS    - NUMBER OF DIFFERENT BIAS ENERGIES
90C        EBIAS  - BIAS ENERGIES, IN MEV.
91C        TIMAX  - MAXIMUM ALLOWABLE TIME OF FLIGHT
92C        TITEL  - TITEL OF RUN
93C
94   107 FORMAT()
95       READ(16,107)IRAN,ITRIG,IPRT,IBOUND,IISO,IANAL,IFRAC
96       WRITE(3,107)IRAN,ITRIG,IPRT,IBOUND,IISO,IANAL,IFRAC
97       READ(16,107)AN,ACON,DIAM,D
98       WRITE(3,107)AN,ACON,DIAM,D
99       READ(16,107)NPS,E,EMAXP,NCH
100      WRITE(3,107)NPS,E,EMAXP,NCH
101      READ(16,107)DS,SIGMA,TWIDTH,DEUTEN,TSCATA,RFCOEF
102      WRITE(3,107)DS,SIGMA,TWIDTH,DEUTEN,TSCATA,RFCOEF
103      READ(16,107)NBS,(EBIAS(KKLL),KKLL=1,NBS)
104      WRITE(3,107)NBS,(EBIAS(KKLL),KKLL=1,NBS)
105      READ(16,107)TIMAX
106      WRITE(3,107)TIMAX
107C
108C      INITIALIZE KINEMATIC PARAMETERS
109C
110      PI=3.141592654
111      CALL RKINI(DEUTEN,PKIN,ETKIN,AKIN)
112C
113C      FIND THE MAXIMUM RANGE OF RECOIL PROTON
114C
115      ANGLMN=SIGMA(1)*TWIDTH(1)/2.0
116      ENERMX=RKINF(ANGLNM,PKIN,ETKIN,AKIN)
```

```
      RANGM=PRFUN2(ENERMX)
      WRITE(3,207)ENERMX,RANGM
  207 FORMAT(10X,'MAXIMUM ALLOWED NEUTRON ENERGY=',E15.5,/,
     &10X,'MAXIMUM PROTON RECOIL RANGE=',E15.5,' CENTIMETERS')
  227 CONTINUE
C
C     READ IN HYDROGEN DIFF CROSS SECTION DATA
C
      IF(IISO.EQ.0)GO TO 1147
 1007 FORMAT(3E15.5)
 1027 FORMAT(E15.5)
 1047 FORMAT(10A6)
      READ(20,1007)THETS
C     WRITE(3,1007)THETS
      DO 1107 I=1,IISO
      READ(20,1047)DNAME
      DO 1087 J=1,25
      READ(20,1027)DHE(J)
      READ(20,1007)DDIF
      DO 1067 K=1,21
      DHDIF(J,K)=DDIF(K)
 1067 CONTINUE
 1087 CONTINUE
 1107 CONTINUE
      WRITE(3,1047)DNAME
C     DO 1127 J=1,25
C     WRITE(3,1027)DHE(J)
C     WRITE(3,1007)(DHDIF(J,K),K=1,21)
C1127 CONTINUE
 1147 CONTINUE
C
C     INITIALIZE RANDOM NUMBER GENERATOR
C
      RINITL=RAND(IRAN)
C
      RAD=0.5*DIAM
      VOLU=PI*RAD*RAD*D
      SURF=2.0*PI*RAD*RAD+PI*DIAM*D
      TAVSP=EXP(-4.0*VOLU/(SURF*175.0))
      IF(IRES.LT.0) GO TO 1207
      WRITE(3,1167) ACON
      WRITE(3,1187)AN
 1167 FORMAT(/30X,'LIGHT COLLECTION VARIANCE ',E12.3/)
 1187 FORMAT(//30X,'NE102 DETECTOR MEAN PHOTOELECTRONS ',E12.3/)
      GO TO 1247
 1207  CONTINUE
 1227 FORMAT(//30X,'NE102 DETECTOR'/)
 1247 CONTINUE
C
C     PRODUCE THE MACROSCOPIC CROSS SECTIONS FOR ELASTIC HYDROGEN
C     AND CARBON ELASTIC AND INELASTIC.
C
      CALL CROSS(-1.0,ACR,AHYD,ETHRSH,NTAB,ETAB,SCAR,SIC,SHD)
C
C     EVALUATE DET= INTEGRAL FROM -1 TO 1 OF PMUS*D(UMUS) AND
C     QUS= INTEGRAL FORM -1 TO UMUS OF PMUS*D(UMUS)/DET.
C     THEN DIVIDE PMUS BY DET TO NORMALIZE PMUS.
C
```

```
      MU4=MURANG-1
      DO 1287 I=1,MURANG
      QUS(1,I)=0.
      DO 1267 J=2,21
      QUS(J,I)=QUS(J-1,I)+.5*(PMUS(J,I)+PMUS(J-1,I))*(UMUS(J,I)-UMUS(J-1
     &,I))
 1267 CONTINUE
      DET=1./QUS(21,I)
      DO 1287 J=1,21
      QUS(J,I)=DET*QUS(J,   I)
 1287 PMUS(J,I)=DET*PMUS(J,I)
C     WRITE(3,1307)
 1307 FORMAT('1ANGULAR DISTRIBUTIONS FOR CARBON ELASTIC SCATTER')
      DO 1347 I=1,MURANG
C     WRITE(3,1327)EPMUS(I),(UMUS(J,I),PMUS(J,I),QUS(J,I),J=1,21)
 1327 FORMAT('0ENERGY',F6.3,' MEV.'/3X,'MU',6X,'P(MU)',4X,'Q(MU)'/' C. O
     &F M.',11X,'CUMULATIVE'/(F7.3,F9.4,F10.4))
 1347 CONTINUE
C
C     BOOK KEEPING AND INPUT OF THE TITEL.
C
      RSQ=RAD*RAD
      NB2=NBS+NBS
      DO 1367 II=1,NBS
      ABIAS(II)=EBIAS(II)
 1367 CONTINUE
 1387 FORMAT('1'///20X,20A4)
      WRITE(3,1407) DIAM,D
 1407 FORMAT(//10X,'COUNTER PARAMETERS :- DIAMETER ',1PE12.4,' DEPTH',
     * 1PE12.4)
 1427 READ(16,1447)TITEL
      WRITE(3,1387) TITEL
 1447 FORMAT(20A4)
C
C     DETERMINE THE MAXIMUM PULSE HEIGHT AND SCALING OF THE SPECTRUM,
C     AND SET COUNTERS TO 0.
C
 1467 NN=NCH
 1487 CONTINUE
      NNM=NN-1
 1507 ANCH=NCH
 1527 ESTART=E
      PULMAX=SCINA(EMAXP,1.0,D)
      ADIV=PULMAX/ANCH
      APULH(1)=0.0
      DO 1547 II=1,NN
      APULH(II+1)=II*ADIV
      PMID(II)=0.5*(APULH(II)+APULH(II+1))
      ACTS(II)=0.0
 1547 CONTINUE
      ADIV1=EMAXP/ANCH
      EPC(1)=0.0
      DO 1567 II=1,NN
      EPC(II+1)=II*ADIV1
      ANEP(II)=0.0
 1567 CONTINUE
      WRITE(3,1587)
 1587 FORMAT(/10X,60('*'))
```

```
      WRITE(3,1607) NPS,E
 1607 FORMAT(//20X,'TRACKING ',I6,'  NEUTRONS OF ENERGY ',1PE12.4,
     * '  MEV.')
      WRITE(3,1627) NBS,(EBIAS(J),J=1,NBS)
 1627 FORMAT(//10X,I2,' BIAS ENERGIES AT '/(1P10E12.3))
      DO 1647 I=1,NBS
 1647 NGT(I)=0
      DO 1667 II=1,5
 1667 INOCOL(II)=0
      NHYD=0
      NCAR=0
      IHYD=0
      ICAR=0
      ANPP=NPS
      NZERO=0
      MISTOT=0
      NNOCOL=0
      NRECOR=0
      NRECRG=0
      WTSUM=0.0
      NODET=0
      NISCAT=0
      NOSCAT=0
C
C
C     ITERATE FOR NPS NEUTRONS
C
C
      DO 4007 I=1,NPS
      IFIR=0
      IFSCAT=0
      NCOLLS=0
      EDEP=0.0
      DO 2001 KCC=1,5
 2001 KCARB(KCC)=0
      KCARBO=0
      EDEP1H=0.0
      EDEPOH=0.0
      EDEP1C=0.0
      EDEPOC=0.0
      AENG=0.0
      TIME=0.0
      IFST=-1
C
C     CHOOSE INITIAL DIRECTION AND POSITION OF INCIDENT NEUTRON AND
C       DETERMINE THE ENERGY OF THE NEUTRON
C
      CALL SORCE1(RAD,D,DS,SIGMA,TWIDTH,TSCATA,U,X,SIGH,NMISS)
      IF(NMISS.EQ.1)GO TO 2007
      GO TO 2027
 2007 MISTOT=MISTOT+1
      GO TO 4007
 2027 CONTINUE
   11 FORMAT(' CHECK POINT NUMBER',I5)
      ENEW=RKINF(SIGH,PKIN,ETKIN,AKIN)
      E=ENEW
C     WRITE(3,2047)I,E,X,U
 2047 FORMAT(/,' ITERATION NUMBER',I6,'    ENERGY',F7.3,/,
```

```
     1' COORDS',3E10.3,/,' COSINES',3E10.3)
C
C    INTERPOLATE TO GIVE CROSS SECTIONS
C
      ITAB=1
 2067 IF(ETAB(ITAB+1).LE.E) GO TO 2087
      IF(ITAB+1.EQ.NTAB) GO TO 2087
      ITAB=ITAB+1
      GO TO 2067
 2087 ITP=ITAB+1
      FAC1=ETAB(ITAB)-E
      FAC2=E-ETAB(ITP)
      DEN=1.0/(ETAB(ITAB)-ETAB(ITP))
      FAC1=FAC1*DEN
      FAC2=FAC2*DEN
      SHE=FAC1*SHD(ITP)+FAC2*SHD(ITAB)
      SCI=FAC1*SIC(ITP)+FAC2*SIC(ITAB)
      SCE=FAC1*SCAR(ITP)+FAC2*SCAR(ITAB)
      SSCAT=SHE+SCI+SCE
      AINV=1.0/SSCAT
C
C    CHOOSE DISTANCE TO NEXT COLLISION
C
C    FORCED FIRST COLLISION
C
C    FIND THE DISTANCE TO THE BOUNDARY OF THE DETECTOR
C
      IF(IFST.GT.0)GO TO 2147
      DIST=DISTC(X,U,RSQ,D)
      WT=1.0-EXP(-DIST*SSCAT)
C     WRITE(3,2107)DIST,WT
 2107 FORMAT(' DIST',E10.3,'  WT',E10.3)
      WTSUM=WTSUM+WT
 2127 COLDST=-LOG(1.0-RAND(0)*WT)*AINV
      IF(COLDST.GT.DIST)GO TO 2127
      IFST=1
      GO TO 2187
C
C    NORMAL CONSECUTIVE COLLISIONS
C
 2147 DRAN=RAND(0)
      IF(DRAN.LE.0.0)GO TO 2147
 2167 COLDST=-LOG(DRAN)/SSCAT
 2187 CONTINUE
C
C    DETERMINE POSITION OF PROPOSED COLLISION
C
      DO 2207 J=1,3
 2207 X(J)=X(J)+U(J)*COLDST
C     WRITE(3,2227)COLDST,X
 2227 FORMAT('  COLDST',E10.3,'  NEW COORDS',3E10.3)
C
C    TEST TO SEE IF NEW POSITION IS OUTSIDE THE SCATTERER
C
      RADPAR=X(1)*X(1)+X(3)*X(3)
      IF(RADPAR.GE.RSQ)GO TO 3007
      DHAF=D/2.
      DMHAF=-DHAF
```

```
      IF(X(2).LT.DMHAF.OR.X(2).GE.DHAF)GO TO 3007
      TIME=TIME+0.723*COLDST/SQRT(E)
      IF(TIME.GT.TIMAX) GO TO 3007
C
C     DETERMINE TYPE OF COLLISION
C
      RAN=RAND(0)*SSCAT
      IF(RAN.LT.SCI) GO TO 2487
      RAN=RAN-SCI
      IF(RAN.LT.SCE) GO TO 2347
C
C
C   SCATTER IN HYDROGEN
C
C
 2247 APOINT=1.0
      IF(IISO.EQ.0)GO TO 2307
      CALL INTER2(DHE,DHDIF,25,21,E,DDIF)
C     NORMALIZE
      DO 2267 JKL=1,21
 2267 DDIF(JKL)=DDIF(JKL)/DDIF(21)
 2287 C2=RAND(0)
      CO=SQRT(C2)
      IF(CO.LT.THETS(21))GO TO 2287
      CALL INTER(THETS,DDIF,21,CO,PRCO)
      C9=RAND(0)
      IF(C9.GT.PRCO)GO TO 2287
      GO TO 2327
 2307 C2=RAND(0)
      CO=SQRT(C2)
 2327 XMU=CO
      EN=E*C2
      SIN=SQRT(1.0-C2)
      AA=AHYD
      GO TO 2547
C
C   ELASTIC SCATTER FROM CARBON.
C
 2347 CONTINUE
      AA=ACR
      R2=AA*AA
      APOINT=2.0
      IF(E.LE.EPMUS(1)) GO TO 2507
      DO 2367 LR=2,MU4
      IF(EPMUS(LR).GE.E) GO TO 2387
 2367 CONTINUE
 2387 XMU=(EPMUS(LR)-E)/(EPMUS(LR)-EPMUS(LR-1))
      IF( RAND(0).LT.XMU)LR=LR-1
      XMU= RAND(0)
      DO 2407 J=2,20
      IF(QUS(J,LR).GT.XMU) GO TO 2427
 2407 CONTINUE
 2427 BIGX=UMUS(J,LR)-UMUS(J-1,LR)
      BIGC=AMAX1(PMUS(J,LR),PMUS(J-1,LR))
 2447 XLIT=BIGX* RAND(0)
      ETAX=BIGC* RAND(0)
      IF(ETAX.GT.(PMUS(J-1,LR)+XLIT*(PMUS(J,LR)-PMUS(J-1,LR))/BIGX))
     & GO TO 2447
```

```
      XMU=UMUS(J-1,LR)+XLIT
      IF(DABS(XMU).GT.1.0) WRITE(3,2467)
 2467 FORMAT(/20X,'HELP MY COSINES')
      GO TO 2527
 2487 CONTINUE
C
C   INELASTIC SCATTERING FROM CARBON
C
      AA=ACR
      R2=AA*AA*(1.0-ETHRSH/E)
      APOINT=3.0
 2507 CONTINUE
      XMU=DRANF(0)
C
C   ISOTROPIC ELASTIC SCATTERING FROM CARBON
C
 2527 CONTINUE
      R=SQRT(R2)
      DET=1.0+R2+R*(XMU+XMU)
      CO=(1.0+R*XMU)/SQRT(DET)
      SIN=SQRT(1.0-CO*CO)
      EN=E*DET/((AA+1.0)*(AA+1.0))
 2547 CONTINUE
      IF(EN.GT.E) WRITE(3,2567) APOINT,XMU
 2567 FORMAT(/10X,' APOINT AND XMU  ',1P2E12.3)
      EREC=E-EN
      IF(APOINT.GT.2.5) EREC=EREC-ELEVEL
      ESCIN=SCINA(EREC,APOINT,D)
      IF(IFRAC.EQ.0)GO TO 2569
      ESCIN=ESCIN*FRAC(X,RAD,S,PI,TAVSP,RFCOEF,40)
 2569 EDEP=EDEP+ESCIN
      IF(APOINT.GT.1.5)KCARBO=1
      AENG=AENG+E-EN
      F=E
      NCOLLS=NCOLLS+1
      E=EN
C     WRITE(3,2587)E
 2587 FORMAT('  NEW ENERGY',F7.3)
      IF(NCOLLS.GT.5)GO TO 2597
      IF(APOINT.GT.1.5)KCARB(NCOLLS)=1
      IF(APOINT.LT.1.5)KCARB(NCOLLS)=2
 2597 CONTINUE
      IF(IFIR.EQ.0.AND.APOINT.LT.1.5) IHYD=IHYD+1
      IF(IFIR.EQ.0.AND.APOINT.GT.1.5) ICAR=ICAR+1
      IF(APOINT.LT.1.5) NHYD=NHYD+1
      IF(APOINT.GT.1.5) NCAR=NCAR+1
      IFIR=1
      IF(E.LE.EMIN) GO TO 3007
 2607 FORMAT(1X,10E11.3)
      OLDA=U(1)
      OLDB=U(2)
      OLDG=U(3)
      UO(1)=U(1)
      UO(2)=U(2)
      UO(3)=U(3)
C
C   FIND NEW DIRECTION COSINES
C
```

```
      CALL AZIRN(SIA,COA)
      IF(DABS(DABS(U(3))-1.0).GT.1.E-2) GO TO 2627
      U(1)=SIN*COA
      U(2)=SIN*SIA
      U(3)=CO*U(3)/DABS(U(3))
      GO TO 2687
 2627 SQL=SIN/SQRT(1.0-U(3)*U(3))
      ALD=CO*U(1)+SQL*(U(1)*U(3)*COA-U(2)*SIA)
      BETD=CO*U(2)+SQL*(U(2)*U(3)*COA+U(1)*SIA)
      GAMD=CO*U(3)-SQL*COA*(1.0-U(3)*U(3))
      U(1)=ALD
      U(2)=BETD
      U(3)=GAMD
 2687 CONTINUE
      IF(NCOLLS.NE.1.OR.U(3).LT.0.5993.OR.
     &U(3).GT.0.6843)GO TO 2635
      IF(ABS(U(2)).LE.0.05547)IFSCAT=1
 2635 CONTINUE
C
C     PERFORM PROTON RECOIL CORRECTION
C
C     TEST TO SEE IF COLLISION IS WITHIN RECOIL OF BOUNDARY
C
      IF(APOINT.GT.1.5)GO TO 2667
      IF(IBOUND.EQ.0)GO TO 2667
      IF(X(3).LT.RANGM)GO TO 2647
      IF(X(3).GT.D-RANGM)GO TO 2647
      IF(X(1)*X(1)+X(2)*X(2).GT.(RAD-RANGM)**2)GO TO 2647
      GO TO 2667
 2647 CONTINUE
      NRECRG=NRECRG+1
C
C     EVALUATE RANGE OF RECOIL PROTON
C
      RANGE=PRFUN2(EREC)
C
C     FIND DISTANCE TO BOUNDARY OF DETECTOR
C
      SI=RECOIL(XMU,E,EREC)
      CALL DIRECA(U,UO,SI,UR)
      DISTR=DISTC(X,UR,RSQ,D)
      IF(DISTR-RANGE.GE.0.0)GO TO 2667
      DL=RANGE-DISTR
C
C     FIND REMAINING ENERGY AND DECREASE EDEP ACCORDINGLY
C
      EREMAN=38.630*SQRT(DL)-10.650*DL**0.333+2.2551*DL**0.25
      ESCIN1=SCINA(EREMAN,APOINT,D)
      IF(IFRAC.EQ.0)GO TO 2659
      ESCIN1=ESCIN1*FRAC(X,RAD,D,PI,TAVSP,RFCOEF,40)
 2659 EDEP=EDEP-ESCIN1
      NRECOR=NRECOR+1
 2667 CONTINUE
 2707 FORMAT(20X,1P8E12.4)
 2727 IF(ETAB(ITAB+1).LE.E) GO TO 2087
      IF(ITAB+1.EQ.NTAB) GO TO 2087
      ITAB=ITAB+1
      GO TO 2727
```

```
523 3007 CONTINUE
524C
525C   TALLY DEPOSITED ENERGY
526C
527       IF(U(3).LT.0.5993.OR.U(3).GT.0.6843)GO TO 3087
528       IF(ABS(U(2)).GT.0.05547)GO TO 3087
529       NODET=NODET+1
530       IF(IFSCAT.EQ.0)NISCAT=NISCAT+1
531       GO TO 3089
532 3087 IF(IFSCAT.EQ.1)NOSCAT=NOSCAT+1
533       GO TO 4007
534 3089 CONTINUE
535C       WRITE(3,107)KCARB
536       DO 3107 J=1,NBS
537       IF(EDEP.GE.EBIAS(J)) NGT(J)=NGT(J)+1
538 3107 CONTINUE
539       DO 3127 II=1,NN
540       IF(EDEP.GT.APULH(II).AND.EDEP.LE.APULH(II+1)) GO TO 3147
541 3127 CONTINUE
542 3147 ACTS(II)=ACTS(II)+1.0
543       IF(IANAL.EQ.0)GO TO 3164
544       IF(KCARB(1).EQ.2.AND.KCARBO.EQ.0)GO TO 3148
545       IF(KCARB(1).EQ.2.AND.KCARBO.EQ.1.AND.NCOLLS.EQ.2)
546      &SPEC2C(II)=SPEC2C(II)+1.
547       IF(KCARB(2).EQ.2.AND.KCARBO.EQ.1.AND.NCOLLS.EQ.2)
548      &SPEC1C(II)=SPEC1C(II)+1.
549       GO TO 3164
550 3148 CONTINUE
551       IF(NCOLLS.EQ.1)SPEC1H(II)=SPEC1H(II)+1.
552       IF(NCOLLS.EQ.2)SPEC2H(II)=SPEC2H(II)+1.
553       IF(NCOLLS.EQ.3)SPEC3H(II)=SPEC3H(II)+1.
554 3164 CONTINUE
555       DO 3167 II=1,NN
556       IF(AENG.GE.EPC(II).AND.AENG.LT.EPC(II+1)) GO TO 3187
557 3167 CONTINUE
558 3187 ANEP(II)=ANEP(II)+1.0
559       DO 3207 II=1,5
560       IF(NCOLLS.EQ.II) INOCOL(II)=INOCOL(II)+1
561 3207 CONTINUE
562 4007 CONTINUE
563C
564C
565C   ALL TRACKING FINISHED
566C
567C   CALCULATE EFFICENCY
568C
569C      TAKE THE MEAN OF THE WEIGHTING FACTOR
570C
571       ANUMB=NPS
572       WTMEAN=WTSUM/ANUMB
573       ANUMB=WTMEAN/ANUMB
574       WRITE(3,5047)MISTOT
575       WRITE(3,5007)NRECRG
576       WRITE(3,5027)NRECOR
577 5007 FORMAT(/20X,'NUMBER OF PROTONS ENTERING RECOIL CORRECTION',
578      &' VOLUME ',I6)
579 5027 FORMAT(/20X,'NUMBER RECOIL PROTON CORRECTIONS',I6)
580 5047 FORMAT(//20X,'NUMBER OF NEUTRONS THAT MISS SCATTERER ',I6)
```

```
      WRITE(3,5067) NHYD,NCAR,IHYD,ICAR
 5067 FORMAT(//20X,'HYDROGEN COLLISIONS',I6,'  CARBON COLLISIONS',I6/
     *15X,'FIRST HYDROGEN COLLISIONS',I6,'  FIRST CARBON COLLISIONS',I6)
      WRITE(3,5087) (INOCOL(II),II,II=1,5)
 5087 FORMAT(/' THERE ARE ',I6,' PARTICLES HAVING',I2,' COLLISIONS')
      WRITE(3,5097)NODET,NISCAT,NOSCAT
 5097 FORMAT(/,' NUMBER OF NEUTRONS INCIDENT ON DETECTOR=',I6,/,
     &' NUMBER IN-SCATTERED=',I6,/,
     &' NUMBER OUT SCATTERED=',I6)
C
C     PRINT OUTPUT
C
      IF(IPRT.LT.0) GO TO 5207
      IF(IPRT.EQ.2) GO TO 5201
      WRITE(3,5127)
 5127 FORMAT(1H1,20X,'   HISTOGRAM OF DEPOSITED ENERGY')
      WRITE(3,2607) (ANEP(II),II=1,NN)
      WRITE(3,5147)
 5147 FORMAT(1H1,25X,'PULSE HEIGHT BINS')
      WRITE(3,2607) (PMID(II),II=1,NN)
      WRITE(3,5167)
 5167 FORMAT(1H1,25X,'HISTOGRAM OF PULSE HEIGHTS')
      WRITE(3,2607) (ACTS(II),II=1,NN)
      IF(IRES.LT.0) GO TO 5207
 5201 WRITE(3,5167)
      WRITE(3,2607) (ACTS(II),II=1,NN)
      IF(IANAL.EQ.0)GO TO 5207
      WRITE(3,5202)
      WRITE(3,2607)(SPEC1H(II),II=1,NN)
      WRITE(3,5203)
      WRITE(3,2607)(SPEC2H(II),II=1,NN)
      WRITE(3,5204)
      WRITE(3,2607)(SPEC3H(II),II=1,NN)
      WRITE(3,5205)
      WRITE(3,2607)(SPEC1C(II),II=1,NN)
      WRITE(3,5206)
      WRITE(3,2607)(SPEC2C(II),II=1,NN)
 5207 CONTINUE
 5202 FORMAT(1H1,25X,'HISTOGRAM FOR SINGLE HYDROGEN COLLISIONS')
 5203 FORMAT(1H1,25X,'HISTOGRAM FOR DOUBLE HYDROGEN COLLISIONS')
 5204 FORMAT(1H1,25X,'HISTOGRAM FOR TRIPLE HYDROGEN COLLISIONS')
 5205 FORMAT(1H1,25X,'HISTOGRAM FOR H + CARBON COLLISIONS')
 5206 FORMAT(1H1,25X,'HISTOGRAM FOR CARBON + H COLLISIONS')
C
C     WRITE TO A FILE L.U. 18
C
      IF(ITRIG.LT.0)GO TO 5227
      IF(ITRIG.EQ.2)GO TO 5221
      WRITE(18,5127)
      WRITE(18,2607)(ANEP(II),II=1,NN)
      WRITE(18,5147)
      WRITE(18,2607)(PMID(II),II=1,NN)
      WRITE(18,5167)
      WRITE(18,2607)(ACTS(II),II=1,NN)
 5221 CONTINUE
      WRITE(18,5167)
      WRITE(18,2607)(ACTS(II),II=1,NN)
      IF(IANAL.EQ.0)GO TO 5227
```

```
      WRITE(18,5202)
      WRITE(18,2607)(SPEC1H(II),II=1,NN)
      WRITE(18,5203)
      WRITE(18,2607)(SPEC2H(II),II=1,NN)
      WRITE(18,5204)
      WRITE(18,2607)(SPEC3H(II),II=1,NN)
      WRITE(18,5205)
      WRITE(18,2607)(SPEC1C(II),II=1,NN)
      WRITE(18,5206)
      WRITE(18,2607)(SPEC2C(II),II=1,NN)
 5227 CONTINUE
      ZEREF=ANUMB*NPS*100.0
      WRITE(3,5247) ZEREF
 5247 FORMAT(//20X,'ZERO THRESHOLD SINGLE COL. EFFICIENCY =',1PE11.3)
      DO 5307 J=1,NBS
      CALL EFCAL(ACTS,APULH,ANUMB,ABIAS(J),NCH,EFF,DELTA)
      WRITE(3,5287) EBIAS(J),EFF,DELTA
      IF(IRES.LT.0) GO TO 5307
      WRITE(3,5267)
 5267 FORMAT(//30X,'AFTER RESOLUTION FOLDING.'//)
      CALL EFCAL(ACTS,APULH,ANUMB,ABIAS(J),NN,EFF,DELTA)
      WRITE(3,5287) EBIAS(J),EFF,DELTA
 5287 FORMAT(//2X,' FOR BIAS ENERGY ',1PE12.4/9X,'THE COUNTER EFFICIENCY
     * IS ',2PE12.4,' + OR - ',1PE12.4,' PERCENT'//)
 5307 CONTINUE
 5327 CONTINUE
 9999 STOP
      END
```

```
      SUBROUTINE RKINI(T,P,ET,A)
C
C     PURPOSE
C       TO PREPARE CONSTANT TERMS FOR RELATIVISTIC KINEMATIC
C       CALCULATIONS FOR THE D(D,N)HE3 REACTION.
C
C     DEFINITION OF PARAMETERS
C       T       - INCIDENT DEUTERON ENERGY
C       P       - RELATIVISTIC MOMENTUM
C       ET      - TOTAL ENERGY
C       A       - CONSTANT NUMBER ONE
C
      REAL M1,M2,M3,M4
      M1=1876.09
      M2=M1
      M3=939.5493
      M4=2809.366
      Q=3.2684
      E=T+M1
      P=SQRT(E*E-M1*M1)
      ET=T+M1+M2
      A=2.*M2*T+2.*M1*M3+2.*M2*M3+2.*Q*(M1+M2-M3)-Q*Q
      RETURN
      END


      FUNCTION RKINF(SI,P,ET,A)
C
C     PURPOSE
C       TO EVALUATE THE NEUTRON ENERGY FOR A GIVEN SCATTERING
C       ANGLE FOR THE D(D,N)HE3 REACTION.
C
C      DEFINITION OF PARAMETERS
C       SI     - SCATTERING ANGLE IN RADIANS
C       P      - RELAYIVISTIC MOMENTUM
C       ET     - TOTAL ENERGY
C       A      - CONSTANT NUMBER ONE
C
C     SUBROUTINES REQUIRED
C       RKINI - EVALUATES REQUIRED CONSTANTS
C               TO BE CALLED BEFORE RKINF
C
      REAL M3
      CSI=COS(SI)
      M3=939.5493
      B=ET*ET-P*P*CSI*CSI
      ASQR=A*A-4.*M3*M3*B
      RKINF=(ET*A+P*CSI*SQRT(ASQR))*.5/B-M3
      RETURN
      END


      FUNCTION PRFUN2(EP)
C
C     PURPOSE
C       TO EVALUATE THE PROTON RANGE IN NE102 FOR A GIVEN ENERGY.
```

```
59C       THE RANGE IS GIVEN IN CENTIMETERS.
60C
61C     EP - IS THE PROTONS ENERGY IN MEV
62C
63      EPS=EP*EP
64      PRFUN2=1.31365E-3*EP+1.38291E-3*EPS-2.19161E-5*EP*EPS
65      PRFUN2=PRFUN2+3.63879E-7*EPS*EPS
66      PRFUN2=PRFUN2-3.12179E-5/((EP-.79495)**2+0.17141)
67      RETURN
68      END
69
70
71
72      SUBROUTINE CROSS(ACINS,ACR,AHYD,ETHRSH,NTAB,ETAB,SCAR,SIC,SHD)
73C
74C     PURPOSE
75C       TO PRODUCE ARRAYS AF MACROSCOPIC CROSS SECTIONS  OF HYDROGEN
76C       CARBON AND INELASTIC CARBON FOR THE SCINTILLATOR CONCERNED
77C
78C     DESCRIPTION OF PARAMETERS
79C       ACINS  - DETERMINES SCINTILATOR TYPE  - FOR NE102
80C       ACR    - RATIO OF THE ATOMIC MASSES OF CARBON TO A NEUTRON
81C       AHYD   - RATIO OF THE ATOMIC MASSES OF HYDROGEN TO A NEUTRON
82C       ETHRSH - THRESHOLD ENERGY FOR CARBON INELASTIC COLLISIONS
83C       NTAB   - NUMBER OF ENTRIES IN THE ARRAYS
84C       ETAB   - ARRAY OF NEUTRON ENERGIES
85C       SCAR   - ARRAY OF CROSS SECTIONS FOR CARBON ELASTIC
86C       SIC    - ARRAY OF CROSS SECTIONS FOR CARBON INELASTIC
87C       SHD    - ARRAY OF CROSS SECTIONS FOR HYDROGEN ELASTIC
88C
89C     SUBROUTINES AND FUNCTION SUBPROGRAMS REQUIRED
90C       CLAYDAT2 - FILE CONTAINING THE MICROSCOPIC CROSS SECTIONS
91C
92      DIMENSION ETAB(600),SCAR(600),SIC(600),SHD(600)
93      DATA DENS1,RAT1,DENS2,RAT2/1.032,1.105,0.88,1.213/
94C
95C     DENS1 RAT1 FOR NE102... 2 FOR NE213
96C
97      DATA AMH,AMC,AMN/1.00797,12.01115,1.008665/
98      DO 1 I=1,600
99      ETAB(I)=0.0
100     SCAR(I)=0.0
101     SIC(I)=0.0
102     SHD(I)=0.0
103 1   CONTINUE
104C
105C     READ IN THE DATA FILE WHICH HAS BEEN ASSIGNED UNIT NUMBER 15
106C
107   10 FORMAT()
108   11 FORMAT(4(E12.5))
109     READ(15,10)NTAB
110     READ(15,11)(ETAB(I),SCAR(I),SIC(I),SHD(I),I=1,NTAB)
111C
112     IPRINT=-1
113     IF(IPRINT.LT.0)GO TO 22
114     WRITE(3,19) NTAB
115 19  FORMAT(25X,'NUMBER OF POINTS',I8//5X,'ENERGY(MEV)',T27,'C ELAST',
116    *T45,'C INELAST',T67,'H ELAST'//)
```

```
      DO 21 I=1,NTAB
      WRITE(3,20)ETAB(I),SCAR(I),SIC(I),SHD(I)
   20 FORMAT(1X,4(E20.5))
   21 CONTINUE
   22 CONTINUE
C
      ELEVEL=4.433
      ACR=AMC/AMN
      AHYD=AMH/AMN
      ARAT=AMC/AMH
      ETHRSH=ELEVEL*(ACR+1.)/ACR
C
C     CHOOSE WHICH TYPE OF SCINTILLATOR IS BEING USED
C
      IF(ACINS.GT.0.) GO TO 3
      DENS=DENS1
      RAT=RAT1
      GO TO 5
    3 DENS=DENS2
      RAT=RAT2
    5 CONTINUE
      AC=DENS*0.6023/(AMH*(ARAT+RAT))
      AH=AC*RAT
      WRITE(3,4) AH,AC
    4 FORMAT(///20X,'ATOM DENSITIES:- HYDROGEN ',1PE12.4,' CARBON ',
     &1PD12.4)
C
C     PRODUCE MACROSCOPIC CROSS SECTIONS
C
      DO 2 I=1,NTAB
      SCAR(I)=SCAR(I)*AC
      SIC(I)=SIC(I)*AC
      SHD(I)=SHD(I)*AH
    2 CONTINUE
      RETURN
      END


      FUNCTION SCINA(ER,P,D)
C
C     PURPOSE
C       TO EVALUATE THE EQUIVALENT ELECTRON ENERGY FOR A GIVEN
C       PROTON OR CARBON RECOIL IN ONE OF THE THREE SCATTERERS
C       USED.  (NE102)
C
      IF(P.GT.1.5)GO TO 10
      IF(D.LT.2.5)GO TO 8
      IF(D.LT.3.0)GO TO 6
C     TWO INCH SCATTERER
      SCINA=34.11*ER+15.07*EXP(-.5*((ER-5.004)/1.127)**2)
      RETURN
C     ONE INCH SCATTERER
    6 SCINA=48.72*ER+21.03*EXP(-.5*((ER-4.958)/1.139)**2)
      RETURN
C     HALF INCH SCATTERER
    8 SCINA=50.65*ER+25.79*EXP(-.5*((ER-4.712)/1.149)**2)
      RETURN
```

```
C     CARBON SCATTER
10    SCINA=0.14*ER
      RETURN
      END


      SUBROUTINE SORCE1(RO,HO,DS,SIGMA,TWIDTH,TSCATA,U,X,SIGH,NMISS)
C
C     PURPOSE
C       TO PRODUCE A SET OF DIRECTION COSINES AND INTERCEPT COORDINATES
C       FOR A POINT SOURCE OF NEUTRONS INCIDENT ON THE CURVED SURFACE
C       OF A CYLINDRICAL SCINTILLATOR.  THE BEAM PROFILE IS CONTROLED
C       BY TWO GAUSSIANS , ONE IN THE Y-Z PLANE (SUBSCRIPT 1) AND ONE
C       IN THE X-Z PLANE (SUBSCRIPT 2).  THE BEAM IS CENTRED ABOUT
C       THE Z AXIS.
C       THE ORIGIN IS LOCATED IN THE CENTRE OF THE CYLINDER
C       OF THE SCINTILLATOR.
C
C     DESCRIPTION OF PARAMETERS
C       RO      - RADIUS OF CYLINDER
C       HO      - HEIGHT OF CYLINDER
C       DS      - DISTANCE BETWEEN SOURCE AND CYLINDER CENTRE
C       SIGMA   - ARRAY OF STANDARD DEVIATIONS FOR BEAM PROFILE
C       TWIDTH  - ARRAY GIVING TOTAL WIDTH OF BEAM PROFILES
C       TSCATA  - MEAN NEUTRON PRODUCTION ANGLE
C       U       - ARRAY OF DIRECTION COSINES
C       X       - ARRAY OF POSITION COORDINATES
C       SIGH    - INDIVIDUAL NEUTRON PRODUCTION ANGLE
C       NMISS   - COUNTER FOR NUMBER OF PARTICLES THAT MISS CYLINDER
C
C     SUBROUTINES AND FUNCTION SUBPROGRAMS REQUIRED
C       RGAUS2 - PRODUCES RANDOM NUMBERS ACCORDING TO A GAUSSIAN
C
      DIMENSION SIGMA(2),TWIDTH(2),U(3),X(3)
      NMISS=0
C
C     CHOOSE THE INITIAL ANGLES SI AND THETA
C     SI IS THE ANGLE BETWEEN THE Z AXIS AND THE Y-Z PLANE PROJECTION
C     THETA IS THE ANGLE BETWEEN THE Y-Z PLANE AND THE DIRECTION
C
10    SI=RGAUS2(SIGMA(1),TWIDTH(1))
      THETA=RGAUS2(SIGMA(2),TWIDTH(2))
C
C     EVALUATE THE DIRECTION COSINES
C
      CSI=COS(SI)
      CTHETA=COS(THETA)
      SSI=SIN(SI)
      STHETA=SIN(THETA)
      CSI2=CSI*CSI
      CTHET2=CTHETA*CTHETA
      SSI2=SSI*SSI
      STHET2=STHETA*STHETA
      TM=SQRT(SSI2+STHET2+CSI2*CTHET2)
      U(1)=SSI/TM
      U(2)=STHETA/TM
      U(3)=CSI*CTHETA/TM
```

```
      SIGH=ACOS(COS(TSCATA+SI)*CTHETA)
C
C     EVALUATE WHERE PARTICLE MEETS SCATTERER
C
      A=SSI2+CSI2*CTHET2
      B=2.*(DS+RO)*SSI2
      C=(DS+RO)*(DS+RO)*SSI2-RO*RO*CTHET2*CSI2
      SRF=B*B-4.*A*C
      IF(SRF.LT.0.0)GO TO 20
      X(3)=(-B-SQRT(SRF))/(2.*A)
      X(1)=(X(3)+DS+RO)*SSI/(CSI*CTHETA)
      X(2)=(X(3)+DS+RO)*STHETA/(CSI*CTHETA)
      RETURN
   20 NMISS=NMISS+1
      GO TO 10
      END


      SUBROUTINE SORCE2(RO,HO,DS,SIGMA,TWIDTH,TSCATA,U,X,SIGH,NMISS)
C
C     PURPOSE
C       TO PRODUCE A SET OF DIRECTION COSINES AND INTERCEPT COORDINATES
C       FOR A POINT SOURCE OF NEUTRONS INCIDENT ON THE FLAT SURFACE
C       OF A CYLINDRICAL SCINTILLATOR.  THE BEAM PROFILE IS CONTROLED
C       BY TWO GAUSSIANS , ONE IN THE Y-Z PLANE (SUBSCRIPT 1) AND ONE
C       IN THE X-Z PLANE (SUBSCRIPT 2).  THE BEAM IS CENTRED ABOUT
C       THE Z AXIS.  WITH THE ORIGIN OF THE SET OF AXIS LOCATED IN THE
C       CENTER OF THE INCIDENT FACE OF THE CYLINDER.
C
C     DESCRIPTION OF PARAMETERS
C       RO     - RADIUS OF CYLINDER
C       HO     - HEIGHT OF CYLINDER
C       DS     - DISTANCE BETWEEN SOURCE AND CYLINDER CENTRE
C       SIGMA  - ARRAY OF STANDARD DEVIATIONS FOR BEAM PROFILE
C       TWIDTH - ARRAY GIVING TOTAL WIDTH OF BEAM PROFILES
C       TSCATA - MEAN NEUTRON PRODUCTION ANGLE
C       U      - ARRAY OF DIRECTION COSINES
C       X      - ARRAY OF POSITION COORDINATES
C       NMISS  - COUNTER FOR NUMBER OF PARTICLES THAT MISS CYLINDER
C       SI     - ANGLE BETWEEN Z-X PLANE AND NEUTRON DIRECTION
C
C     SUBROUTINES AND FUNCTION SUBPROGRAMS REQUIRED
C       RGAUS2 - PRODUCES RANDOM NUMBERS ACCORDING TO A GAUSSIAN
C
      DIMENSION SIGMA(2),TWIDTH(2),U(3),X(3)
      PI=3.141592654
      HAFPI=PI/2.
      NMISS=0
C
C     CHOOSE THE INITIAL ANGLES SI AND THETA
C     SI IS THE ANGLE BETWEEN THE Z AXIS AND THE Y-Z PLANE PROJECTION
C     THETA IS THE ANGLE BETWEEN THE Y-Z PLANE AND THE DIRECTION
C
   10 SI=RGAUS2(SIGMA(1),TWIDTH(1))
      THETA=RGAUS2(SIGMA(2),TWIDTH(2))
      SIGH=SI
C
```

```
C     EVALUATE THE DIRECTION COSINES
C
      CSI=COS(SI)
      CTHETA=COS(THETA)
      U(1)=COS(HAFPI-THETA)
      U(2)=CTHETA*COS(HAFPI-SI)
      U(3)=CTHETA*CSI
      SIGH=ACOS(COS(TSCATA+SI)*CTHETA)
C
C     EVALUATE WHERE PARTICLE MEETS SCATTERER
C
      X(1)=DS*TAN(THETA)
      X(2)=DS*TAN(SI)
      X(3)=0.0
      RS=X(1)**2+X(2)**2
      IF(RO**2-RS)20,20,30
   20 NMISS=1
   30 RETURN
      END


      FUNCTION RGAUS2(SIGMA,TWIDTH)
C
C     PURPOSE
C       TO PRODUCE RANDOM NUMBERS THAT ARE DISTRIBUTED ACCORDING
C       TO A GAUSSIAN DISTRIBUTION WITH A SPECIFIED STANDARD DEVIATION
C       CENTERED ON ZERO.  THE DISTRIBUTION HAS A FINITE WIDTH
C
C     DESCRIPTION OF PARAMETERS
C       SIGMA  - STANDARD DEVIATION OF THE DISTRIBUTION
C       TWIDTH - TOTAL WIDTH TO BE CONSIDERED. (IN UNITS OF SIGMA)
C
C     SUBROUTINES AND FUNCTION SUBPROGRAMS REQUIRED
C
C       GRAND - PRODUCES RANDOM NUMBERS ACCORDING TO A NORMAL DISTRIBUTI
C
   10 RGAUS2=GRAND(0)
      RGAUS2=RGAUS2*SIGMA
      IF(DABS(RGAUS2).GE.SIGMA*TWIDTH/2.D0)GO TO 10
   20 RETURN
      END


      FUNCTION DISTB(X,U,RSQ,D)
C
C     PURPOSE
C       TO EVALUATE THE DISTANCE FROM A POINT WITHIN A CYLINDER
C       TO THE BOUNDARY IN A SPECIFIED DIRECTION
C       THE Z AXIS IS PARALLEL TO THE AXIS OF THE CYLINDER
C
C     DESCRIPTION OF PARAMETERS
C       X      - ARRAY OF POSITION COORDINATES
C       U      - ARRAY OF DIRECTION COSINES
C       RSQ    - RADIUS SQUARED
C       D      - DEPTH OF CYLINDER
C
```

```
      DIMENSION X(3),U(3)
      IF(ABS(U(3)).LT.1.)GO TO 30
C
C     EVALUTE DISTANCE TO THE Z BOUNDARY
C
   20 ZBND=0.
      IF(U(3).GT.0.)ZBND=D
      AK=(ZBND-X(3))/U(3)
C
C      TEST TO SEE IF Z BOUNDARY IS INSIDE CYLINDER
C
      XY=(X(1)+AK*U(1))**2+(X(2)+AK*U(2))**2
      IF(XY.LE.RSQ)GO TO 40
C
C     SOLVE FOR CYLINDRICAL SURFACE USING QUADRATIC FORMULA
C
   30 AB=X(1)*U(1)+X(2)*U(2)
      AC=1.-U(3)*U(3)
      AK=(-AB+SQRT(AB*AB+AC*(RSQ-X(1)*X(1)-X(2)*X(2))))/AC
C
C      TEST TO SEE IF Z BOUNDARY INSIDE CYLINDER
C
      ZN=X(3)+U(3)*AK
      IF(ZN.LT.0.0.OR.ZN.GT.D)GO TO 20
   40 DISTB=AK
      RETURN
      END


      FUNCTION DISTC(X,U,RSQ,D)
C
C     PURPOSE
C       TO EVALUATE THE DISTANCE FROM A POINT WITHIN A CYLINDER
C       TO THE BOUNDARY IN A SPECIFIED DIRECTION
C
C     DESCRIPTION OF PARAMETERS
C       X       - ARRAY OF POSITION COORDINATES
C       U       - ARRAY OF DIRECTION COSINES
C       RSQ     - RADIUS SQUARED
C       D       - DEPTH OF CYLINDER
C
      DIMENSION X(3),U(3)
      HD=D/2.
      HDM=-HD
      IF(ABS(U(2)).LT.1.E-2)GO TO 30
C
C     EVALUTE DISTANCE TO THE Y BOUNDARY
C
   20 ZBND=HDM
      IF(U(2).GT.0.D0)ZBND=HD
      AK=(ZBND-X(2))/U(2)
C
C      TEST TO SEE IF Z BOUNDARY IS INSIDE CYLINDER
C
      XY=(X(3)+AK*U(3))**2+(X(1)+AK*U(1))**2
      IF(XY.LE.RSQ)GO TO 40
C
```

```
C     SOLVE FOR CYLINDRICAL SURFACE USING QUADRATIC FORMULA
C
   30 AB=X(3)*U(3)+X(1)*U(1)
      AC=1.-U(2)*U(2)
      SQARG=AB*AB + AC*(RSQ-X(3)*X(3)-X(1)*X(1))
      IF(SQARG.LE.0.0)WRITE(3,10)SQARG,X,U,AB,AC,RSQ
   10 FORMAT(1X,6E15.5,/,1X,4E15.5)
      AK=(-AB+SQRT(SQARG))/AC
C
C      TEST TO SEE IF Z BOUNDARY INSIDE CYLINDER
C
      ZN=X(2)+U(2)*AK
      IF(ZN.LT.HDM.OR.ZN.GT.HD)GO TO 20
   40 DISTC=AK
      RETURN
      END



      SUBROUTINE INTER2(X,Y,NPTS,NUM,XIN,YOUT)
C     PURPOSE
C       PERFORM A LINEAR INTERPOLATION OF AN ARRAY OF DATA POINTS
C
C     DESCRIPTION OF PARRAMETERS
C       X       - ARRAY OF INDEPENDENT DATA POINTS
C       Y       - ARRAY OF DEPENDENT DATA POINTS
C       NPTS    - NUMBER OF DATA POINTS
C       XIN     - INPUT VALUE OF INDEPENDENT DATA
C       YOUT    - OUTPUT OF INTERPOLATED VALUE
C
      DIMENSION X(1),Y(25,21),YOUT(1)
   11 DO 19 I=1,NPTS
      IF(XIN-X(I))13,17,19
   13 I1=I-1
      IF(I1)15,15,31
   15 I1=1
      GO TO 31
   17 DO 18 J=1,NUM
      YOUT(J)=Y(I,J)
   18 CONTINUE
      GO TO 61
   19 CONTINUE
C
   31 DENOM=X(I1+1)-X(I1)
      DELTA=(XIN-X(I1))/DENOM
C
      DO 42 J=1,NUM
   40 A=Y(I1,J)
      B=Y(I1+1,J)-A
      YOUT(J)=A+B*DELTA
   42 CONTINUE
   61 RETURN
      END



      SUBROUTINE INTER(X,Y,NPTS,XIN,YOUT)
C     PURPOSE
```

```
C       PERFORM A LINEAR INTERPOLATION OF AN ARRAY OF DATA POINTS
C
C     DESCRIPTION OF PARRAMETERS
C       X       - ARRAY OF INDEPENDENT DATA POINTS
C       Y       - ARRAY OF DEPENDENT DATA POINTS
C       NPTS    - NUMBER OF DATA POINTS
C       XIN     - INPUT VALUE OF INDEPENDENT DATA
C       YOUT    - OUTPUT OF INTERPOLATED VALUE
C
      DIMENSION X(1),Y(1)
   11 DO 19 I=1,NPTS
      IF(XIN-X(I))13,17,19
   13 I1=I-1
      IF(I1)15,15,31
   15 I1=1
      GO TO 31
   17 YOUT=Y(I)
      GO TO 61
   19 CONTINUE
C
   31 DENOM=X(I1+1)-X(I1)
      DELTA=(XIN-X(I1))/DENOM
C
   40 A=Y(I1)
      B=Y(I1+1)-A
      YOUT=A+B*DELTA
   61 RETURN
      END



      FUNCTION FRAC(X,RAD,D,PI,TAVSP,R,NUM)
      DIMENSION X(3)
      S=FSA(X,RAD,D,PI,NUM)
      FRAC=S*TAVSP/(1.0-R*TAVSP*(1.0-S))
      RETURN
      END



      FUNCTION FSA(X,RAD,D,PI,NUM)
C     PURPOSE
C       TO EVALUATE THE FRACTION OF THE TOTAL SOLID ANGLE THAT
C       THE BASE OF A CYLINDER SUBTENDS TO ANY POINT WITHIN THE
C       CYLINDER.  THE ORIGIN OF THE COORDINATE SYSTEM IS IN THE
C       CENTRE OF THE TOP OF THE CYLINDER, THE Z (X(3)) AXIS
C       BEING THE AXIS OF THE CYLINDER.
C
C     PARAMETERS
C       X       -COORDINATES OF THE POINT
C       RAD     -RADIUS OF THE CYLINDER
C       D       -DEPTH OF THE CYLINDER
C       PI      -PI
C       NUM     -THE NUMBER OF STEPS IN THE INTEGRATION
C
      DIMENSION X(3),P(50),Y(50)
      IF(X(3).GE.D)GO TO 50
      ZDASH=D-X(3)
```

```
      XDASHS=X(1)*X(1)+X(2)*X(2)
      XDASH=SQRT(XDASHS)
      IF(XDASH.GE.RAD)GO TO 60
      DI=SQRT(XDASHS+ZDASH*ZDASH)
      BETA=ATAN(XDASH/ZDASH)
      CBETA=COS(BETA)
      SBETA=SIN(BETA)
      OA=DI*SBETA
      AP=DI*CBETA
      SI1=BETA+ATAN((RAD-OA)/AP)
      SI2=BETA-ATAN((RAD+OA)/AP)
      NUMM1=NUM-1
      DSI=(SI1-SI2)/FLOAT(NUMM1)
      P(1)=SI1
      DO 10 I=2,NUMM1
   10 P(I)=SI1-FLOAT(I-1)*DSI
      P(NUM)=SI2
      Y(1)=0.
      DO 20 I=2,NUMM1
      AR=RAD*RAD-(OA+AP*ATAN(P(I)-BETA))**2
   20 Y(I)=SIN(P(I))*ATAN(SQRT(AR)/AP*COS(P(I)-BETA))
      Y(NUM)=0.
      AREA=0.
      AREA=AREA+(ABS(Y(2))+ABS(Y(NUM-1)))*31./24.
      AREA=AREA+(ABS(Y(3))+ABS(Y(NUM-2)))*5./6.
      AREA=AREA+(ABS(Y(4))+ABS(Y(NUM-3)))*25./24.
      NUMM4=NUM-4
      DO 30 I=5,NUMM4
C     DO 30 I=2,NUMM1
   30 AREA=AREA+ABS(Y(I))
      AREA=AREA*DSI*2.
      FSA=AREA/(4.*PI)
      RETURN
   50 FSA=.5
      RETURN
   60 FSA=0.
      RETURN
      END



      SUBROUTINE AZIRN(SIA,COA)
C
C     PURPOSE
C       TO PRODUCE THE SINE AND COSINE OF RANDOMLY DISTRIBUTED
C       AZIMUTHAL ANGLES
C
      PI=3.141592654
      TWOPI=2.*PI
      R=RAND(0)
      SIA=SIN(R*TWOPI)
      COA=COS(R*TWOPI)
      RETURN
      END



      FUNCTION RECOIL(XMU,E,EREC)
```

```
C
C     PURPOSE
C       TO EVALUATE THE ANGLE BETWEEN THE TRAJECTORIES OF THE
C       INCIDENT NUCLEUS AND THE RECOIL NUCLEUS.
C
C     DESCRIPTION OF PARAMETERS
C       AMP     - REST MASS OF A PROTON
C       AMN     - REST MASS OF A NEUTRON
C       XMU     - COSINE OF THE SCATTERING ANGLE
C       E       - ENERGY OF SCATTERED NEUTRON
C       EREC    - ENERGY OF RECOILING PROTON
C
      AMP=1.007276470
      AMN=1.008665012
      SI=ACOS(XMU)
      RAT=SQRT(AMN*E/(AMP*EREC))
      ETA=RAT*SIN(SI)
      IF(ETA.GT.1.)ETA=1.0
      RECOIL=ASIN(ETA)
      RETURN
      END


      SUBROUTINE DIRECA(U,UO,SI,UR)
C
C     PURPOSE
C       TO EVALUATE THE DIRECTION COSINES OF A RECOIL PROTON
C
C     DESCRIPTION OF PARAMETERS
C       U  - DIRECTION COSINES OF SCATTERED NEUTRON
C       UO - DIRECTION COSINES OF INCIDENT NEUTRON
C       SI - RECOIL OF PROTON
C       UR - DIRECTION COSINES OF RECOIL PROTON
C
      DIMENSION U(3),UO(3),UR(3)
C
C     EVALUATE THE POLAR COORDINATES OF THE DIRECTION COSINES
C
      PI=3.141592654
      PIDTO=PI/2.
      BINC=PIDTO-ACOS(UO(1))
      AINC=ACOS(UO(3)/COS(BINC))
      BSCAT=PIDTO-ACOS(U(1))
      ASCAT=ACOS(U(3)/COS(BSCAT))
      ASIGN=1.
      BSIGN=1.
      ADIFF=ASCAT-AINC
      BDIFF=BSCAT-BINC
      IF(ADIFF.GT.0.)ASIGN=-1.
      IF(BDIFF.GT.0.)BSIGN=-1.
      EPS=1.E-6
      IF(ABS(ADIFF).LT.EPS)GO TO 10
      GO TO 30
C
C     SPECIAL CASE OF SCATTERING IN THE B PLANE
C
   10 ARCOIL=AINC
```

```
      BRCOIL=BINC+BSIGN*SI
      GO TO 40
C
C     GENERAL CASE
C
   30 CONTINUE
      R=TAN(BDIFF)/SIN(ADIFF)
      RSQ=R*R
      C=COS(SI)
      CSQ=C*C
      B=ACOS(SQRT((1.+RSQ*CSQ)/(RSQ+1.)))
      A=ACOS(C/COS(B))
      ARCOIL=AINC+ASIGN*A
      BRCOIL=BINC+BSIGN*B
C
C     EVALUATE DIRECTION COSINES
C
   40 CONTINUE
      UR(1)=COS(PIDTO-BRCOIL)
      UR(2)=COS(BRCOIL)*COS(PIDTO-ARCOIL)
      UR(3)=COS(BRCOIL)*COS(ARCOIL)
      RETURN
      END


      SUBROUTINE EFCAL(A,P,WT,BIAS,N,EFF,DELTA)
      DIMENSION A(1),P(1)
C   WT = (1-EXP(-SIGMA*D))/NO. OF INCIDENT PARTICLES
      DO 1 I=1,N
      IF(BIAS.GE.P(I).AND.BIAS.LT.P(I+1)) GO TO 2
    1 CONTINUE
      EFF=0.
      DELTA=0.
      RETURN
    2 IMN=I+1
      FRAC=(P(IMN)-BIAS)/(P(IMN)-P(I))
      SUM=FRAC*A(I)
      IF(IMN.GE.N) GO TO 4
      DO 3 I=IMN,N
      SUM=SUM+A(I)
    3 CONTINUE
    4 EFF=SUM*WT*100.
      DELTA=SQRT(SUM)*WT*100.
      RETURN
      END
```

REFERENCES

Ar66 R.A. Arndt and M.H. MacGregor, Phys. Rev., 141 (1966) 873.

Ar67 R.A. Arndt and M.H. MacGregor, Phys. Rev., 154 (1967) 1549.

Ba61 R. Batchelor, W.B. Gilboy, J.B. Parker and J.H. Towle, Nucl. Instr. and Meth. 13 (1961) 7Ø.

Ba63 R. Batchelor and J.H. Towle, Nucl. Phys. 47 (1963) 385.

Ba64 C.J. Batty and J.K. Perring, Nucl. Phys., 59 (1964) 141.

Ba66 B.R. Barrett, W.E. Meyerhof and J.D. Walecka, Phys. Lett., 22 (1966) 45Ø.

Ba74 C.M. Bartle and P.A. Quin, Nucl. Instr. and Meth., 121 (1974) 119.

Ba75 C. M. Bartle, NBS-SP-425 (1975) Vol. I, 688.

Ba77 C.M. Bartle, Nucl. Instr. and Meth., 144 (1977) 599

Ba77a C.M. Bartle, D.W. Gebbie and C.L. Hollas, Australian National University internal report AUN-P/675, Nucl. Instr. and Meth., 144 (1977) 437

Be49 H. Bethe, Phys. Rev., 76 (1949) 38.

Be76 F.D. Becchetti, C.E. Thorn and M.J. Levine, Nucl. Instr. and Meth., 138 (1976) 93.

Bo61 B. Bosco, Phys. Rev., 123 (1961) 1Ø72.

Bi51 J.B. Birks, Proc. Phys. Soc., A164 (1951) 1Ø.

Bi64 J.B. Birks,"The Theory and Practice of Scintillation Counting", MacMillan, New York, 1964.

Bi68 S.I. Bilen'kaya, J. Bystricky, Z Janout, Yu. M.

Kazarinov, F. Lehar and A. Pazma, Joint Insti. for Nucl. Research (Dubna) Report, EI-3899 (1968)

Bl52 J.M. Blatt and L.C. Biedenharn, Phys. Rev., 86 (1952) 399, and Rev. Mod. Phys., 24 (1952) 258.

Br36 G. Breit, E.U. Condon and R.D. Present, Phys. Rev., 5Ø (1936) 825.

Br49 G. Breit and W.C. Bouricius, Phys. Rev., 79 (1949) 1Ø29.

Br57 J.E. Brolley Jr., T.M. Putman and L. Rosen, Phys. Rev., 1Ø7 (1957) 82Ø.

Br58 K.A. Brueckner, J.L. Gammel and R.M. Thaler, Phys. Rev., 1Ø9 (1958) 1Ø23.

Br6Ø R.A. Bryan, Bull. Am. Phys. Soc., 5 (196Ø) 35.

Br6Øa G. Breit, M.H. Hull Jr., K.E. Lassila and K.D. Pyatt Jr., Phys. Rev., 12Ø (196Ø) 2227.

Br6Øb R.A. Bryan, Bull. Am. Phys. Soc., 5 (196Ø) 35.

Br6Øc G. Breit, M.H. Hull, Jr., K.E. Lassila and K.D. Pyatt, Jr., Phys. Rev., 12Ø (196Ø) 2227.

Br63 R.A. Bryan, C.R. Dismukes and W. Ramsay, Nucl. Phys., 45 (1963) 353.

Br67 G. Breit, Rev. Mod. Phys., 39 (1967) 56Ø.

Br68 G. Breit and R.E. Seamon, Phys. Rev. Lett., 21 (1968) 76Ø.

Br68a G. Breit, K.A. Friedman, J.M. Holt and R.E. Seamon, Phys. Rev., 17Ø (1968) 624.

Br69 C.N. Bressel, A.K. Kerman and B. Rouben, Nucl. Phys., A124 (1969) 624.

Br69a G. Breit, J. Lucas and M. Tischler, Phys Rev., 184 (1969) 1668.

Br70 D.M. Brink, "Theory of Nuclear Structure": Triests Lectures, 1969 (IAEA, 1970) page 3.

Br79 F.D. Brooks, Nucl. Instr. and Meth., 162 (1979)447.

Bu72 T.W. Burrows, Phys Rev. C, 7 (1972) 1306.

Ca59 E.D. Cashwell and C.J. Everett, "A Practicle Manual on the Monte Carlo Method for Random Walk Problems" , Pergamon Press, 1959.

Ca76 R. Casparis, B.Th. Leemann, M. Preiswerk, H. Rubin, R. Wagner and P. Zupranski, Nucl. Phys. A263 (1976) 285.

Ch32 J. Chadwick, Proc. Roy. Soc., A 136 (1932) 692.

Ch52 C.N. Chou, Phys. Rev., 87 (1952) 904.

Ch73 G.C. Chikkur and N. Umakantha, Nucl. Instr. and Meth., 107 (1973) 201.

Cl60 G.W. Clark, IRE Trans. Nucl. Sci. NS-7 (1960) 82.

Cl77 E. Clayton, Lucas Heights Research Establishment, private communication.

Cr70 R.L. Craun and D.L. Smith, Nucl. Instr. and Meth. 80 (1970) 239.

Cz59 P. Cziffra, M.H. MacGregor, M.J. Moravcsik and H.P. Stapp, Phys. Rev., 114 (1959) 880.

De74 R. DeLeo, G. D'Erasmo, A. Pantaleo and G. Russo, Nucl. Instr. and Meth. 119 (1974) 559.

Di72 F.S. Dietrich, E.G. Adelberger and W.E. Meyerhof, Nucl. Phys., A184 (1972) 449.

Ei41 L. Eisenbub and E. Wigner, Proc. Nat. Acad. Sci. U.S.A., 27 (1941) 281.

En63 C.E. Engelke, R.E. Benenson, E. Melkonian and J.M. Lebowitz, Phys. Rev., 129 (1963) 324.

En73 J.B.A. England, Australian National University internal report ANU-P/534., Nucl. Instr. and Meth., 106 (1973) 45.

Er70 F. Erdas, B. Mosconi, A. Pompie and P. Quarati, Phys. Lett., 32B (1970) 659.

Er71 F. Erdas, A. Pompie, P. Quarati and B. Mosconi, Nucl. Phys., A174 (1971) 657.

Ev59 H.C. Evans and E.H. Bellamy, Proc. Phys. Soc. 74 (1959) 483.

Fa63 H. Faissner, F. Ferrero, A. Ghani and M. Reinharz, Nucl. Instr. and Meth. 20 (1963) 289.

Fe56 H. Feshbach and E.L. Lomon, Phys. Rev., 102 (1956) 891.

Fe61 H. Feshbach, E.L. Lomon and A. Tubis, Phys. Rev. Lett., 6 (1961) 635.

Fi73 S. Fiarman and W.E. Meyerhof, Nucl. Phys. A206 (1973) 1.

Fo76 J.L. Fowler and W.W. Havens Jr., Phys. Today, Aug., (1976) 42.

Fo77 J.L. Fowler, J.A. Cookson, M. Hussain, C.A. Uttley and R.B. Schwartz, Annual Progress Report, ORNL-5306, p. 124.

Ga55 S. Gartenhaus, Phys. Rev., 100 (1955) 900.

Ga57 J.L. Gammel, R.S. Christian and R.M. Thaler, Phys. Rev., 105 (1957) 311.

Ga57a J.L. Gammel and R.M. Thaler, Phys. Rev., 107 (1957) 291.

Go60 M.L. Goldberger, M.T. Grisaru, S.W. MacDowell and D.Y. Wong, Phys. Rev., 120 (1960) 2250.

Gu67 B. Gustafsson and O. Aspelund, Nucl. Instr. and Meth. 48 (1976) 77.

Ha62 T. Hamada and I.D. Johnston, Nucl. Phys., 34 (1962) 382.

Ha65 J.M. Hammersely and D.C. Handscomb, "Monte Carlo Methods", Methuen and Co Ltd, 1965.

He69 L. Heller and M.S. Sher, Phys. Rev., 182 (1969) 1Ø31.

Ho71 J.C. Hopkins and G. Breit, Nucl. Data Tables, A9 (1971) 137.

Hu61 M.H. Hull Jr., K.E. Lassila, H.M. Ruppel, F.A. McDonald and G. Breit, Phys. Rev., 122 (1961) 1606.

Hu61a M.H. Hull Jr., K.E. Lassila, H.M. Ruppel, F.A. McDonald and G. Breit, Phys. Rev., 128 (1962) 83Ø

Hu62 M.H. Hull Jr., F.A. McDonald, H.M. Ruppel and G. Breit, Phys. Rev. Lett., 8 (1962) 68.

Ka67 Yu. M. Kazarinov, F. Lehar and Z. Janout, Rev. Mod. Phys., 39 (1967) 571.

Ku61 A.K. Kuckes and R. Wilson, Phys. Rev., 121 (1961) 1226.

Ku66 P. Kuijper, C.J. Tiesinga and C.C. Jonker, Nucl. Instr. and Meth. 42 (1966) 56.

La62 K.E. Lassila, M.H. Hull Jr., H.M. Ruppel, F.A. McDonald and G. Breit, Phys. Rev., 126 (1962) 881

La69 A. Lande and J.P. Svenne, Nucl. Phys., A124 (1969) 241.

Le49 D.H Lehmer, "Mathematical Methods in Large Scale Computing Units", Proc, 2nd Symp. on Large Scale

Digital Calculating Machinery, pp 141-146(1949) Ann. Comp. Lab. Harvard Univ., 26 (1951).

Li68 P. Limon, L. Pondrom, S. Olsen, P. Kloeppel, R. Handler and S.C. Wright, Phys. Rev., 169 (1968) 1026.

Li70 J.T. Lindow, P. Boschung and E.F. Shrader, Nucl. Instr. and Meth. 85 (1970) 151.

Li72 W.W. Lindstrom and B.D. Anderson, Nucl. Instr. and Meth. 98 (1972) 413.

Lo67 E. Lomon and H. Feshbach, Rev. Mod. Phys., 39 (1967) 611.

Ma60 M.H. MacGregor, M.J. Moravscik and H.P. Stapp, Ann. Rev. Nucl. Sci., 10 (1960) 291.

Ma64 M.H. MacGregor, R.A. Arndt and A.A. Dubow, Phys. Rev., 135 (1964) B628.

Ma65 M.H. MacGregor and R.A. Arndt, Phys. Rev., 139 (1965) B362.

Ma66 J.J. Malanify, P.J. Bendt, T.R. Roberts and J.E. Simmons, Phys. Rev. Lett., 17 (1966) 481.

Ma68 M.H. MacGregor, R.A. Arndt and R.M. Wright, Phys. Rev., 169 (1968) 1128.

Ma68a M.H. MacGregor, R.A. Arndt and R.M. Wright, Phys. Rev., 169 (1968) 1149.

Ma68b M.H. MacGregor, R.A. Arndt and R.M. Wright, Phys. Rev., 173 (1968) 1272.

Ma69 M.H. MacGregor, R.A. Arndt and R.M. Wright, Phys. Rev., 182 (1969) 1714.

Ma72 T.G. Masterson, Phys. Rev. C, 6 (1972) 690.

Mc68 I.E. McCarthy, "Introduction to Nuclear Theory",

John Wiley and Sons Inc., (1968).

Me69 W.E. Meyerhof, W. Feldman, S. Gilbert and W. O'Connell, Nucl. Phys., A131 (1969) 489.

Mo68 T.R. Mongan, Phys. Rev., 175 (1968) 1260.

Mu71 G.S. Mutchler, W.B. Broste and J.E. Simmons, Phys. Rev., C3 (1971) 67.

Ni63 B.P. Nigam, Rev. Mod. Phys., 35 (1963) 117.

No63 H.P. Noyes, Phys. Rev., 130 (1963) 2025.

No64 H.P. Noyes, Phys. Rev. Lett., 12 (1964) 171.

No65 H.P. Noyes, D.S. Bailey, R.A. Arndt and M.H. MacGregor, Phys. Rev., 139 (1965) B380.

No67 H.P. Noyes and H.M. Lipinski, Phys. Rev., 162 (1967) 884.

No67a H.P. Noyes, P. Signell, N.R. Yoder and R.M. Wright, Phys. Rev., 159 (1967) 789.

Ok58 S. Okubo and R.E. Marshak, Ann. Phys., 4 (1958)166.

Op58 T.R. Ophel, Nucl. Instr. 3 (1958) 45.

Op78 T.R. Ophel, subroutine COMPTN, private communication.

Pe67 J.K. Perring, Rev. Mod. Phys., 39 (1967) 550.

Ph59 R.J.N. Phillips, Rep. Progr. Phys., 12 (1959) 562.

Pi72 S.C. Pieper and K.L. Kowalski, Phys. Rev., C5 (1972) 306.

Pr62 J.R. Prescott, Nucl. Instr. and Meth. 22 (1963)256.

Pu57 L.D. Puzikov, R.M. Ryndin and J. Smorodinsky, Nucl. Phys., 3 (1957) 436.

Ra74 D.E. Raeside, Amer. Jour. Phys. 42 (1974) 20.

Re68 R.V. Reid Jr., Ann. Phys., 50 (1968) 411.

Ro61 L. Rosen and L. Stewart, Phys. Rev. 126 (1962)1150.

Ro70 L.N. Rothenberg, Phys. Rev., C1 (1970) 1226.

Sa70 P.J. Saunders and G.G. Shute, Honours Thiesis, University of Melbourne, 1970, unpublished.

Sc47 J. Schwinger, Phys. Rev., 72 (1947) 742.

Sc69 A. Schaarschmidt and H.J. Keller, Nucl. Instr. and Meth. 72 (1969) 82.

Se66 R.E. Seamon, K.A. Friedman and G. Breit, Phys. Rev., 145 (1966) 779.

Se68 R.E. Seamon, K.A. Friedman, R.D. Haracz, J.M. Holt and A. Prakash, Phys. Rev., 165 (1968) 1579.

Sh67 Yu. A. Shreider, "The Monte Carlo Method", Pergamon Press, 1967.

Sh70 M.S. Sher, P. Signell and L. Heller, Ann. Phys., 58 (1970) 1.

Si57 P. Signell and R.E. Marshak, Phys. Rev., 106 (1957) 832.

Si58 P. Signell and R.E. Marshak, Phys. Rev., 109 (1958) 1229.

Si67 J.E. Simmons, Rev. Mod. Phys., 39 (1967) 542.

Si69 P. Signell, Adv. Nucl. Phys., 2 (1969) 223.

Sm68 D.L. Smith, R.G. Polk and T.G. Miller, Nucl. Instr. and Meth. 64 (1968) 157.

So63 M.I. Sobel and A.H. Cromer, Phys. Rev., 132 (1963) 2698.

Sp69 Jerome Spanier and Ely M. Gelbard, "Monte Carlo Principles and Neutron Transport Problems", Addison-Wesley, 1969.

St57 H.P. Stapp, T.J. Ypsilantis and N. Metropolis,

Phys. Rev., 105 (1957) 302.

St58 R.H. Stokes, J.A. Northrop and K. Boyer, Rev. Sci. Instr., 29 (1958) 61.

St66 M.F. Steuer and C.A. Kelsey, NUcl. Phys. 83 (1966) 401.

St74a D. Steiner, Nucl. Fusion 14 (1974) 33.

St74b D. Steiner and M. Tobias, Nucl. Fusion 14 (1974) 153.

Ta64 F. Tabakin, Ann. Phys., 30 (1964) 51.

Ta66 Y.C. Yang, Phys. Lett., 20 (1966) 299.

Th69 S.T. Thornton, Nucl. Phys., A136 (1969) 25.

Th70 D.R. Thompson, Nucl. Phys., A143 (1970) 304.

Th70a D.R. Thompson, Nucl. Phys., A154 (1970) 442.

To65 T.A. Tombrello, Phys. Rev., 138 (1965) 40, and 143 (1966) 772.

U170 I. Ulehla, J. Bystricky, E. Humhal, F. Lehar, V. Lelek and J. Wiesner, "Theory of Nuclear Structure": Triests Lectures, 1969 (IAEA, 1970) page 837.

Va63 W.T.H. Van Oers and K.W. Brockman Jr., Nucl. Phys., 48 (1963) 625.

We68 C. Werntz and W.E. Meyerhof, Nucl. Phys., A121 (1968) 38.

Wi63 R. Wolson, "The Nucleon-Nucleon Interaction", (Interscience Publishers, 1963).

Wo56 L. Wolfenstein, Ann. Rev. Nucl. Sci., 6 (1956) 43.

Wo59 D.Y. Wong, Phys. Rev. Lett., 2 (1959) 406.

Wr67 R.M. Wright, M.H. MacGregor and R.A. Arndt, Phys. Rev., 159 (1967) 1422.

Yu35 H. Yukawa. Proc. Math. Soc. Japan, 17 (1935) 48.